1993

The Response Of An Hyperpure Germanium Detector To Ionizing Radiation

Shao Ying Tong

THE RESPONSE OF AN HYPERPURE Ge DETECTOR TO IONIZING RADIATION

by

Shao Ying Tong

Department of Physics

Submitted in partial fulfilment
of the requirements for the degree of
Doctor of Philosophy

Faculty of Graduate Studies
The University of Western Ontario
London, Ontario
July 1993

ISBN 0-315-83968-6

ABSTRACT

A basic understanding of the response of semiconductor detectors to ionizing radiation is important for their proper usage and their further development. Such devices may also be used to explore the energy deposition process in semiconductors.

The detailed response of an HPGe detector (~1 cm^3 hyperpure Ge with an ion-implanted front contact) to ionizing radiation has been studied with regard to the radiation ionization energy ratio, $\varepsilon_{ion}/\varepsilon_0$, using radioactive α and γ sources and accelerated ion beams (^1H, $^{3,4}He$, ^7Li). The data span the energy range of a few hundred keV to a few MeV. Effects of temperature and bias voltage variation have been investigated. The response to charged particles and γ-rays have been measured simultaneously by using ^{152}Eu, ^{60}Co, and ^{137}Cs γ-ray sources.

Analysis of the results reveals:

(1) Contrary to earlier conclusions, a difference of ~1% between ε_0 and $\varepsilon_{\alpha \text{ or } p}$ has been found in Ge, often showing $\varepsilon_{\alpha,p} < \varepsilon_0$ - results that are qualitatively in accord with the observed behaviour for Si semiconductor detectors; these observations cannot be explained by trapping or recombination effects during the stopping of the ion in the sensitive volume.

(2) The functional behaviour of $\varepsilon_\alpha/\varepsilon_0$ and $\varepsilon_p/\varepsilon_0$ exhibits a non-linear response of the Ge detector as a function of ion energy for a given projectile, which is similar to results observed for Si detectors; the ratios approach unity as the particle energy increases - a result that is to be expected from fundamental considerations.

(3) Where comparisons can be made with earlier works, the present results for $\varepsilon_{ion}/\varepsilon_0$

are in good quantitative agreement when similar assumptions are included, *e.g.* the apparent window thickness of the Ge detector is assumed to be independent of ion energy.

(4) The energy loss in the window of the Ge detector is found to vary with the energy of the incident particle in a manner that does not agree with the stopping power curve. The apparent thickness of this window region is observed to decrease dramatically with increasing detector temperature (~30% decrease as T increases from 80K to 175K). This observation suggests that the surface layer of the Ge detector does not consist of a simple passive dead layer. The reasons for this behaviour are not presently understood.

(5) Pronounced channeling effects are evident in the pulse height spectra as the incidence angle of the ions is rotated with respect to the detector surface normal. These features arise from ion channeling effects in the ion−implanted entrance window region. Monte Carlo calculations of the projectile energy loss under channeling conditions are in qualitative agreement with experimental observations. However, such channeling effects do not account for the deviations of $\varepsilon_{ion}/\varepsilon_0$ from unity.

ACKNOWLEDGEMENTS

I would like to sincerely thank my supervisor, Dr. William N. Lennard, for his excellent guidance and enthusiastic support and encouragement throughout the course of my graduate studies.

Many thanks are extended to: Prof. Ian V. Mitchell, who introduced me to Interface Science Western and helped me all the time with his extensive knowledge and experience in both physics and real life, as with his own students; Dr. Keith Griffiths, who was always ready to help me in solving vacuum problems; Prof. Peter Norton, for his encouragement and care; and Drs. Chun−Si Zhang and Y. Y. Xia, who were good friends and always making useful suggestions for my work.

Special thanks are extended to: Dr. R. H. Pehl (Lawrence Livermore National Laboratory) for his kind support for my project; Dr. Andrzej Dygo for his help and guidance in the Monte Carlo calculations; Dr. Leighton Coatsworth for providing some elegant diagrams for my thesis; Dr. Guiti Massoumi for her help and encouragement; Dr. J. Davies for his helpful discussion; and Profs. J. B. A. Mitchell, R. P. Lowe and G. S. Rose for their helpful advice from within the Department of Physics.

I am indebted to Jack Hendriks, Dan O'Dacre, Steve Brawn, Lawrence Green, B. Campbell and I. Schmidt for their strong technical support; without them, the accelerator and ancillary equipment would never have performed so well. Particular thanks are extended to: Harry Chen for his invaluable electronic expertise; Dr. Bernie Flinn for his help with computer problems; John Glasko for his contribution

to sample preparation; Yida Mai for assisting me in experiments; and my fellow graduate students, Hang Tao Tang, Laura Flinn, and many others.

Finally, I would like to thank the Department of Physics, the Faculty of Graduate Studies, the Ontario Ministry of Colleges and Universities and NSERC (Canada) for their financial support.

TABLE OF CONTENTS

LIST OF FIGURES

LIST OF TABLES

mechanisms of radiation interaction with semiconductors are still not satisfactorily explained. In addition, a precise knowledge of the functional behaviour of ε_{ion} for Ge semiconductors is obviously essential if they are to be used for precise charged particle spectrometry. Furthermore, studies of ε_{ion} can in principle yield a better understanding of radiation effects in semiconductor devices. This is the motive for this thesis. Since the absolute value of ε_o in Ge has been measured accurately, only a precise relative comparison of ε_{ion} and ε_o is required. The absolute value of ε_{ion} can be derived easily from the well known ε_o value if the ratio $\varepsilon_{ion}/\varepsilon_o$ is measured. In the following chapters, a detailed study of the response of an HPGe detector will be reported for $\gamma-$rays, p, α and Li particles in term of relative $\varepsilon-$values and their dependence on energy and temperature.

to convert the information carried by the radiation into a measurable quantity is called a radiation detector. A complete understanding of such interactions between radiation and detector materials is necessary for improving detector fabrication to enhance the attendant applications.

1.2 Development of ionization detectors and study of the ionization energy

Since the Geiger-Müller radiation counter was introduced in 1928 [1], there has been a continual development in radiation detection techniques in order to fulfil the requirements for both pure and applied science. According to their functions, radiation detectors can be conveniently divided into three broad groups: dosimeters, track visualization recorders and counters. Among these, dosimeters measure the integrated effect of many ionizing radiations, track visualization recorders record the individual trajectories of some radiation types, and counters detect and record individual events caused by ionizing radiation. Counters operating in pulse mode can measure the energy of radiation recorded and are therefore the most extensively used in nuclear physics, materials science, *etc.* The basic types of counters are scintillators, gas ionization chambers, liquid and solid state detectors. With the exception of scintillators, all detectors are directly based on ionization effects produced when ionizing radiation passes through the working detector medium, *e.g.* ion pairs collected in gas or liquid detectors and electron–hole pairs in semiconductor (solid state) detectors. For radiation energy measurements, the response of ionization detectors to radiation is most concerned with a determination of the so–called "ionization energy", denoted ε, which is the mean energy required to create one ion

pair or electron−hole pair by ionizing radiation. Research is mainly conducted in three directions: the dependence of ε on the radiation type (γ, e^-, α,$\cdots$), as well as the energy and temperature.

Ionization chamber Gas ionization chambers, the oldest and most widely used types of radiation detectors, in which gases comprise the working medium. As mentioned, the working principle of the ionization chamber is simply based on collecting the ion pairs (ionized atom/molecule plus free electron) created by the radiation or the secondary products of the radiation within the sensitive gas volume. Since the density of gases is low, gas chambers have to be made large in order to fully absorb high energy radiation. Due to their size limitation, gas chambers are more suitable to measure low energy electrons, charged particles or radiation exposure (*e.g.* γ−ray counting). The ionization energy is a crucial factor depending on the nature of the radiation and the working gas. A typical value of ionization energy is 30−35 eV/ion pair − a value larger than the binding energy of the least tightly bound electrons, *i.e.* a few eV. This ε−value sets a lower limit on the energy resolution arising from statistical fluctuations during a series of ionization events in the gas chambers. Extensive experimental and theoretical studies on ionization energy for gases are reviewed in a recent ICRU report [2,3]. Studies mainly focused on values for ionization energy in pure gases, noble gases and gas mixtures under different pressures for radiation with different energies. The results have been applied in studies of radiation dosimetry, charged particle spectroscopy, and in studies of the radiation chemistry of gases. Especially the discovery of the Jesse effect (*i.e.* the observed increase in total ionization due to small concentrations of impurities)

provided important knowledge of energy pathways in the noble gases, which was later applied to a variety of practical situations such as trace analyses of atmospheric pollutants and the development of gas lasers. For basic understanding and application, however, the studies are expected to be enhanced in terms of using more charged particle radiation over a wide range of kinetic energy, improving the precision of measurements and trying new experiments on the phenomena predicted by the theory. Also the study of ionization energy with alkali vapours may be pertinent to new energy–generation technologies.

Scintillation detector The scintillation technique is one of the oldest radiation detection techniques and still remains one of the most useful methods available for detection and spectroscopy of a wide assortment of radiation. Instead of collecting ion pairs as in gas ionization chambers, scintillation detectors rely on the detection and amplification of scintillation light quanta (*i.e.* visible photons) produced by ionizing radiation in scintillating materials. This scintillation process is directly associated with the scintillation material and ionization in the material due to the interaction with ionizing radiation. Basically a scintillation detector contains a scintillator and a photosensor; the scintillator can be a gas, liquid, organic or solid luminescent material. The scintillator should ideally convert radiation energy to detectable fluorescence linearly with an high efficiency; the scintillator should be transparent to its own induced light and easily manufactured in large volumes. In modern scintillation detectors, photomultiplier tubes are used as the photosensors. Many types of scintillation detectors, such as alkali halides (*e.g.* NaI), BGO and organic scintillators are described in the references [4,5]. The advantage of solid

scintillation detectors is that they can be made much smaller than the equivalent gas−filled detectors, due to the high density ratio (~1000) of solid scintillation materials to gases. However, in scintillator detectors, the energy required to generate one photoelectron is $\gtrsim$ 100 eV or more, which sets a major limitation to energy resolution. This shortcoming cannot be overcome until better scintillators with higher efficiency in the chain process of converting incident radiation energy to optical signals are developed.

Semiconductor detector The efficient solid ionization detectors, Si and Ge semiconductor detectors, are most commonly used in nuclear physics and ion beam materials science. The development of these semiconductor detectors has brought revolutionary changes in both pure and applied sciences. The reasons for their superiority as a detector material derive from their special properties: (i) they can be made in the form of highly uniform large single crystals; (ii) high resistivity by virtue of their small carrier densities at certain temperatures; and (iii) long carrier drifting length, small bandgap and a low density of traps and other recombination centres. Compared to gas ionization chambers, semiconductor detectors have a number of advantages. Their greater density makes it feasible to achieve complete absorption of high energy particles (e^-, p, α,$\cdots$), X−rays and γ−rays. The detectors can be made more compact to be easily fit in high or ultrahigh vacuum (UHV) systems. A relatively small value of the ionization energy (~3 eV) means better energy resolution via smaller statistical fluctuations in the number of electron-hole pairs produced by the ionizing radiation; the latter feature has improved the accuracy of spectroscopic energy measurements. The development of semiconductor

detectors has progressed since about the 1950's. In 1949, McKay [6] first demonstrated the principle of recording α particles with a Ge point contact rectifier. Soon after, improved Ge p−n junction diode detectors were developed, allowing for the extraction of basic physical data from the measurement. In the beginning, detectors were basically of the p−n junction type. From 1960 to the mid−1970's, however, semiconductor detectors developed dramatically. As a result of progress in understanding more about semiconductors and their interaction with radiation, material processing techniques, electronic pulse processing and ion beam implantation, the new types of surface barrier (Schottky) and implantation types, Li−drifted and high purity semiconductor detectors were achieved gradually with reliable performance. In this period, studies on semiconductors concerning their performance and response to ionizing radiation were very active. Since the 1970's, as the detector planar technique and integrated electronic circuits became feasible, the technology of semiconductor detectors has become more mature. The important innovation and development stages in the history of semiconductor detectors are listed in Table 1.1 (see [7] for relevant references).

McKay already realized the importance of the ionization energy when he tried to understand the behaviour of α particles in his prototype Ge detector (a p−n junction diode). The ε−value he obtained for ~5 MeV α particles in Ge was about 3 eV − a result quite close to the presently accepted value. In that early stage, the ε−value in semiconductors yielded reasonable estimates about electron−hole pair production created by ionizing radiation, the effects of trapping and recombination in the semiconductor detector, and the intrinsic energy resolution the detector could

Table 1.1 Summary of the development of semiconductor detectors*

Time table	Semiconductors	Detector Types
1949 – 1960	Ge	Point contact and p–n junction diodes 1949 Ge point contact diode 1950/1 Ge p–n junction diode 1959 Au/Si surface barrier diode
1960 – 1970	Ge Si	Surface barrier (Schottky), implantation and Li drift detectors 1962 1D–position sensing Au/Si diode with resistive back layer Si(Li) drifted diode Ge(Li) drifted diode 1964/6 Ion implantation studies in Si 1965 Si, Ge X–ray diodes and FET preamplifier 1967 Ion implantation Si diode, 1D and 2D position sensing Si diodes
1970 – 1980	Ge Si	Surface barrier (Schottky) and implantation detectors plus planar technique 1970 Hyperpure Ge detector 1972 Ion implanted Ge diode 1973 Ion implanted ΔE/E Si detector telescope
1980 – present	Ge Si	Surface barrier (Schottky) and implantation detectors plus planar technique 1980 Planar technology for Si detectors 1987 Various Si devices: drift chambers, variable telescopes, low capacitance and current diodes, strip detectors, integrated electronics

* Entries derived from ref. [4]

provide. In the 1960's and early 1970's [4, 8], studies actively focused on: (i) absolute measurements of the ionization energy in Si and Ge for γ, e^- and α particles emitted from radioactive sources; (ii) theoretical studies of the correlation between the ionization energy and the bandgap of semiconductors; (iii) trapping and recombination effects; (iv) pulse height defect for heavy ions or fission fragments; and (v) the Fano factor and ultimate energy resolution for such detectors. The experimental study of the ionization energy tested the hypothesis that it is

independent of radiation energy, type of radiation and the bandgap of the detector materials. Although some contradictory experimental results and a theoretical prediction had been reported, in the end it was believed that: ε had the same value for incident γ and e^- independent of their energies; there was a difference in ε−values of ~1% for γ and α's in Si at 300K; there was no difference in the ε−value for γ and α's in Ge; and there was a small dependence of ε on temperature in both Si and Ge. It must be mentioned that the early experiments were hampered by limitations in the available electronics technology. Later Martini's [9] relative measurements showed that for energetic ions (p, d, α) with energies in the range 10−19 MeV, there was little difference between ε_0 and ε_{ion} found in both Si and high purity Ge detectors.

In 1985, scientists began to study the detailed response of Si surface barrier detectors to light ions over the energy range of a few hundred keV to several MeV with precise corrections for the energy losses arising from the detector entrance "window" and nuclear collisions in the active volume: both these effects contribute to the pulse height defect. A nonlinear energy response of Si detectors to charged particle radiation was found experimentally [10−12]. This effect was described empirically through a dependence of ε_{ion} on the Si stopping power, wherein $\varepsilon_{ion} \rightarrow \varepsilon_o$ (*i.e.* the value of ε for γ's) at both low and high energy. These new data also reported the Z_1-dependence of the response of Si detectors to ions for the range $1 \leq Z_1 \leq 8$. Recently, the nonlinear response of Si surface barrier detectors to 5 − 70 MeV heavy ions (Li, B, C, O, Al and Cl) was studied based on extensive measurements [13]. The ionization energy deduced for those heavy ions was found

to be up to 2.5% smaller than that for ^{241}Am α particles. The nonlinearity of the response of the Si detectors to heavy ions was also smaller than that anticipated from an extrapolation of the early study [11]. The reported results for ε are summarized in Table 1.2.

Comparing the results listed in Table 1.2, it is difficult to reconcile the results of ε_0 and ε_α for Si and Ge semiconductors, notwithstanding the lack of information concerning effects arising from non−ionizing energy losses. As yet, the detailed

Table 1.2 Summary of the studies on ionization energy in Si, Ge detectors

ε ionization	Si detector	Ge detector
ε_0 (for γ−ray) ε_e (for e^-) [14]	Same ε_0 = 3.67 ± 0.02 eV/e−h pair at 300K Independent of their energies Temperature dependence	Same ε_0 = 2.96 ± 0.02 eV/e−h pair at 90K Independent of their energies Temperature dependence
ε_0, ε_α for a few MeV α particles [14]	changes by ~1 % over a wide range of temperature	No difference being found over a wide range of temperature
ε_{ion} for accelerated ions ($1 \le Z_1 \le 8$) with energy less than a few MeV [10-12]	Difference ≥ 1 % compared with ε_p Nonlinear response to radiation E (due to weak E dependence of ε_{ion})	Unknown
$\varepsilon_{p,d,\alpha}$ for 19 MeV ≥ E ≥10 MeV [9]	$\varepsilon_\alpha/\varepsilon_p$ = 0.994 ± 0.0015 at 300K	$\varepsilon_\alpha/\varepsilon_p$ = 0.9989 ± 0.0015 at 90K $\varepsilon_\alpha/\varepsilon_d$ = 0.9963 ± 0.0035 at 90K
ε_{ion} for 5−70 MeV heavy ion (Li, B, C, O, Al and Cl) [13]	ε_{ion} is up to 2.5 % smaller than ε_α (5.486 MeV)	Unknown

mechanisms of radiation interaction with semiconductors are still not satisfactorily explained. In addition, a precise knowledge of the functional behaviour of ε_{ion} for Ge semiconductors is obviously essential if they are to be used for precise charged particle spectrometry. Furthermore, studies of ε_{ion} can in principle yield a better understanding of radiation effects in semiconductor devices. This is the motive for this thesis. Since the absolute value of ε_o in Ge has been measured accurately, only a precise relative comparison of ε_{ion} and ε_o is required. The absolute value of ε_{ion} can be derived easily from the well known ε_o value if the ratio $\varepsilon_{ion}/\varepsilon_o$ is measured. In the following chapters, a detailed study of the response of an HPGe detector will be reported for $\gamma-$rays, p, α and Li particles in term of relative $\varepsilon-$values and their dependence on energy and temperature.

References

1. W. J. Price, "Geiger–Müller and Proportional Counters," in Radiation Dosimetry, Vol. II (F. H. Attix and W. C. Roesch, eds.), Academic Press, New York, 1966.
2. "Average Energy Required to Produce an Ion Pair", ICRU Report 31 (1979).
3. R. Bouclier, J. J. Florent, J. Gaudaen, F. Sauli and L. Shekhman, Nucl. Instr. and Meth. A315 (1992) 521.
4. J. B. Birks, "The Theory and Practice of Scintillation Counting", Pergamon Press, Oxford, 1964.
5. G. F. Knoll, "Radiation Detection and Measurement", Wiley, 1989 (2nd edition).
6. K. G. McKay, Phys. Rev. 76 (1949) 1537.
7. S. Kalbitzer, "Semiconductor Detectors for Nuclear Radiation – a Review," Max–Planck–Institute für Kernphysik, Heidelberg, MPIH–V16–1991, (Symposium on Materials Research with Ion Beams).
8. G. Bertolini and A. Coche, "Semiconductor Detectors," North–Holland Publishing Company, Amsterdam, 1968.
9. M. Martini, T. W. Raudorf, W. R. Stott, J. C. Waddington, IEEE Trans. on Nucl. Sci. NS–22 (1973) 145.
10. W. N. Lennard, H. Geissel, K. B. Winterbon, D. Phillips, T. K. Alexander and J. S. Forster, Nucl. Instr. and Meth. A248 (1986) 454.
11. W. N. Lennard and K. B. Winterbon, Nucl. Instr. and Meth. B24/25 (1987) 1035.
12. P. Bauer and G. Bortels, Nucl. Instr. and Meth. A299 (1990) 205.
13. D. Comedi and J. Davies, Nucl. Instr. and Meth. B67 (1992) 93.
14. R. H. Pehl, F. S. Goulding, D. A. Landis and M. Lenzlinger, Nucl. Instr. and Meth. 59 (1968) 45.

Chapter 2

SEMICONDUCTOR DETECTORS AND THEIR INTERACTION WITH RADIATION

2.1 Bandgap and structure of semiconductor detectors

2.1.1 Semiconductors

The term semiconductor customarily refers to a class of materials with resistivity between 10^{-2} and 10^{9} Ω-cm, intermediate between conductors (~10^{-5} Ω-cm) and insulators (~10^{14}-10^{22} Ω-cm). Common examples include: (1) elemental semiconductors of IV group of the periodic table, such as Si and Ge, and (2) compound semiconductors, such as GaAs, InSb, AlP, GaP, CdS, ZnS, CdTe, ZnO, PdS, PdTe. Although GaAs and related III-V compounds are gaining importance for their potential uses associated with injection lasers and ultrafast electronic devices, Si and Ge are the most important semiconductors with wide commercial applications. Si and Ge atoms both have an half-filled outer electron shell ($3s^2$ $3p^2$ for Si and $4s^2$ $4p^2$ for Ge) and form crystals with the diamond fcc structure. Figure 2.1 shows a schematic of the band structure for electron energy levels in semiconductors. At T=0K, the valence band is filled with electrons, which are bound to specific lattice sites (forming covalent bonds) in the crystal and cannot migrate, and no free electrons are in the conduction band. In intrinsic (pure) semiconductors, the number of electrons in the conduction band (n) is equal to the number of holes (p) in the valence band; this equilibrium is due to the balance the thermal excitation of electron-hole pairs and their recombination, *i.e.*

$$p=n=CT^{\frac{3}{2}}\exp\left[-\frac{E_g(T)}{2kT}\right] \tag{2.1}$$

where T = absolute temperature, E_g = bandgap, k = Boltzmann's constant and C is a proportionality constant relating to the effective mass of e^- and h. In spite of a weak temperature dependence of E_g, the concentration of the e-h pairs changes very quickly with the semiconductor temperature. For instance, at T = 300K the

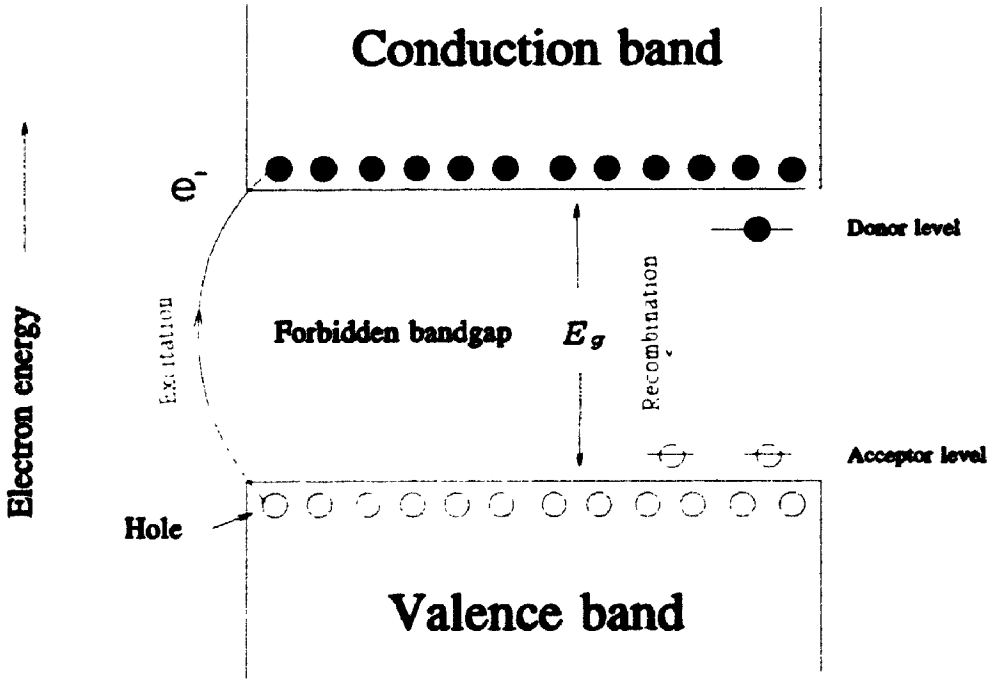

Figure 2.1 Bandgap structure of electron energy levels in semiconductors, where there are no electron states in the bandgap except for states due to impurities. Excitation and recombination processes are marked by the solid and dashed lines.

intrinsic e-h pair densities are 1.5×10^{10} cm^{-3} in silicon and 2.4×10^{13} cm^{-3} in germanium. In the presence of an electric field in the semiconductor, the electrons in the conduction band and the holes in the valence band are free to migrate and both contribute to the electrical conductivity of an intrinsic semiconductor. At the same time, recombination will be gradually reduced with increasing strength of the electric field.

Impurities in a semiconductor - even at trace levels - can substantially change the population of conducting electrons or holes. Because the impurity (donor or acceptor) energy levels are very close to the conduction or valence band (~0.01 eV in Ge and ~0.04 eV in Si), the carriers can be easily excited thermally, thereby contributing to the conductivity. Such a contribution depends on the net donor or acceptor concentration and also weakly on the temperature of the semiconductor.

2.1.2 Planar semiconductor detectors

Planar Si and Ge semiconductor detectors basically can be classified as: (1) Schottky surface barrier type, or (2) implantation type. Both types can be simply described as a "pure" Si or Ge wafer with thin front and back conducting layers, operating at a reverse bias voltage. The term "pure" means that Si and Ge wafers can be either of mildly p-type, mildly n-type (10^{15} donor atoms/cm^3), lithium-compensated or intrinsic (only rarely) semiconductors. The Schottky surface barrier type refers to a semiconductor detector with thin front and back metallized layers. Figure 2.2 shows an example of a thin metal layer deposited on an n-type semiconductor, forming an intimate contact. Due to the higher electron carrier

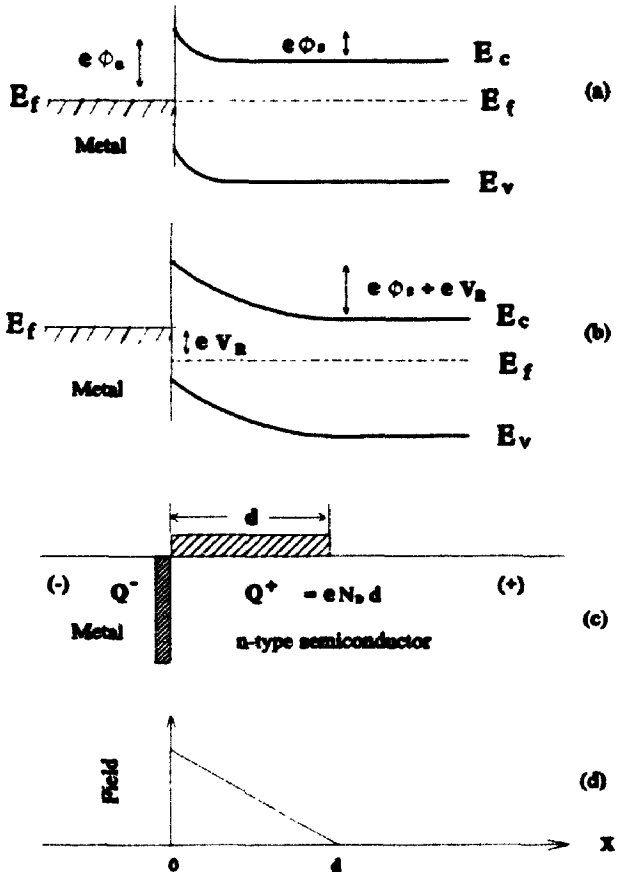

Figure 2.2 (a) Band structure at interface of the metal–semiconductor contact; (b) bent band structure, (c) space charge distributions, and (d) electric field in semiconductor, with a reverse bias applied across the interface.

concentration on the metal side, the energy band of the semiconductor bends up at the metal-semiconductor interface and a space-charge distribution is established in the semiconductor near the interface region. Therefore, a potential barrier, ϕ_B, exists at the interface thereby impeding electrons in the metal from entering the semiconductor; the magnitude of this barrier depends on the metal and the semiconductor. When a reverse bias, V_R, is applied across the metal-semiconductor

junction (low potential on the metal), the Fermi level of the metal and the energy band of the semiconductor at the interface will be raised by an amount eV_R, causing more charge to accumulate on both sides of the interface, see Figure 2.2(b). The negative charges are concentrated within a very thin layer on the metal side of the interface and the positive charge distribution has to be built up by repelling the donor electrons away in the n-type semiconductor. Since the donor concentration is uniform and relatively small, the charge distribution in the semiconductor must be uniform and extends further into the semiconductor from the interface, see Figure 2.2(c). The corresponding electric field shown, in Figure 2.2(d), decreases linearly from the interface according to:

$$E = \frac{eN_D}{\epsilon}(d-x) \tag{2.2}$$

where ϵ is the permittivity, N_D is the donor density of the semiconductor, and d is the depth of the charge distribution, called the depletion depth. The depletion depth is a function of the reverse bias applied,

$$d = \left(\frac{2\epsilon V}{eN_D}\right)^{\frac{1}{2}} \tag{2.3}$$

For implantation-type semiconductor detectors, the situation is different. Instead of the metal front and back layers, the thin front and back conducting layers are comprised of heavily doped n- and p-type layers or vice versa formed by implanting donor- and acceptor-type atoms into the surface of "pure" semiconductor wafers. That means that a p-n junction replaces the surface barrier contact at the surface of the semiconductor detector. Figure 2.3 shows the change at a p-n junction

when a reverse bias is applied across the junction. Because the n-type side is heavily doped relative to a mildly p-type side (*i.e.* $N_D \gg N_P$) and the depletion depth is proportional to $(N_D)^{-1/2}$, the depleted region in the n−type region is negligible compared with that in the p−type region under the reverse bias. The total depletion depth is almost determined by Equation 2.3, substituting N_P for N_D. The electric field under a reverse bias on the p-type side is similar to the surface barrier case, see Figure 2.3(d).

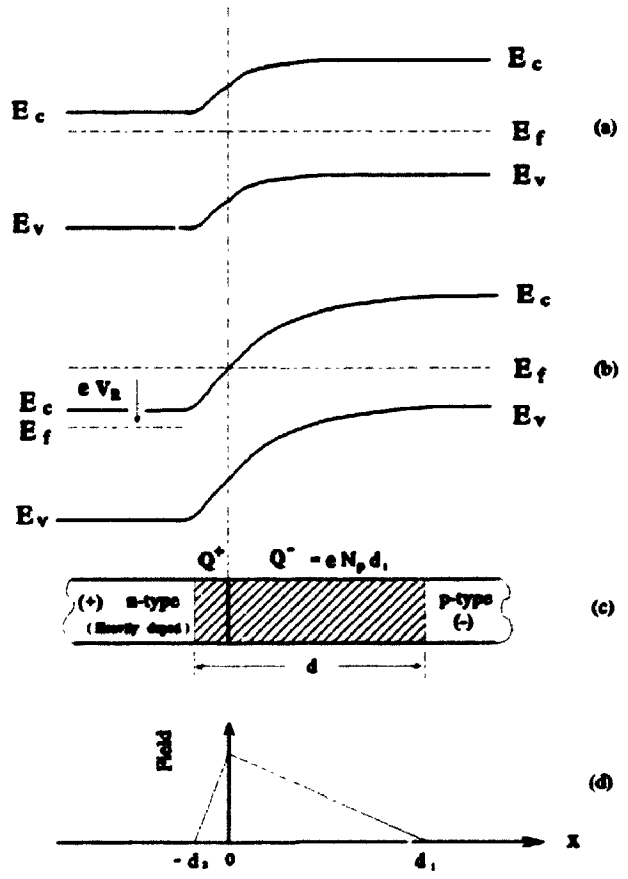

Figure 2.3 Band structure change at interface of heavily doped n−type and mildly p−type semiconductors. (a) without a bias; (b) with a reverse bias. (c) and (d) show charge and electric field distribution with a reverse bias.

Both types of semiconductor detectors are operated under a reverse bias applied between the front and back conducting surfaces, similar to a diode with a reverse voltage. On increasing the bias, the electric field penetrates deeper into the wafer. The reverse bias value for which d is equal to the wafer thickness is called the depletion voltage; at this value, the electric field reaches the back conducting layer. The detector is said to be fully depleted at this point. Further raising the bias voltage results in a constant increase of the electric field everywhere in the wafer. The thickness of wafer that can be fully depleted using bias voltages below that value which causes catastrophic breakdown depends on the purity of the semiconductor. Depletion of over 1 cm thickness can be achieved for ultrapure Ge and generally no more than several millimeters for Si. Figure 2.4 shows several different configurations for fully depleted semiconductor detectors. There are several advantages (*e.g.* larger sensitive volume) for the detectors operating in the fully depleted condition, which will be mentioned in section 3.

The front conducting layer of detectors is conveniently called the entrance "window", which is either a metal evaporated layer (including some oxide or sub-oxide layer at the interface) or an heavily doped semiconductor layer. The "window" layer is usually required to be as thin as possible. In principle, the higher bias will help in reducing the thickness of the front and back layers, but this is not true for implantation detectors [1].

2.2 Interaction of ionizing radiation with semiconductors

Si and Ge planar detectors are commonly used for measuring energies of

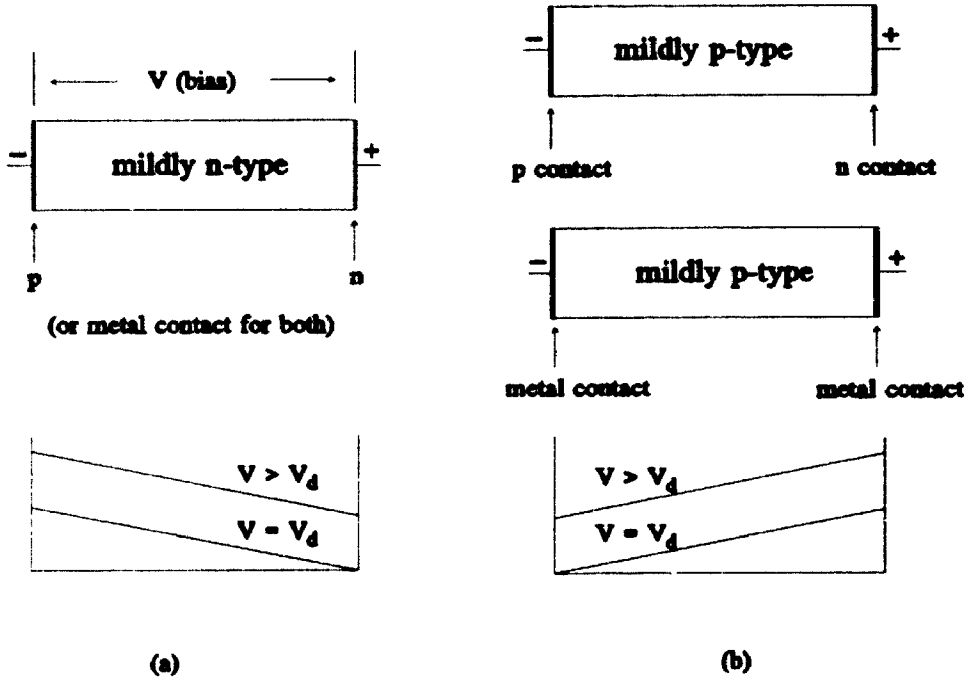

Figure 2.4 Different configuration of a planar semiconductor detector and electric field distribution under a reverse bias. The indicated p, n and metal contacts refer to the thin heavily p−type, n−type semiconductor and metal layers.

incident electrons, heavy charged particles (*i.e.* light ions, heavy ions, or muons), visible light, X-rays and γ rays. Their working principle is based on the ionization effect created by radiation in semiconductor detector materials. Although the final results from the interaction of charged particles and electrons with semiconductors consist of a number of ionization tracks containing electron-hole pairs, each has its own manner of achieving that end. Thus, separate discussions are necessary. In the following, the terminology "stopping power" refers to the energy loss per unit pathlength.

2.2.1 Interaction of electrons with semiconductors

The interaction of electrons with semiconductor materials is important since such an interaction is often involved in secondary processes following primary interactions of other type of radiation (*e.g.* X or γ) with semiconductor materials. There are two major energy loss mechanisms: (1) collisional energy loss, caused by inelastic Coulomb collisions with bound atomic electrons of the semiconductor resulting in ionization and excitation; (2) radiative energy loss, arising from the emission of *Bremsstrahlung* radiation in the electric field of the atomic nucleus and of the atomic electrons, which increases with increasing electron energy and only produces low-energy photons for typical electron energies. The ratio of radiative to collisional stopping power is approximately equal to $(4/3\pi)\ Z_2\ \alpha_f\ (v/c)^2$, where α_f is the atomic fine structure constant, v is the velocity of electrons, c is the velocity of light, and Z_2 is the atomic number of the medium.

Since most interactions are collisions between the incident and target electrons of equal mass, the path of the incident electron is a tortuous one. Therefore, some electrons can be completely stopped in a semiconductor layer thinner than the range of these electrons. The stopping power and range for electrons can be obtained from theory [2].

2.2.2 Interaction of heavy charged particles with semiconductors

The most important parameter of heavy charged particles (ions) is their atomic number, which determines to a large degree their interaction with semiconductor materials. The outer shell electrons of charged particles may be

stripped off at high velocity or the ion can capture electrons from the atoms of the target medium at lower velocity when they penetrate the detector.

The energy loss for energetic heavy charged particles traversing a medium occurs via collisions with electrons and nuclei in the medium. Collisions with the electrons cause excitation and ionization of the bound (valence or core) electrons. Those ionized electrons (or δ-rays) with enough kinetic energy can subsequently induce secondary ionization and excitation, and eventually dissipate all their kinetic energy in the semiconductor. This type of collision is inelastic and the corresponding energy loss of the ions is called the electronic energy loss. The second kind of collision arises through (screened) Coulomb scattering between the incident charged particle and a target nucleus. A vacancy in the lattice can be created and further ionization or excitation will occur as the recoiling nucleus slows down. The probability for heavier particles to have nuclear collisions with the atoms of the medium increases with the projectile mass at fixed energy. Energy transfer to the nucleus (or atom) will be described in detail in a later chapter. This type of energy loss is called nuclear energy loss. The electronic energy loss dominates for the higher energy region and the nuclear energy loss dominates at lower energy, *i.e.* close to the end of the particle range. The paths of heavy charged particles in the detector medium are virtually straight, except near the end of range. The density of electron-hole pairs due to ionization along the track of the incident particles is higher for heavier particles. For charged particles with an energy less than 10 MeV, the ranges are no more than 1 mm in Si and Ge semiconductors. Conveniently, the dE/dx (total stopping power) is divided into the electronic and nuclear stopping power regimes,

which can be found in reference [3,4]. Figure 2.5 shows an example of the ratio of the nuclear stopping to the total stopping as a function of the energy for ^{4}He ions in Ge.

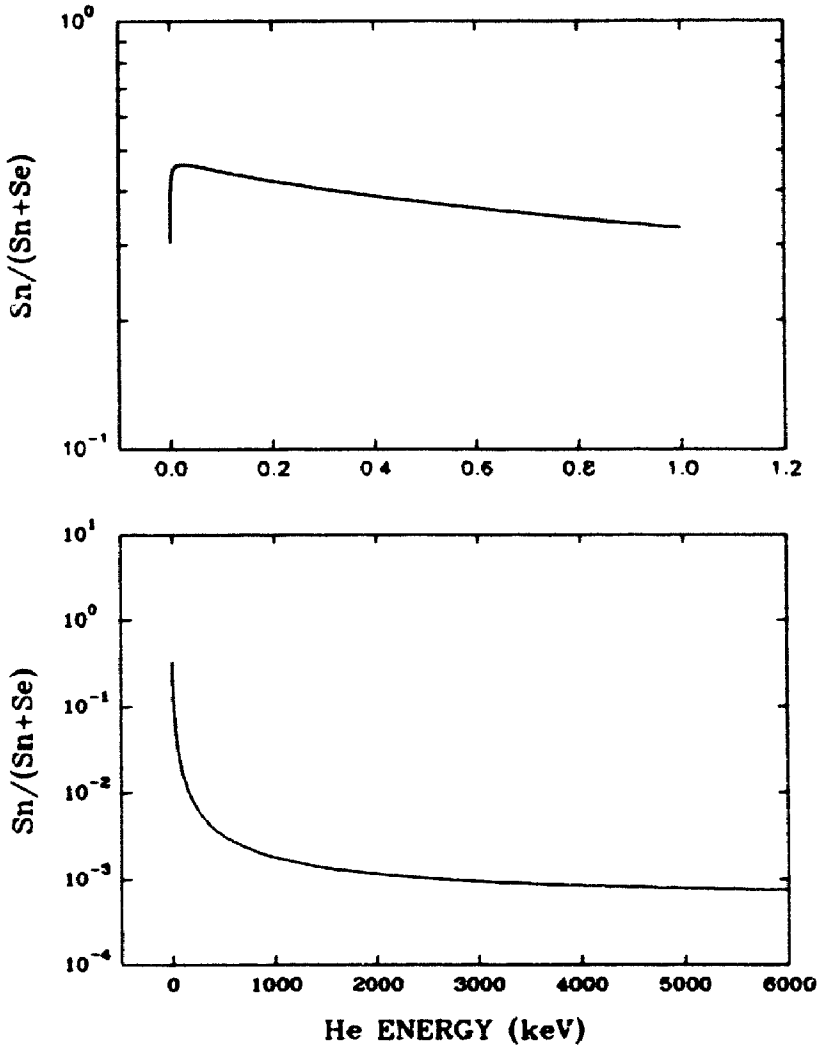

Figure 2.5 The ratio of the nuclear stopping (S_n) to the total (nuclear+electronic) stopping (S_n+S_e) is shown as a function of the energy for ^{4}He ions in Ge. Nuclear stopping has insignificant contribution to the total stopping in the high energy region. The ^{4}He energy scale for the upper panel is also in keV.

2.2.3 Interaction of photons with media

A photon is an uncharged energy quantum, which can interact with solid materials through three major processes: photoelectric absorption, Compton scattering and pair production. Photons either disappear entirely or are scattered through significant angles in the former two processes respectively, where the Compton scattering will lead to a transfer of some of the original photon energy to a recoil electron (of course, photons may penetrate through a thin absorber without losing any of their energy). The probabilities per atom for these three processes depend on the photon energy and on the atomic number of the medium. Photoelectric absorption dominates at low photon energy (up to a few hundred keV), pair production dominates at photon energies exceeding 5-10 MeV, and Compton scattering is the most probable process in the energy range intermediate between these two extremes [5].

(1) Photoelectric absorption

In this process, a photon interacts with an absorber atom in a manner such that it is completely absorbed by the atom; an energetic photoelectron is ejected from one of the atom's bound orbits having an energy $E_e = h\upsilon - E_b$ (E_b is the binding energy of the photoelectron). As a consequence of free electron capture or rearrangement of electrons within the residual ion, characteristic X-rays or Auger electrons can be generated. The X-rays are reabsorbed in the neighbouring atoms through photoelectric absorption involving less tightly bound electrons, unless they escape from the detector. The probability per unit pathlength, τ, for photoelectric absorption can be estimated from the expression

$$\tau \propto const. \times \frac{Z^n}{E_\gamma^{3.5}} \tag{2.4}$$

where the exponent, n, has a value between 4 and 5.

(2) Compton scattering

The incident photon can interact directly with individual electrons in the absorber via a Compton scattering process. In such a process, the photon is deflected from its incident direction, transferring a portion of its energy to tne (recoil) electron. The energy transferred to the recoil electron depends on the energy of the incident photon and the scattering angle. The cross section for Compton scattering is well described through the Klein-Nishina formula [5]. The γ-ray energies of many radioactive sources fall in the energy region where Compton scattering is predominant. The distribution of the energy transferred to the electrons exhibits a continuous spectrum which can be calculated by averaging over all Compton scattering angles with the appropriate cross sections. For instance, the maximum energy of a Compton-scattered electron for the case of a photon of energy $h\upsilon$ scattered to 180° from a free electron is given by

$$E_e = \frac{2m_0c^2h\upsilon}{m_0c^2+2h\upsilon} \tag{2.5}$$

(3) Pair production

This process must occur in the Coulomb field of a nucleus. When the photon energy exceeds 1.02 MeV, *i.e.* twice the rest-mass energy of an electron, it is energetically possible for the photon to disappear and create an electron-positron pair with the sum of their kinetic energies equal to $h\upsilon$-$2m_0c^2$. After travelling a short

distance, the positron will annihilate and produces two annihilation photons, each with an energy m_0c^2 (0.511 MeV).

Overall, the attenuation of the primary photons by the above competing processes follows an exponential law:

$$I = I_0 e^{-\alpha t} \tag{2.6}$$

where I_0 is the incident photon flux, I is the photon flux transmitted through a thickness, t, of the absorber and α is the linear attenuation coefficient. Therefore, for a thin semiconductor layer, there exists a finite probability (1-exp[-αt]) that the full energy of an incident photon can be totally absorbed (*e.g.* photoelectric effect) to generate electron-hole pairs in the layer, albeit with low interaction efficiency.

2.3 Response of Si and Ge detectors to ionizing radiation

The response of Si and Ge detectors to ionizing radiation is very important for understanding the basic interaction of the radiation with matter as well as for applications of semiconductor detectors. In some situations, the results obtained from the detectors could be misinterpreted due to a lack of a complete understanding of the detailed detector response. In principle, the response depends on the properties of the radiation and the parameters of the detector. The common features and difference in the response of the detectors to radiation will be described phenomenologically with respect to the physical mechanisms.

2.3.1 Charge collection and ionization energy

There are always a certain number of electron-hole pairs existing due to

equilibrium between the thermal generation of electron-hole pairs and their recombination. In the absence of an electric field in the detector, these electrons and holes move randomly within the semiconductor. When a reverse bias is applied to the detector, in the depleted region the electrons drift towards the positive electrode and holes drift towards the negative electrode. The migration is the net result of the random thermal motion plus the drifting parallel to the direction of the applied field. The drift velocity is proportional to the applied field for low or moderate electric field strengths:

$$V_e = \mu_e E$$
$$V_h = \mu_h E \qquad (2.7)$$

where E is the electric field magnitude and μ_e, μ_h are the proportionality constants, or mobilities, for electrons and holes, respectively. In semiconductors, μ_e and μ_h are approximately equal, which indicates that the drift velocities along the direction of the electric field for electrons and holes are approximately equal at the same electric field strength. At high electric fields, the drift velocity reaches a saturation value and then becomes independent of the electric field. The electric field required to reach the saturation velocity depends on the detector temperature. Since lattice scattering become more important at higher temperature, the carriers require higher electric field to reach their saturation velocity, *e.g.* μ_h=450 $cm^2\ sec^{-1}\ V^{-1}$ for holes in Si at room temperature requiring an electric field exceeding ~10^5 V/cm.

Most semiconductor detectors are commonly operated using a bias higher than the depletion voltage in order to obtain larger and more uniform electric fields in the active volume of the detector. The electric field normally in the active volume of the

detector ensures a saturated drift velocity for the charge carriers (except for thick Si detectors at room temperature).

Since the saturated velocity in Si and Ge semiconductors are ~10^7 cm/s, the collection time for electron-hole pairs generated from a single radiation interaction event in the active volume of the detector can be very short, depending on the physical dimensions of the detector. For instance, the charge collection time for a typical dimension of 1 mm or less will be less than 10 ns. This estimate suggests that the response of the detector to a single radiation interaction event in its active volume will produce a fast charge pulse output. If there is no loss of the electron-hole pairs, the total amount of charge collected should equal the number of electron-hole pairs created by the single radiation interaction event, *i.e.* proportional to the energy deposited in the depleted volume by the radiation. The proportionality constant is called the "ionization energy", ε ($E=\varepsilon N_{e-h}$), which is the average energy required for creating one electron-hole pair in a semiconductor detector by the radiation. The collection of the thermally generated electron-hole pairs can make a small contribution to the output signal, which is reflected in the leakage current of the detector (measured without radiation).

2.3.2 Spectra for energetic charged particles and photons

Using appropriate electronics, the output charge pulses from the semiconductor detector (analog signal) can be converted via an analog-to-digital converter (ADC) to counts in the channels of a multichannel analyzer (MCA). The channel number is linearly proportional to the amount of charge collected; the

number of counts record the corresponding number of events. Thus, the energy spectrum of the incident radiation can be recorded, provided the detector is large enough to fully absorb the incoming particles.

(1) Electrons

The full energy peak corresponding to the total electron energy used to create e-h pairs in the active volume of the detector will be observed in the spectrum. Those electrons that deposit only part of their energy in the active volume of the detector will produce peaks at lower energy. Backscattering of the incident electron or the escaping of their secondaries from the entrance window (the front conducting surface) can have a significant effect on the response of the detector. Such phenomena are most pronounced for electrons with low incident energies and for target materials with high atomic numbers; for such cases, the backscattering fraction can be as high as 50% [3]. This process will cause partial energy peaks for some of the incident electrons which strike the detector. The spectrum for monoenergetic incident elections shows a nearly flat background extending from zero to the full energy peak. There is only a small energy loss of the incident electrons in the entrance window of the detectors, except for low energy electrons.

(2) Heavy charged particles

For monoenergetic ions, a full energy peak will be recorded by the semiconductor detector if the depletion depth of the detector exceeds the particle range. But the incident ions will lose part of their energy in the entrance window of the detector, since the energy deposited by the incident ion in the window (conducting layer) of the detector will not create any stable electron-hole pairs. In

general, heavy ions will lose more energy than light ions of the same incident energy in the detector window. Since the electronic stopping power for light ions of the same energy is larger in Ge than in Si, Ge detectors can be used for measuring more energetic ions. For example, the maximum thickness for (uncompensated) Si detectors is ~5 mm, which is equivalent to the range of 120 MeV α particles, and ~1.5 cm thickness for Ge detectors, which corresponds to the range of 300 MeV α particles.

(3) Photons

Similar to the case for energetic electrons, large detectors and low photon energy will only increase the detection efficiency for γ-rays. Hence the full energy peak mainly due to the photoelectric process will be seen for all detector sizes, in which the total energy of the incident photon is dissipated in creating electron-hole pairs in the detector active volume. For small detectors, as used in this thesis, the Compton spectrum extends from zero to the maximum energy close to that determined by Equation 2.5, which is lower than the full energy peak.

2.3.3 Resolution and Fano factor

The response function of semiconductor detectors to monoenergetic charged particles or photons exhibits a nearly-Gaussian distribution based on experimental observations. The energy resolution of detectors is defined as

$$R = \frac{FWHM}{H_0} \tag{2.8}$$

where H_0 is the peak centroid and FWHM is the full width at half maximum height

of the peak. There are several sources of fluctuations which contribute to the resolution of a detector, such as statistical fluctuations in the collected charge, electronic noise, electric drift, microphonic noise, *etc.* Since most of these contributions are symmetric and independent, the overall distribution tends toward a Gaussian shape. Adding them in quadrature, the overall FWHM will be expressed:

$$(FWHM)^2_{total} = (FWHM)^2_{statis} + (FWHM)^2_{e.noise} + (FWHM)^2_{micro} + \cdots$$

The total FWHM can be directly determined from the spectrum; the individual contributions can be estimated under certain conditions.

The energy resolution is a key parameter for judging the quality of detectors, which will give a measure of the energy peak spread for detectors exposed to monoenergetic radiation. Two peaks are resolved when their separation is larger than the detector FWHM at the corresponding energy. In the following, some of the important noise contributions are discussed.

(1) Statistical fluctuation in the number of charge carriers

The statistical fluctuation occurs in the process of generating electron-hole pairs in the active volume of the detector by a quantum of ionizing radiation. While the primary incident charged particle or photon, or the ionization shower products (electrons, holes, recoil nucleus or photons) create electron-hole pairs in the detector, other processes of smaller energy losses are always involved, such as vibrational excitation of the crystal lattice, displacement of the lattice atoms, defect creation, *etc.* Such energy loss involved in these processes is not enough to create electron-hole pairs. Thus, the mean ionization energy for creating one electron-hole pair is about three times the bandgap energy in semiconductor detectors. And also for a given

energy deposited by radiation in the detector, the total number of electron-hole pairs created is subject to statistical fluctuations. In the ionization process, the generation of charge carriers does not follow a Poisson model, indicating that all events along the ion track are not independent. The Fano factor, F [4,6,7], has been introduced to describe the variance, σ, in the total number of electron-hole pairs measured for the actual process, *i.e.*

$$\sigma = \left(\frac{FE}{\epsilon}\right)^{\frac{1}{2}}$$
$$R = 2.35\left(\frac{F\epsilon}{E}\right)^{\frac{1}{2}} \qquad (2.9)$$

where F=1 for the Poisson process. The experimental determination of F is difficult, since all other contributions to the total FWHM (resolution) must be precisely known or estimated reliably. For γ rays and electrons, the Fano factor ranges from 0.09 to 0.3 for Si detectors without evident changes observed with the temperature, and 0.08−0.3 for Ge detectors at 77K [7-9]. For charged particles, the energy loss in the detector window causes problems in determining F reliably.

(2) Electronic noise and electronic drifting

The electronic noise here refers to the noise coming from the detector leakage currents and the preamplifier-amplifier-analyzer system including the connecting cable between the detector and preamplifier. For leakage current, one source is the bulk leakage current of detectors, which comes from the fluctuations in the number of thermally generated electron-hole pairs in the active volume of the detector. The bulk leakage current can only be reduced through temperature reduction of the detector crystal (see Equation 2.1). Another source is from the fluctuation in surface

leakage current related to the fabrication of detectors. Damage or contamination at the interface between the surface conducting layer and bulk crystal of detectors can cause severe leakage and breakdown problems.

There is one kind of noise called Johnson noise, which is associated with series resistance or poor electrical contacts to detectors, including the series resistance of the undepleted region of partially depleted detectors.

(3) Energy loss straggling for heavy charged particles

The energy loss of heavy charged particles moving through a thin layer of an homogeneous medium is determined by many individual collisions. The energy loss for particles with the same initial energies that follow the same path is not identical due to statistical fluctuations in the energy loss. Fluctuations in the electronic energy loss give rise to electronic energy loss straggling, which depends on the incident particle and the target (medium). At high velocities where electronic collisions make the dominant contribution to the energy loss, energy loss straggling, Ω, can be approximately described by the Bohr theory [10]:

$$\Omega_B^2 = 4\pi Z_1^2 Z_2 e^4 N t \qquad (2.10)$$

where Z_1 is the atomic number of the projectile, Z_2 is the atomic number of the target, e is the electron charge, N is the number of target atoms per unit volume, and t is the target thickness. The Bohr straggling formula, which is independent of the particle energy, often overestimates the energy loss straggling at lower velocities [10]. Although the energy loss of incident particles in the entrance window will not contribute to the total number of electron-hole pairs generated in the detector, the

energy loss straggling in the entrance window will affect the residual energy distribution of the particle after passing through the window, which certainly will degrade the detector resolution. In fact, some authors [11] have used the measured resolution to try to extract the detector window thickness.

(4) Trapping effects

Trapping centres in semiconductors are associated with impurities and crystal imperfections, which produce energy levels in the energy bandgap. The carriers can be trapped by these energy levels and the average time a carrier remains trapped before being thermally detrapped is called the detrapping time, which depends on both the depth of the trap and the temperature. If the detrapping time is of the same order of, or longer than, the pulse-shaping time used in the amplifier, then a net loss of charge results. The variation of trap concentration at different locations in the detector results in different carrier losses from one event to another, which will add fluctuations to the output signal, particularly at low temperature. Significant trapping effects in detectors will give rise to a low energy tail on the peaks observed for a monoenergetic source of radiation. But for heavier ions, the low energy tail may arise from recombination effects. The bandgap in Ge (0.7 eV) is smaller than in silicon (1.1 eV), leading to smaller trapping effects in Ge compared to Si detectors [9].

As a conclusion on overall noise sources, electronic noise and drifting are usually the limiting factors that determine the resolution for photon peaks in semiconductor detectors; energy loss straggling in the entrance window of the detector will make the dominant contribution to the energy resolution for heavy

charged particles.

2.3.4 Temperature dependence of the output pulses and pulse height defect

The temperature effect on the response of Si and Ge detectors to radiation basically depends on the variation of the ionization energy with the temperature of detectors. It has been shown that the bandgaps of Si and Ge semiconductors decrease with increasing temperature, see Figure 2.6, and the ionization energy for γ-rays, electrons and some light ions is approximately linear with the bandgap for Si and Ge detectors (and generally true for the bandgaps of different semiconductors, see refs. 12 and 13). Therefore, the output pulse height will be subject to changes due to the variation of ε with the temperature of detectors.

The pulse height defect was observed in the 1960's [11], when Si detectors were used to measure the energy of fission fragments. The pulse height defect is commonly defined [11] as the difference between the true energy of the heavy ion and its apparent energy which is determined from an energy calibration of the detector obtained using alpha particles, *e.g.* see Figure 2.7. Many studies have shown [14-17] that the pulse height defect in semiconductor detectors can be ascribed to three effects: (1) the energy loss of heavy ions in the entrance window/dead layer of detectors, which can be calculated using the stopping power if the window thickness is known; (2) the energy loss of heavy ions arising from nuclear collisions, for which the cross section can be large for heavy ions at low energy; (3) charge carrier columnar recombination in the dense electron-hole plasma generated along the track of an heavy ion; the heavier the ion, the more dense is the plasma along the particle

track. Although a pulse height defect occurs in detectors for light ions as well, such a defect is often too small to be easily observed.

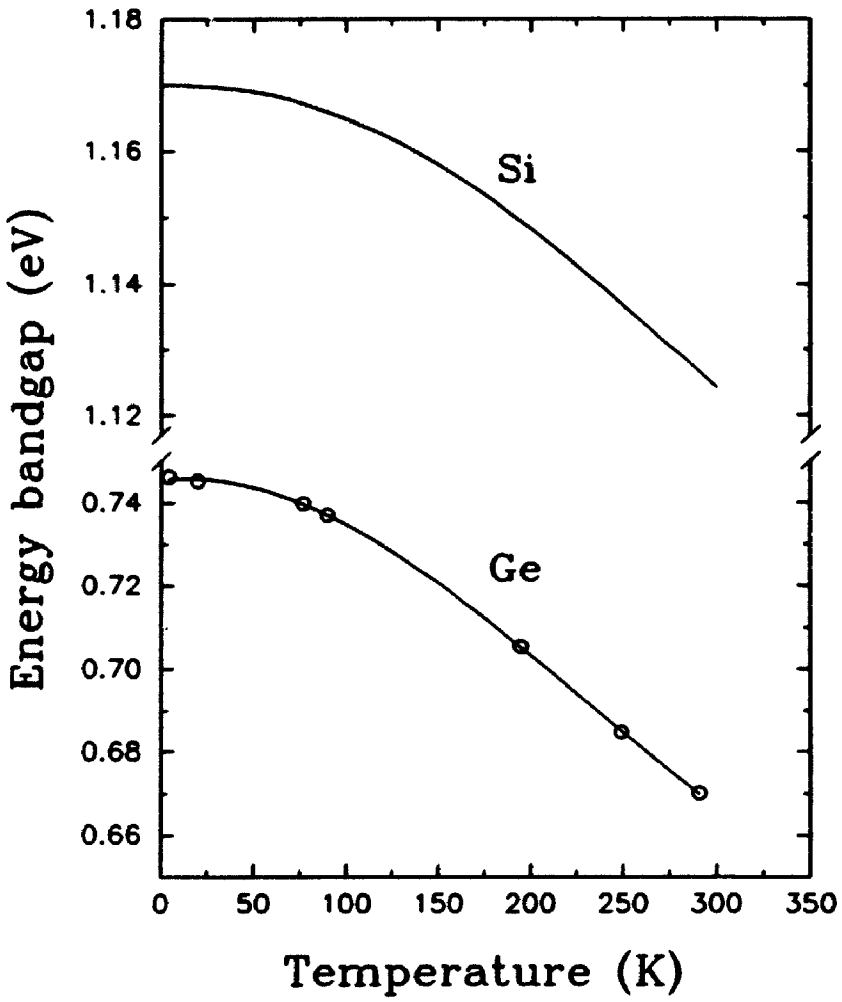

Figure 2.6 Temperature dependence of the indirect bandgap in Si and Ge semiconductors.

2.4 Ionization energy in Si and Ge semiconductor detectors

Figure 2.8 shows experimental results for the temperature dependence of the ionization energy in Si detectors, measured in the late 1960's and early 1970's. The

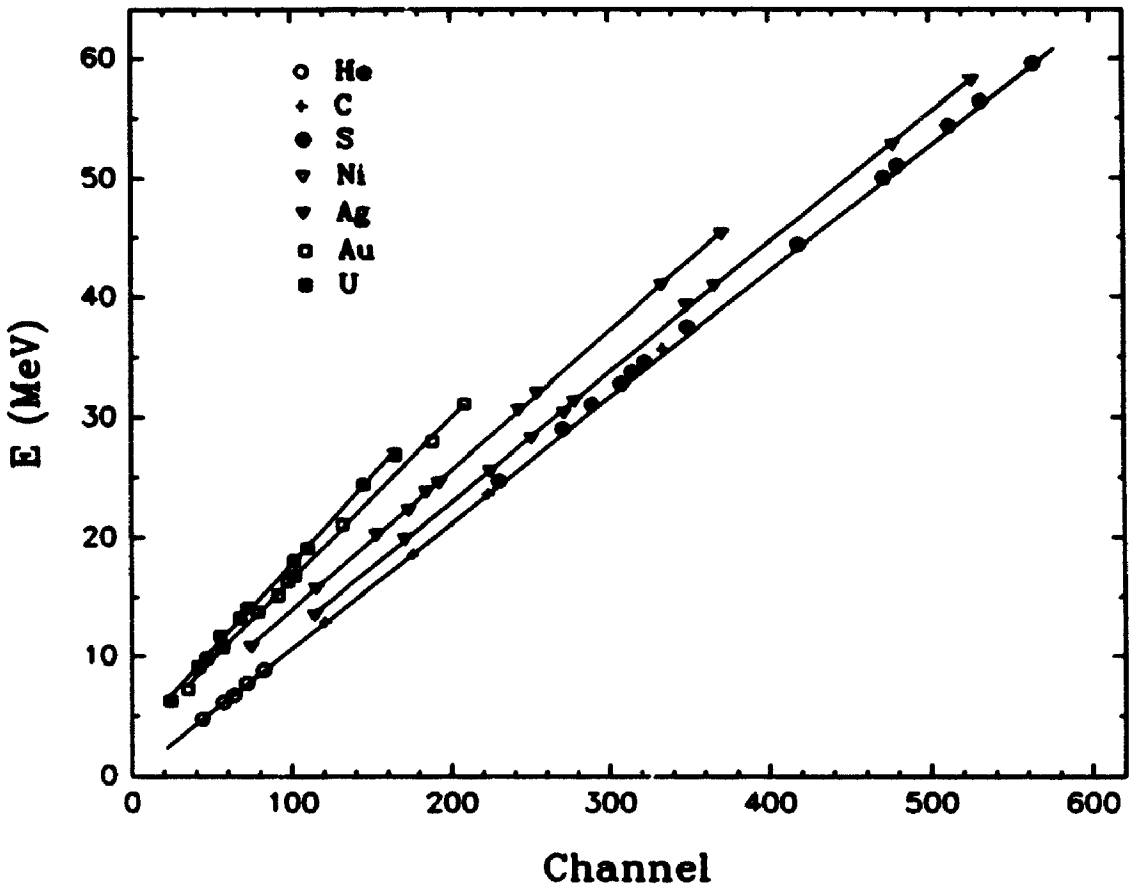

Figure 2.7 The energy of ions versus the measured pulse height (in channel number) obtained using a Si surface barrier detector (taken from ref. 15).

data exhibit the same tendency of ε versus temperature and the difference of $\varepsilon_{0.e}$ and ε_{α} is ~1% in each experiment. But the absolute values of ε vary from one experiment to another, which may be due to a different charge loss in collection of electron–hole pairs. It is not very clear from the reports if and how the window and nuclear energy losses for α particles have been determined and how the temperature dependence

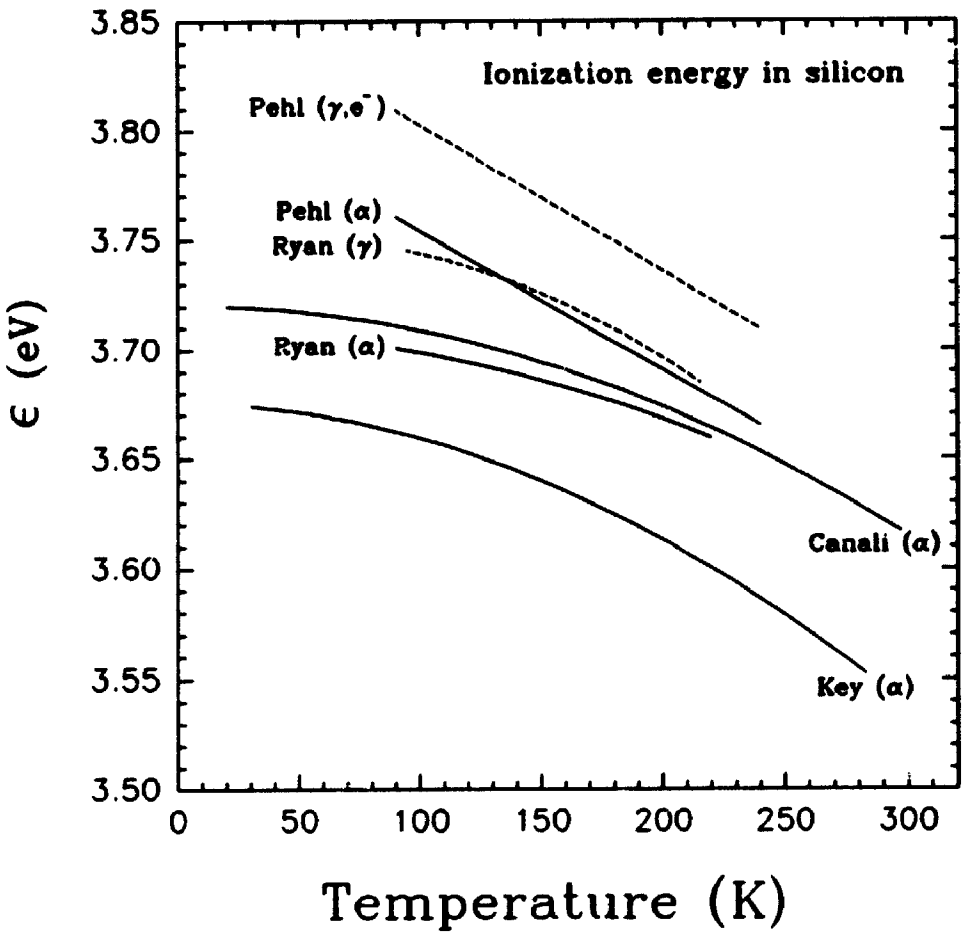

Figure 2.8 Temperature dependence of the ionization energy measured for α, e^-, and γ in Si semiconductor detectors (after ref. 19).

of the window energy loss was considered, which may affect the linear relationship between ε_α and the energy bandgap of the semiconductor derived from experiments. The energy dependence of ε_{ion} in Si detectors has been carefully studied [18]. For light ions, the number of electron-hole pairs, N_{eh}, was described by

$$N_{eh} = \int_{\Delta E_n}^{E} \frac{dE'}{\varepsilon_{ion}(E)} = \int_{\Delta E_n}^{E} \frac{dE'}{\varepsilon_0 - k(dE/dx)} \qquad (2.11)$$

where $E=E_{ion} - \Delta E_w$, ΔE_w is the window energy loss, ΔE_n is the nuclear energy loss,

dE/dx (dE/dx>0) is the stopping power for ions and k is a constant having the value 2-3 × 10^{-4} nm/e-h pair. Figure 2.9 shows the schematic of the energy dependence of $\varepsilon_{ion}(E)$ for protons and α's in Si detectors, based on $\varepsilon_{ion} = \varepsilon_0$ - k(dE/dx), where

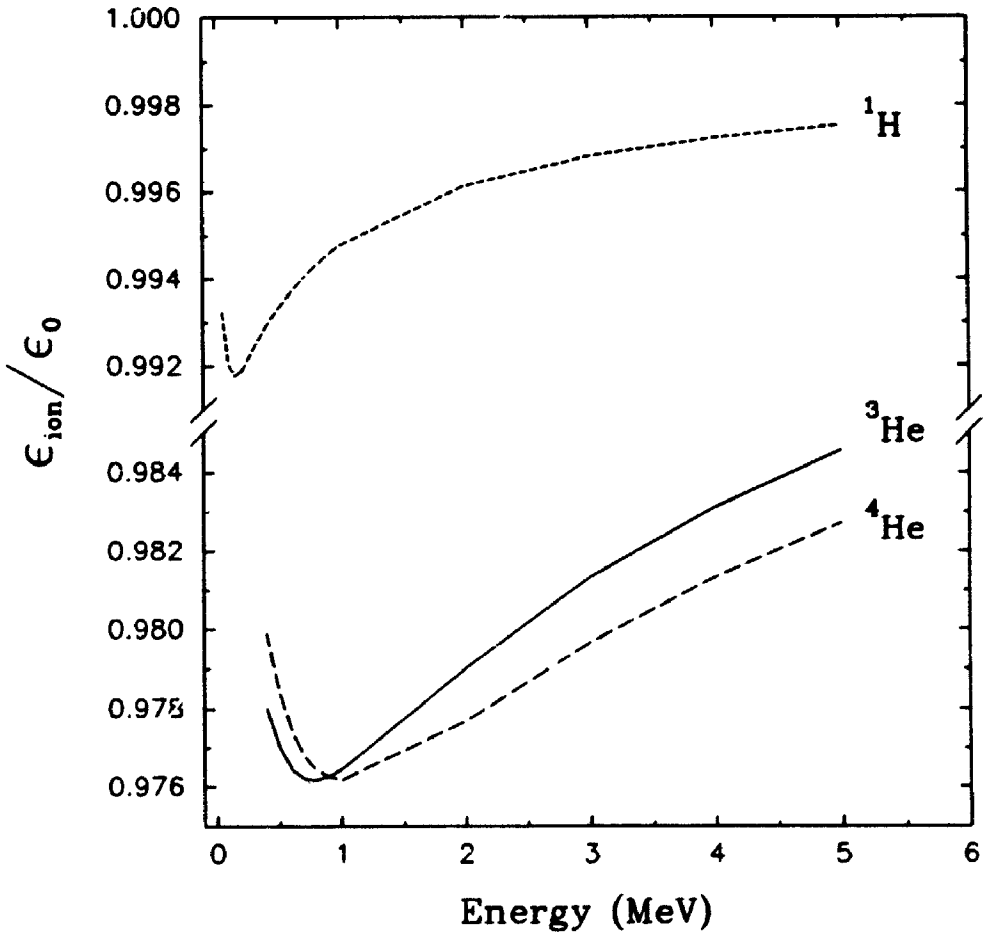

Figure 2.9 Energy dependence of the $\varepsilon_{ion}/\varepsilon_0$ for p and α in Si semiconductor detectors, predicted by Lennard et al [20].

k = 2.8 × 10^{-4} nm/e-h pair. The experimental study [21] has shown that $\varepsilon_{ion} = \varepsilon_0$ − k(dE/dx) is not quite suitable for heavy ions. ε_{ion} changes very slowly with increasing stopping power above the value of 1.5 keV/nm. The plasma effect needs

to be considered, since the local plasma is so dense that strong electric fields are not likely to penetrate.

Figure 2.10 exhibits the temperature dependence of ε_α and ε_0 for Ge detectors [22]. No difference was found between ε_α and ε_0 within experimental uncertainty.

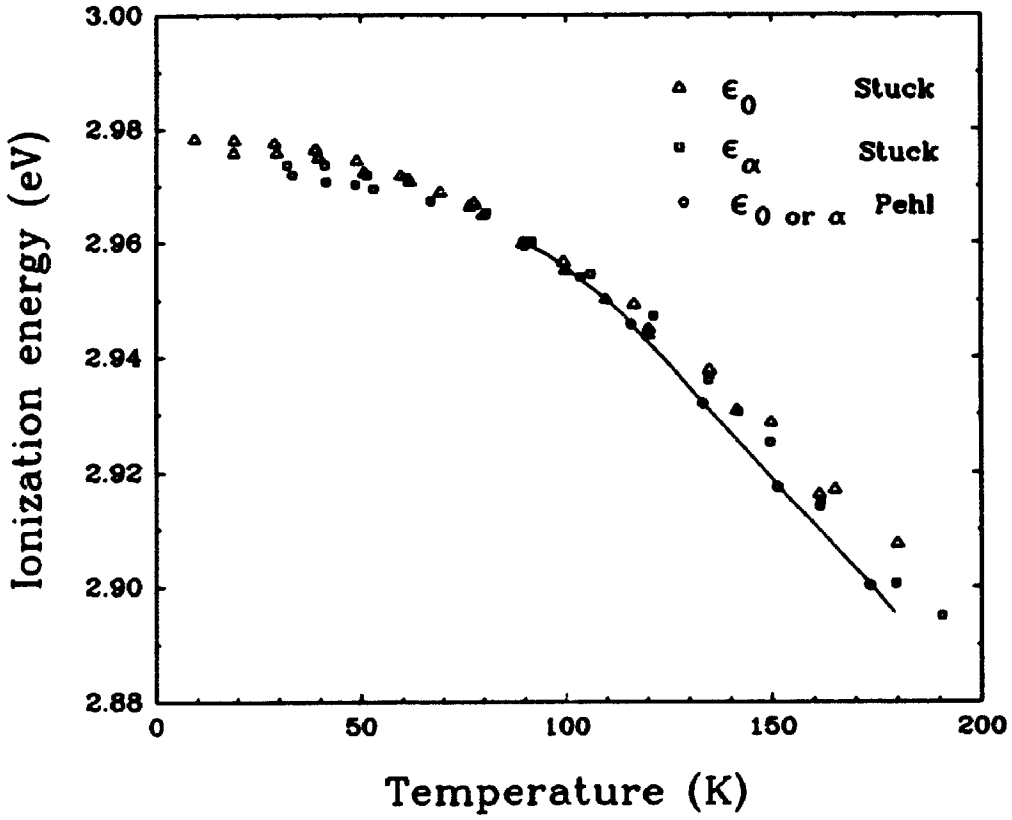

Figure 2.10 Temperature dependence of the ionization energy measured for α and γ in Ge semiconductor detectors.

A linear dependence of $\varepsilon_{0,e}$ on the Ge energy bandgap was observed. Again, corrections for the window and nuclear energy losses were not discussed in detail.

For the energy dependence of the ionization energy, data are only available

for p, d, and α particles in the energy range 10-19 MeV, which shows little energy dependence of ε for light ions and $\gamma-$rays in Si and high purity Ge detectors. This observation suggests that at high velocities, the ionization energy of energetic ions will approach ε_0 in both Si and Ge detectors.

References

1. A. Grab, J. J. Grob and P. Siffert, Nucl. Instr. and Meth. 132 (1976) 273.
2. "Stopping Powers for Electrons and Positrons", ICRU Report 37 (1984).
3. T. Tabata, R. Ito, and S. Okabe, Nucl. Instr. and Meth. 94 (1971) 509.
4. U. Fano, Phys. Rev. 70 (1946) 44; Phys. Rev. 72 (1947) 26.
5. R. D. Evans, "The Atomic Nucleus", Krieger, New York, 1982, Chaps. 26-28.
6. H. R. Bilger, Phys. Rev. Vol.163 (1967) 238.
7. G. F. Knoll, "Radiation Detection and Measurement", Wiley, 1989.
8. G. Bertolini and A. Coche, "Semiconductor Detectors", North-Holland Publishing Company, Amsterdam, 1968.
9. F. S. Goulding and R. H. Pehl, "Semiconductor Detectors", Section IIIA in Nuclear Spectroscopy and Reactions, J. Cerny, ed. Academic Press (1974).
10. J. W. Mayer and E. Rimini, "Ion Beam Handbook for Material Analysis", Academic Press, Inc. 1977.
11. H. W. Schmitt, J. H. Neiler, F. J. Walter and R. J. Silva, Bull. Am. Phys. Soc. 6 (1961) 240.
12 D. J. Dunstan, JAERI Annual Report (1987) 171.
13 G. G. Macfarlane, T. P. McLean, J. E. Quarrington and V. Roberts, Phys. Rev. 108 (1957) 1377.
14. C. D. Moak, J. W. T. Dabbs and W. W. Walker, Rev. Sci. Instr. 37 (1966) 1131.
15. B. D. Wilkins, M. J. Fluss, S. B. Kaufman, C. E. Gross and E. P. Steinberg, Nucl. Instr. and Meth. 92 (1971) 381.

16. E. C. Finch, Nucl. Instr. and Meth. A257 (1987) 381.

17. M. Ogihara, J. Nagashima, W. Galster and T. Mikumo, Nucl. Instr. and Meth. A251 (1986) 313.

18. See refs. 10-12 in Chapter 1.

19. R. Stuck, J. P. Ponpon, R. Berger and P. Siffert, Rad. Effects 20 (1973) 75.

20. W. N. Lennard, H. Geissel, K. B. Winterbon, D. Phillips, T. K. Alexander and J. S. Forster, Nucl. Instr. and Meth. A248 (1986) 454.

21. D. Comedi and J. Davies, Nucl. Instr. and Meth. B67 (1992) 93.

22. R. H. Pehl, F. S. Goulding, D. A. Landis and M. Lenzlinger, Nucl. Instr. and Meth. 59 (1968) 45.

Chapter 3

EXPERIMENTAL SETUP AND CALIBRATION

The study of the response of Ge semiconductor detectors to ionizing radiation requires precise measurements of the energies of the incident radiation and precise control of the experimental conditions. The experimental setup comprises the Ge detector/working chamber, beam flight line, scattering chamber, signal processing system, power supply and reference pulse device. Experimental parameters such as vacuum, noise, temperature control, pulse shaping, linearity of the whole system, thickness of beam scattering foils, *etc.* are the crucial factors to be adjusted or determined.

3.1 Test chamber for Ge detector

The detector chosen for this study was an Ortec HPGe charged particle detector (Serial No. 30-338A, Model No. GG−020−075−7) with an active area of 75 mm^2 and a maximum sensitive depth of 9.8 mm. The front surface of the detector was a 40 keV boron-implanted layer (implantation dose 10^{14} ions cm^{-2}); the back contact was a 300 μm lithium diffused layer. The operating bias applied to the detector was 1000V although total depletion was obtained for approximately 400V. Under the operating bias, the electric field of 1 kV/cm in the detector corresponds to a drift velocity of ~8 × 10^6 cm/s for electrons and holes at T ≈ 80K, which is very close to the saturated drift velocity value [1,2]. The specified detector capacitance when fully depleted is ~7 pF. Initially, a Ge detector fabricated by R. H. Pehl's

group at the Lawrence Radiation Laboratory was used. Unfortunately, the detector's operation was unsuccessful, which was possibly due to surface contamination occurring during transit.

The experiments were performed in a high-vacuum chamber (volume ~500 cm^3) in which the Ge detector was housed. Figure 3.1 shows a schematic diagram

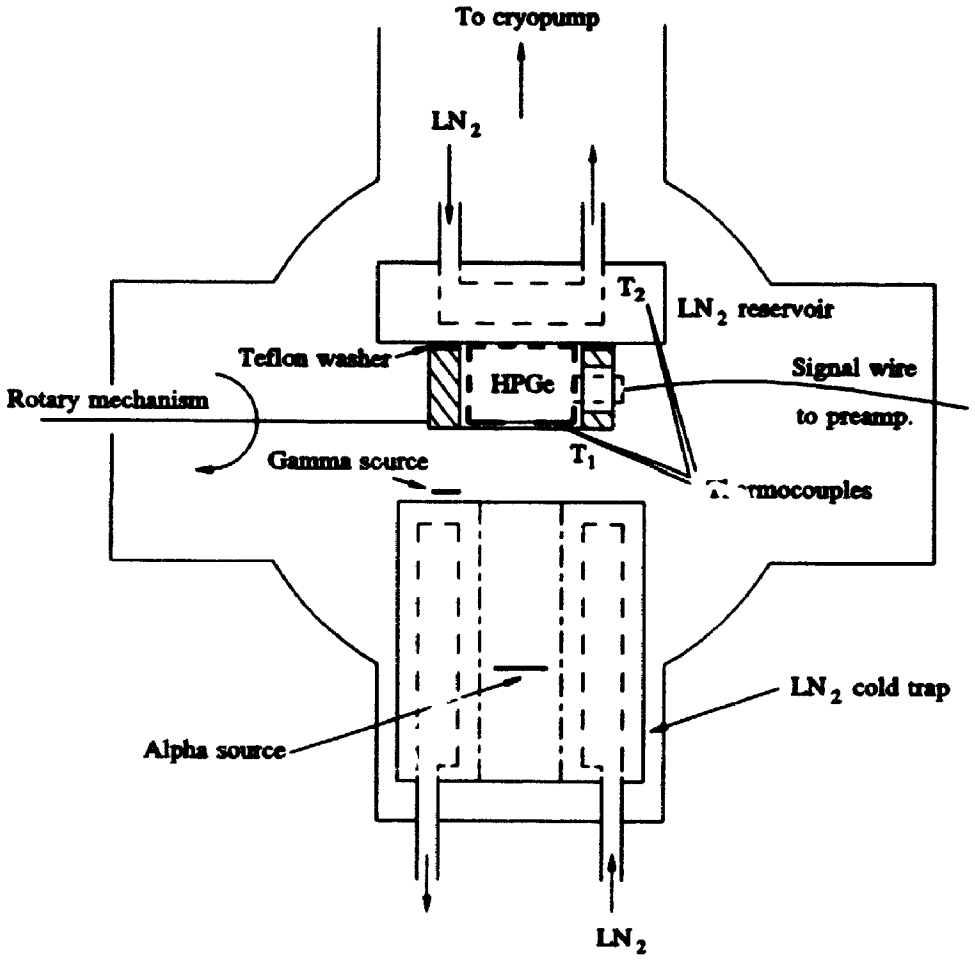

Figure 3.1 Test chamber for the Ge detector for the simultaneous measurement of $\gamma-$ and $\alpha-$spectra using radiative sources. The γ source was removed for the application of ion beams.

of the experimental setup. In the chamber, the rear surface of the planar detector is tightly fastened to a massive copper mount which is in the form of a cooling reservoir. An indium foil gasket was used to make good thermal contact at the interface. The detector mount system was placed on the axis of a high precision rotary mechanism with the rotation axis passing through the front surface of the detector. The mounting allowed the detector to be tilted to any angle between ± 50° (with respect to the surface normal) with an uncertainty of ±0.017°. Thermal isolation between the detector mount and the rotary mechanism was assured via four small teflon fittings. Two metal bellows were connected to the cooling reservoir in order to provide for fast LN_2 cooling while at the same time maintaining adequate rotating flexibility of the detector. By using a continuous flow of LN_2 through the mounting assembly, the detector could be cooled from room temperature to 80K within 20 min. The temperature was monitored by two thermocouples: one was placed on the front surface of the detector chassis and another was directly in contact with the LN_2 reservoir. In order to search for temperature gradients within the detector assembly, the thermocouples and their connecting wires were calibrated at three temperatures: 77K, 195K and 273K. Less than 0.6K difference was found between the readings from the two thermocouples over the temperature range 80K−170K (see Figure 3.2), thereby indicating that the temperature distribution in the detector was uniform, *i.e.* the heat loss through the signal wire and other contacts was negligible. The face of the detector was surrounded by a large LN_2−cooled cold trap which provided a substantial improvement in the local vacuum and suppressed condensation on the Ge crystal surface. In the experiments, this trap was cooled for

approximately 30 min before cooling the detector housing itself. Using a 4000 l/s cryopump, the test chamber was evacuated to a pressure of ~1.3×10^{-6} Pa.

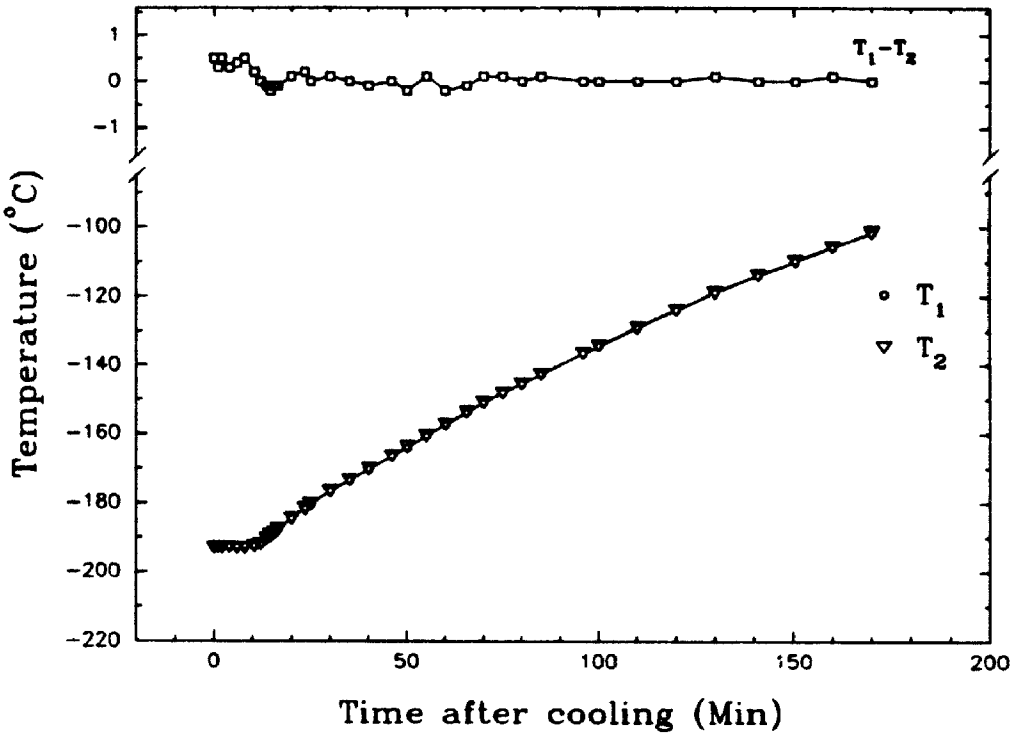

Figure 3.2 The behaviour of the temperature of the detector front chassis and the wall of the LN_2 reservoir (with warm LN_2 trap). The top curve marked with $T_1 - T_2$ represents the temperature difference of the detector with its reservoir.

The setup shown in Figure 3.1 corresponded to that used for experiments with radioactive α–sources. A circular α–sources was used in the experiments: a mixed source containing the α–emitters ^{239}Pu, ^{241}Am and ^{244}Cm (E_α = 5157, 5486 and 5805 keV, respectively [3]), with an active area ~5 mm^2. The distance between the detector and the α–source was ~7 cm. A variety of γ–ray sources (^{152}Eu, ^{60}Co,

^{137}Cs, ^{133}Ba, ^{54}Mn, ^{22}Na) was used for calibration purposes during the course of these measurements.

The setup of the test chamber when using incident ion beams from the accelerator was slightly different from that in Figure 3.1: specifically, the front port of the chamber (*i.e.* the bottom port shown in Figure 3.1) was connected to a large vacuum vessel (denoted the 'time-of- flight', or T-O-F, chamber) and associated beam line to introduce the beam through to the detector with the α−source removed.

3.2 Electronic system

The electronic setup for the Ge detector consisted of the detector, preamplifier, amplifier, multichannel analyzer, a reference test pulse generator as well as the detector power supply, see Figure 3.3. One of the major considerations

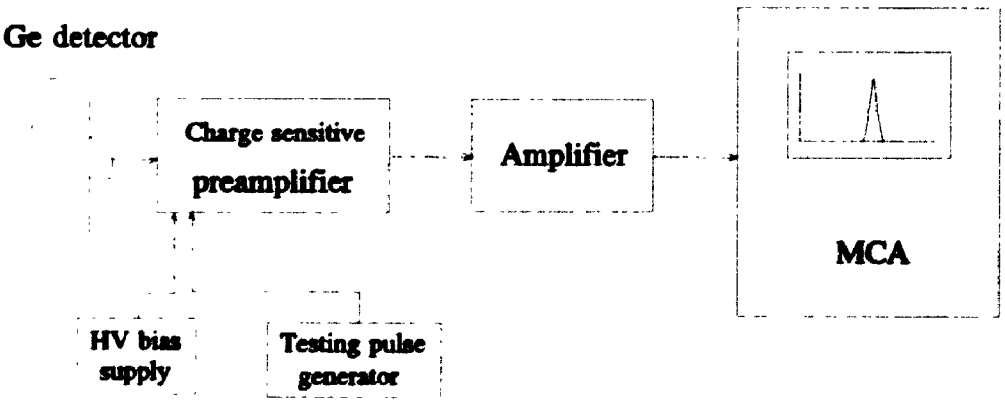

Figure 3.3 Schematic diagram of the Ge detector and its associated electronics. The Ge detector is in the vacuum chamber and the preamplifier is directly mounted to the flange of the test chamber.

concerned the minimization of the electronic noise level. Since the noise picked up between the detector and preamplifier controls the signal/noise ratio, which is independent of the input capacitance, noise reduction for this component was a priority. The best method chosen from several configurations that were tested resulted in grounding the detector chassis (*i.e.* the bias voltage had negative polarity) through its mount to the chamber, using a short (~25 cm) coaxial signal wire (with a reasonable spacing between the signal wire and the shielding) between the detector and the preamplifier; the preamplifier was directly attached to the vacuum chamber flange so that the input wire passed through the flange into the vacuum chamber without any connector. To prevent any other effect from changing cables between the electronic devices, exactly the same cable was used for each connection. The charge sensitive preamplifier was a Model 5091 (Electron Control Corporation, eV Products Division), providing low noise (~0.7 keV FWHM, according to manufacturer's specification sheets) for a load capacitance of 0−100 pF; with an Ortec 142AG preamplifier, the comparable figures were 3 keV at 0 pF and 5 keV at 100 pF. The pulse rise time for the eV−5091 preamplifier was ~9 ns using a 22 pF load capacitance. The eV-5091 preamplifier was thus found to be superior to the Ortec 142AG for the present measurements.

The main amplifier (Ortec 572) used a shaping time of 1 μs; variation of this parameter in the range 0.5−4 μs produced no observable change in the relative pulse heights. The pole−zero of the amplifier was optimized, and the pileup rejector was used although the total count rate was always $\leq 10^3\ s^{-1}$. The γ−ray resolution was best using 1 μs shaping time. Since the signal risetime in the detector is at most ~125

ns, *i.e.* much shorter than the shaping time, this shaping time of 1 μs was therefore a reasonable choice. The actual risetimes for γ−rays ranged from ~50 to ~85 ns as measured using a Tektronix 2430A digital oscilloscope.

Two types of multichannel analysing systems were used: (i) a Canberra Series 90 (MCA1) for measurements using α−sources, and (ii) a Nucleus PC MCA (MCA2) for measurements using accelerated ion beams. All spectra were recorded in a 4096 channel MCA and stored in a computer for later analysis. The total system resolution for MCA1 was ~2.8 keV for 1.4 MeV γ−rays and ~14.7 keV for 5.5 MeV α−particles (^{241}Am); for MCA2, the corresponding values were ~3.1 keV for 1.4 MeV γ−rays, ~6 keV for 1 MeV protons and ~16 keV for 2.5 MeV ^{4}He ions. A precision pulse generator operated at 60 Hz was used to relate measured pulse heights, thereby eliminating any nonlinearity in the analog-to-digital converter (ADC). The output pulse height of the pulse generator was controlled by a precision Kelvin-Varley voltage divider containing 3−decade dial switches and a variety of attenuator switches. The (input) risetime for the test pulses was ~30 ns; after the preamplifier, the risetime became ~38 ns. The offset of the reference pulse corresponding to a dial reading of zero was adjusted to yield a zero output. The maximum pulse heights for both 1.3325 MeV γ-rays and test pulses close to the γ peak was reached for a shaping time of 1 μs; thus, the ballistic deficit [4−6] of the amplifier should be minimized.

3.3 Calibration of the test pulse against γ-rays

In order to eliminate non-linearity in the ADC, the pulse output of the

precision generator was used as a reference in all spectra. The linearity of the pulse generator was confirmed for γ−ray energies from 0.1 to 1.4 MeV by using three different Ge detector-preamplifier combinations and different pulse amplitudes with the same amplifier-ADC system, since the photopeak pulse height is known to be precisely linear with γ−ray energy [7]. The differential linearity of the pulse generator for all pulse amplitudes was found to be better than 1.5×10^{-4}% for both a 200 cm^{-3} planar HPGe spectrometer and a 92 cm^{-3} coaxial Ge(Li) spectrometer (resolution ~1.7 keV for both) at LN_2 temperature, and 0.04% for the Ortec HPGe detector at 80K. The temperature dependence of the linearity was only examined for the Ortec HPGe detector with the Ortec 572 amplifier and MCA2 system for the temperature range 80K-165K, and similar results were found. For the Ortec HPGe detector, the small photopeak efficiency was the limiting factor in the precision of the linearity measurements. It was verified that the pulse height measured for γ−rays was independent of the geometrical orientation of the γ−ray source with respect to the HPGe detector. To determine precisely the positions of γ peaks and the test pulses in the calibration spectra, both peak centroids and the most probable positions determined by a near-Gaussian fitting procedure were used - no difference was found between the two choices. Test pulses were placed on both sides of each γ peak; the pulse values were cycled in time during the accumulation of the γ-rays to minimize small electronic instabilities. Each γ peak position in test pulse height units (called P.H.U. - dial number of the test pulse) was derived by a linear interpolation from the positions of its two satellite test pulses, which is based on the reasonable assumption that the MCA is linear within a short range of channels, *i.e.*

$$P_\gamma = \frac{(P_1 - P_2)}{(C_1 - C_2)} \times (C_\gamma - C_1) + P_1 \qquad (3.1)$$

where P_1, P_2, P_γ represent the peak positions for the two satellite test pulses, and γ−rays in P.H.U., and C_1, C_2, C_γ denote the same peak positions in the channel numbers of the MCA. The zero offset of the pulse generator was minimized and had a negligible effect on the interpolated data compared with uncertainties arising from other sources. Even so, the calibration data were still fitted by

$$E_\gamma = A * P_h + B \qquad (3.2)$$

where P_h is the photopeak pulse height (in P.H.U.) of the γ−rays having an energy of E_γ (MeV) and A and B are fitting parameters representing the slope (MeV/P.H.U.) and intercept (MeV), respectively. Figure 3.4 shows an example of the calibration of the test pulse against ^{152}Eu γ−ray energies at 80K, with the data listed in Table 3.1. The temperature−dependence of the calibration and the data are displayed in Figure 3.5 and Table 3.2, respectively.

Table 3.1 ^{152} Eu γ−ray energies and their pulse height values at 80K

^{152}Eu	γ_1	γ_2	γ_3	γ_4	γ_5	γ_6	γ_7
E_γ (MeV)	0.244693	0.344272	0.778850	0.964007	1.085815	1.112050	1.40806
PH(P.H.U.)	0.070224	0.098794	0.223458	0.276510	0.311472	0.319043	0.403895

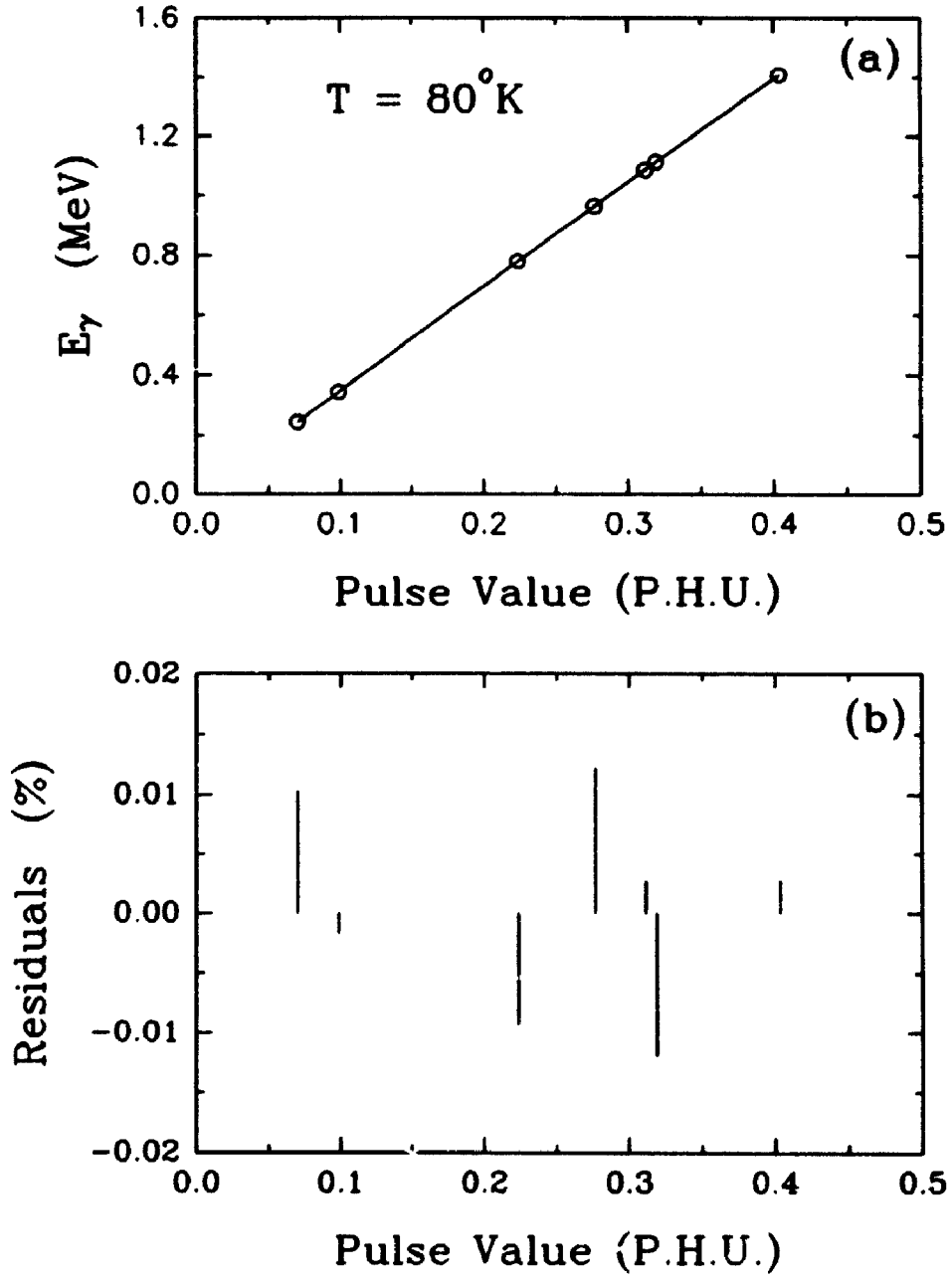

Figure 3.4 (a) An example of the γ−test pulse calibration; the linear fit, $E_\gamma = A\,P_h + B$, shows A = 3.48653 ± 0.00030 MeV/P.H.U. and B = (−1.70 ± 0.80) × 10^{-4} MeV. (b) Residuals (experimental value - fitted value) at each data point. These are expressed as a percentage of the fitted value; see Table 3.1 for the data.

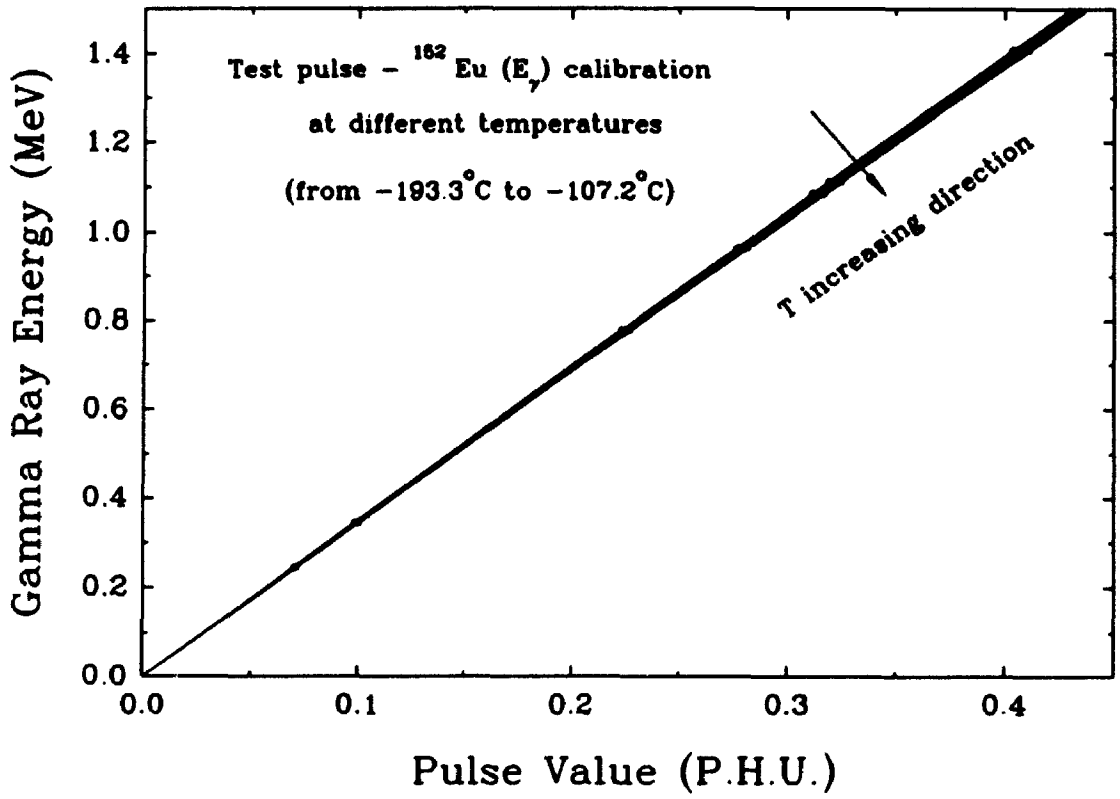

Figure 3.5 Temperature dependence of the γ−test pulse calibration. The linear fitting parameters, A and B, are listed in Table 3.2. Each set of data are obtained over a period of temperature change of 2°C, except for the lowest temperature.

Table 3.2 Temperature dependence of the γ−test pulse calibration

Temperature (°C)	B ($\pm \leq 8.0 \times 10^{-5}$) MeV	A ($\pm \leq 3.0 \times 10^{-4}$) MeV /PHU
-193.3	9.34476×10^{-5}	3.4864683
-189.1	-1.67794×10^{-5}	3.485071
-179.4	-1.77984×10^{-4}	3.479861
-169.1	-2.44322×10^{-5}	3.473704
-159.0	8.94977×10^{-5}	3.466577
-148.9	1.17610×10^{-4}	3.460052
-138.5	-9.36104×10^{-5}	3.451891
-127.4	7.78793×10^{-5}	3.443838
-119.5	3.12891×10^{-5}	3.436358
-107.2	1.23914×10^{-4}	3.427676

3.4 The setup and targets for beam application

The UWO 1.7 MV Tandetron ion accelerator was used as a tunable source of energetic ions. The schematic of the setup is shown in Figure 3.6: after momentum selection, the ion beam was steered (via the 45° beamline) into the T-O-F scattering chamber. The ion beam direction was determined by two adjustable apertures having a separation of 1 m. The beam focus was adjusted by a quadrupole located upstream from the analysing magnet. A target holder capable of holding up to 10 samples was located in front of the T-O-F chamber. The target holder could

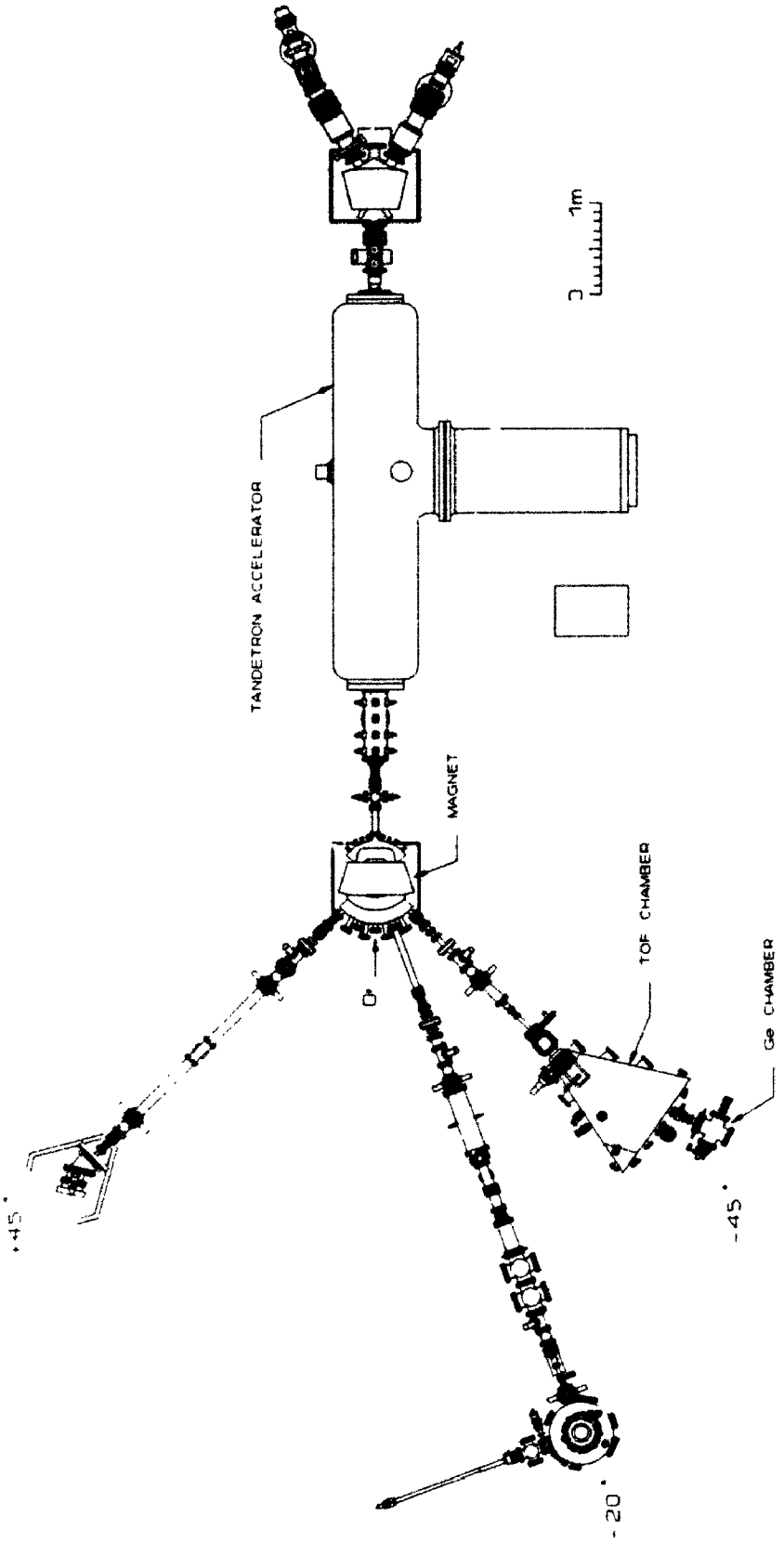

Figure 3.6 a Schematic of the Tandetron accelerator and the associated beam lines.

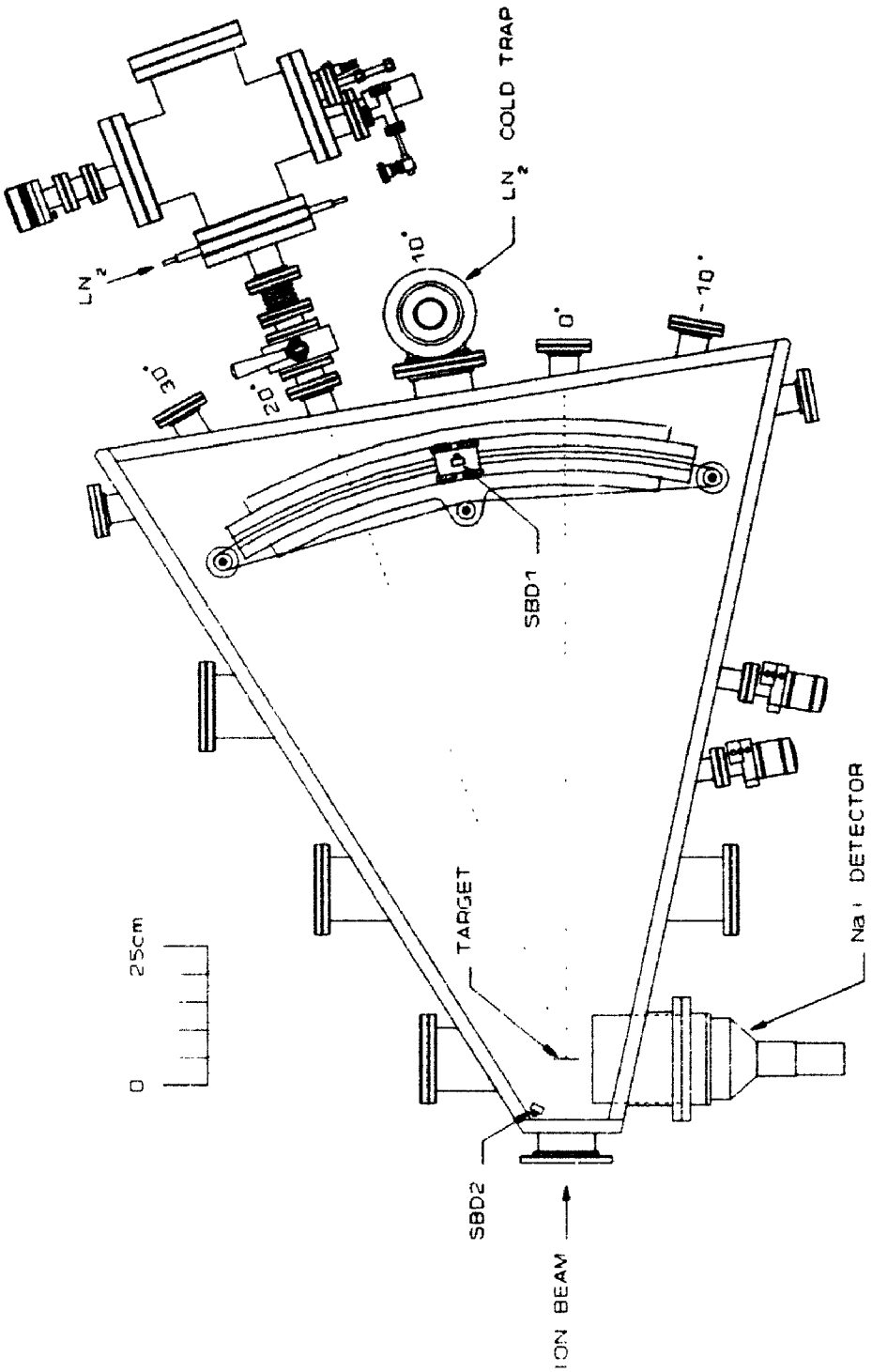

Figure 3.6 b Schematic of TOF chamber and the Ge detector chamber.

be tilted about its vertical axis which passed through the surface of thin targets. The target holder was electrically isolated from the frame of the vacuum chamber and equipped with a front secondary electron suppression plate, thereby providing for reasonably accurate beam current integration from the target. The direction of the beam was aligned with the centre of the target holder and the centre of the 0° port at the back of the T-O-F chamber. The Ge working chamber was connected at the 20° port position at the back of this chamber; the circular detector subtended a solid angle, $\Omega = 1.8 \times 10^{-6}$ sr. (±10%) with respect to the beam spot at the position of the target holder.

The incident beam was scattered through a self−supporting thin foil mounted on the target holder to forward directions, including the direction of 20° to the Ge detector. The intensity of the scattered beam is governed by the Rutherford scattering cross section and the intensity of the incident beam. A movable Si detector (SBD1) on the 'railway track' at the back of the T-O-F chamber was used to monitor the intensity of the scattered beam to ensure that the scattered beam intensity was low enough to avoid any catastrophic damage to the Ge detector.

Three group of targets were mounted on the target holder in the T−O−F chamber for different purposes: (1) a quartz and a phosphor target, which could be fluoresced by the beam to give a visual indication of the beam spot location to ensure that the ion beam impacted at the desired spot on the target; (2) thin Al (35 $\mu g/cm^2$), ^{13}C (12 $\mu g/cm^2$) and CaF_2 (74 $\mu g/cm^2$) targets with Ta backings to facilitate the energy calibration of the accelerator (see next section); (3) a thin Au self−supporting foil (ρt=68 $\mu g/cm^2$) and a Au/C (sandwich target) self−supporting foil (ρt_{Au}=9.6

$\mu g/cm^2$ and ρt_C=11.2 $\mu g/cm^2$) used to scatter the beam . An additional ^{12}C (7.3 $\mu g/cm^2$) target on a silicon substrate was also used in another chamber for the purpose of the energy calibration, see below.

In the experiments, the thin self–supporting Au foil was used to scatter the proton beam, and the self–supporting Au/C foil was used to scatter heavier ion beams. A fixed Si detector (SBD2) with an aperture of 5 mm diameter, located at a distance 12 cm away from the reference point of the target holder at a scattering angle of 152.3° with respect to the beam direction, was used to record the intensity of backscattered particles. First of all, this setup was purposely set for measuring the thicknesses of the scattering foils, in order to determine the energy of the scattered ions precisely. Secondly, this setup also eliminated the need to transfer these delicate foils to a different location for analysis.

The thicknesses of the thin scattering foils were determined via Rutherford backscattering *in situ*. The Rutherford backscattering analysis [8] is a nondestructive method based on detecting the incident ions elastically backscattered from the target. The yield (Y) or number of the scattered ions recorded by a detector at a laboratory scattering angle, θ, follows

$$Y = Q_b \, \Omega \, \sigma_{sc}(\theta, E) \, N_t \qquad (3.3)$$

where Q_b is the number of the incident ions, Ω is the solid angle subtended by the detector, N_t is the target foil thickness in atoms/cm^2, $\sigma_{sc}(\theta, E)$ is the screened Rutherford scattering cross section [9], and E is the average energy of the projectile ions in the target foil. σ_{sc} can be written as

$$\sigma_{sc}(\theta, E) = \frac{Z_1^2 Z_2^2 F(Z_1, Z_2, E) f(\theta)}{E^2} \tag{3.4}$$

where $F(Z_1, Z_2, E)$ is the screening correction factor due to incomplete penetration of the incident ion (Z_1, M_1) through the electron shells of the target atom (Z_2, M_2) and $f(\theta)$ is the angular factor depending on both the mass ratio M_1/M_2 and θ.

The screened cross sections can be calculated. By comparing with the yield from the thin target with known thickness, the thickness of the unknown target foil, N_t, can be easily obtained

$$N_t = N_t' \frac{YQ_b'}{Y'Q_b} \frac{\sigma_{sc}'}{\sigma_{sc}} \tag{3.5}$$

where the primed and unprimed quantities refer to targets of known and unknown thickness, respectively. A Si(Bi) target with a surface Bi concentration of 4.9×10^{15} atoms/cm^2 ($\pm$ 2%) was employed as a standard target. The analysis beam was 1.5 MeV ^{4}He with ~30 nÅ ($\pm$ 2nÅ) beam intensity and a size of 2×2 mm^2. The spectra were recorded by SBD2 for a normally incident beam (for instance, see Figure 3.6b). The yield of ions backscattered from the C and Au in Au/C self-supporting foil correspond to the areas of C and Au peaks in the spectrum. Therefore, the results are ρt=68 μg/cm^2 for Au self-supporting foil, and ρt_{Au}=9.6 μg/cm^2 Au and ρt_C=11.2 μg/cm^2 C for Au/C self-supporting. foil with 10% uncertainties. Note that σ_{sc} is known as the (screened) Rutherford elastic cross section at the energy used above, especially for $\alpha\rightarrow$C scattering [10].

3.5 Energy calibration of the Tandetron accelerator

The energy calibration of the Tandetron ion accelerator was a critical factor

in minimizing uncertainties in this experiment. Since the energy of accelerated ions depends on the charge of the ions and the terminal voltage (GVM) reading, the energy calibration involved a calibration of the GVM reading (in MV) of the accelerator. Assume that negative ions are extracted from the ion source; the energy of the ions after acceleration is

$$E_{ion} = (1+q)\ eV_R + eV_{inj} \tag{3.6}$$

where q is the charge state of the ions after the stripper gas, V_R is the true GVM voltage and V_{inj} is the injection voltage, *i.e.* the sum of the extraction voltage and the preacceleration voltage. Two resonant nuclear reactions were applied for the calibration: (i) the resonance at 991.9 (±0.04) keV with a width of 0.10 keV for the $^{27}Al(p, \gamma)^{28}Si$ reaction (Q=11.586 MeV), and (ii) the resonance at 1747.6 (±0.9) keV with a width of 0.077 keV for the $^{13}C(p, \gamma)^{14}N$ reaction (Q=7.5507 MeV) [11]. By substituting the known resonant energies and the injection voltage into Equation 3.6, the GVM readings can be obtained. The calibration is to establish the assumed linear relationship between the expected GVM reading (V_R) and the actual GVM reading (V_T), by which the true energy of ions can be calculated for known V_T and V_{inj}.

The γ-ray yields from the nuclear reactions were detected by a 5"×5" NaI(Tl) scintillator, which was mounted at a distance of ~8 cm from the targets via a special re-entrant flange, see Figure 3.6b. The total calibration time required to scan both resonances was ~30 min. due to the large detection solid angle. As mentioned before, the thin Al (35 $\mu g/cm^2$) and ^{13}C (12 $\mu g/cm^2$) targets with the tantalum backings were used for the calibrations. The proton beam current on the target was

~200 nA with an area 6−7 mm^2; the suppression voltage used to ensure the integrity of the beam current integration was +200V. The energy for γ−rays produced in the reactions ranged from 4−15 MeV according to their Q-values. Therefore, to improve the statistics of the collected data, the γ yield over 4−15 MeV was integrated for each spectrum. Figure 3.7 exhibits the integrated γ yields from each nuclear reaction as

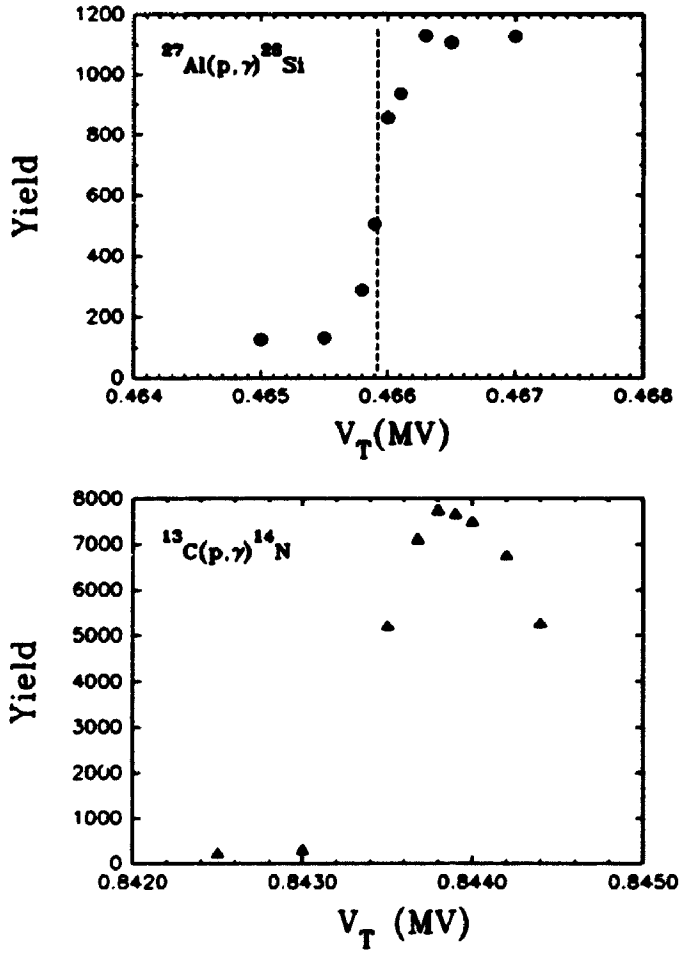

Figure 3.7 Measured γ yield near the resonant energies of 991.9 keV and 1747.6 keV for the ^{27}Al(p,γ)^{28}Si and ^{13}C(p,γ)^{14}N nuclear reactions. The resonant GVM values are: V_T = 0.46592 ± 0.00015 MV at the half way point for the former, and V_T = 0.84380 ± 0.00015 MV at the peak position for the latter (not including the half target thickness correction ~0.00039 MV). E_{inj} = 59 keV.

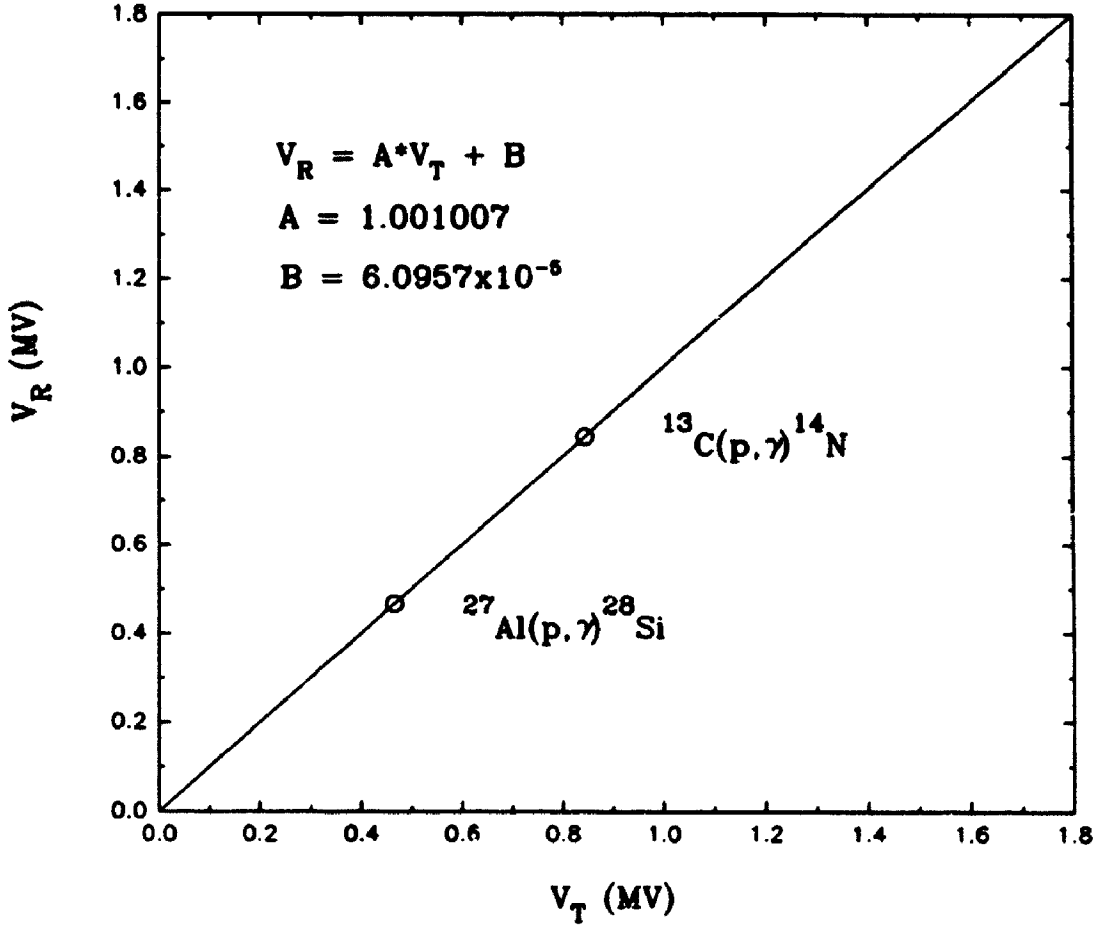

Figure 3.8 The linear relationship between the expected terminal voltage V_R and the actual GVM reading V_T is assumed based on the data from the two nuclear reactions. This has been verified by the additional two points of calibration at low and high energies.

functions of the GVM reading (V_T) in the vicinity of the resonant energies: the same beam dose (*i.e.* integrated charge) was used for each datum in each plot and the data have been corrected for the beam-independent background. The measured V_T at the resonance was chosen as the GVM reading at the half-height between the minimum and maximum yields for $^{27}Al(p, \gamma)^{28}Si$. For $^{13}C(p, \gamma)^{14}N$, the measured resonant V_T was the GVM value at the peak position after correcting for the projectile energy loss

in the thin ^{13}C target. The two calibration points were fitted with a linear function, see Figure 3.8. Therefore, for any given GVM reading V_T, the corresponding beam energy could be derived according to the calibration and Equation 3.6. The typical uncertainty for the resonant V_T was $\leq$0.15 kV, which arose from the instability (~0.1 kV) of the GVM reading and the error in the determination of the resonance position (*i.e.* the measurement). Therefore, the final uncertainty for the ion energies can be calculated, *e.g.* for proton and helium beams, see Tables 6.1 and 6.2. The accelerator was calibrated before and after each pulse height experiment and was found to be very consistent within 0.5 keV at each calibration point over several months.

To ensure the integrity of the above two-point calibration procedure, two further measurements were made: (1) the γ-yield from the $^{19}F(p,\alpha\gamma)^{16}O$ nuclear reaction at 340.46 ($\pm$0.04) keV with a width of 2.4 keV [11] was used to confirm the calibration at low energy; (2) the broad resonance in the $^{12}C(\alpha,\alpha)^{12}C$ elastic scattering yield at a scattering angle of 170° at 4265$\pm$5 keV [12] was scanned to confirm the calibration at higher energies, see Figures 3.9 and 3.10 The extrapolated energy values from the two-point calibration agreed well with the resonant energy within 1.0 keV for the former case and 2.5 keV (the error for measured V_T value is about 0.8 kV) for the latter one. The γ-yield from the $^{24}Mg(\alpha,\gamma)^{28}Si$ nuclear reaction (resonance at 3199.8$\pm$1.0 keV with a width Γ=1.8 keV) was also measured, but the γ-ray yield was not large enough to warrant using this reaction for routine calibration purposes [3].

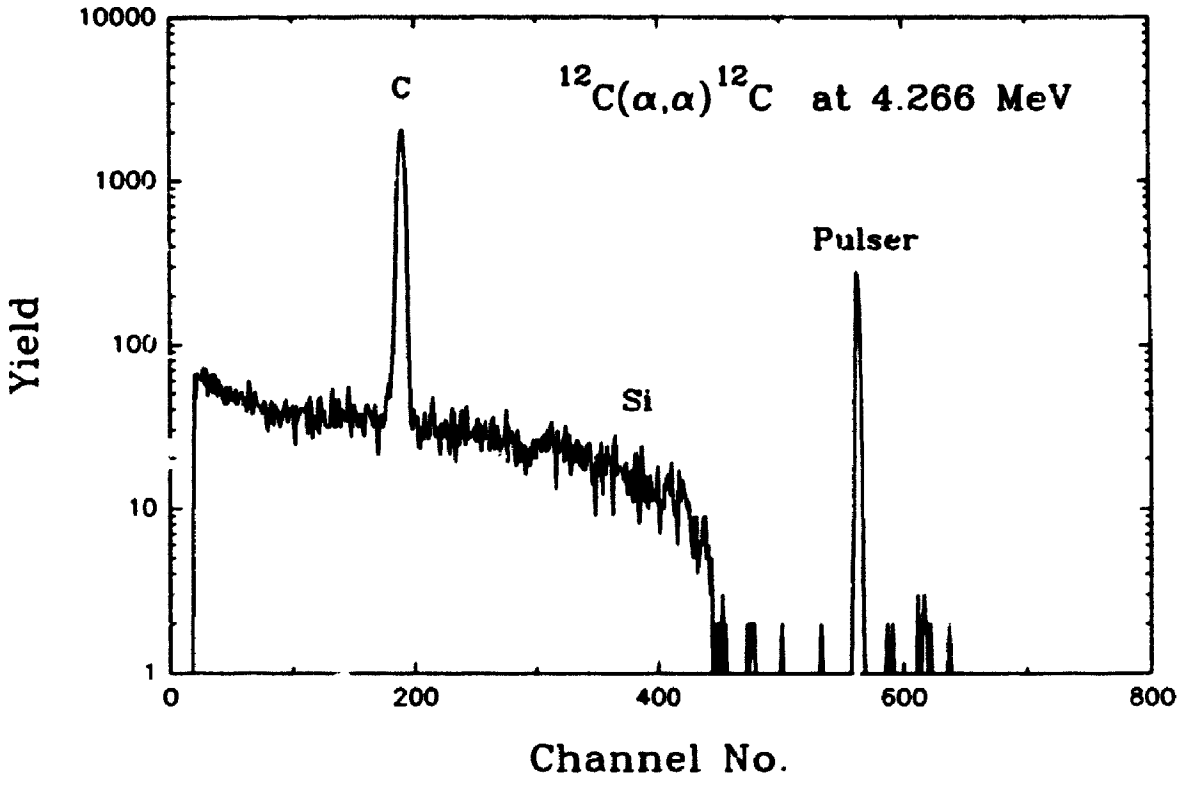

Figure 3.9 Spectrum of $^{12}C(\alpha,\alpha)^{12}C$ resonant scattering at 4.266 MeV, with a prominent carbon scattering yield on top of the continuum Si scattering yield (with slight channeling). The detection angle is 170°.

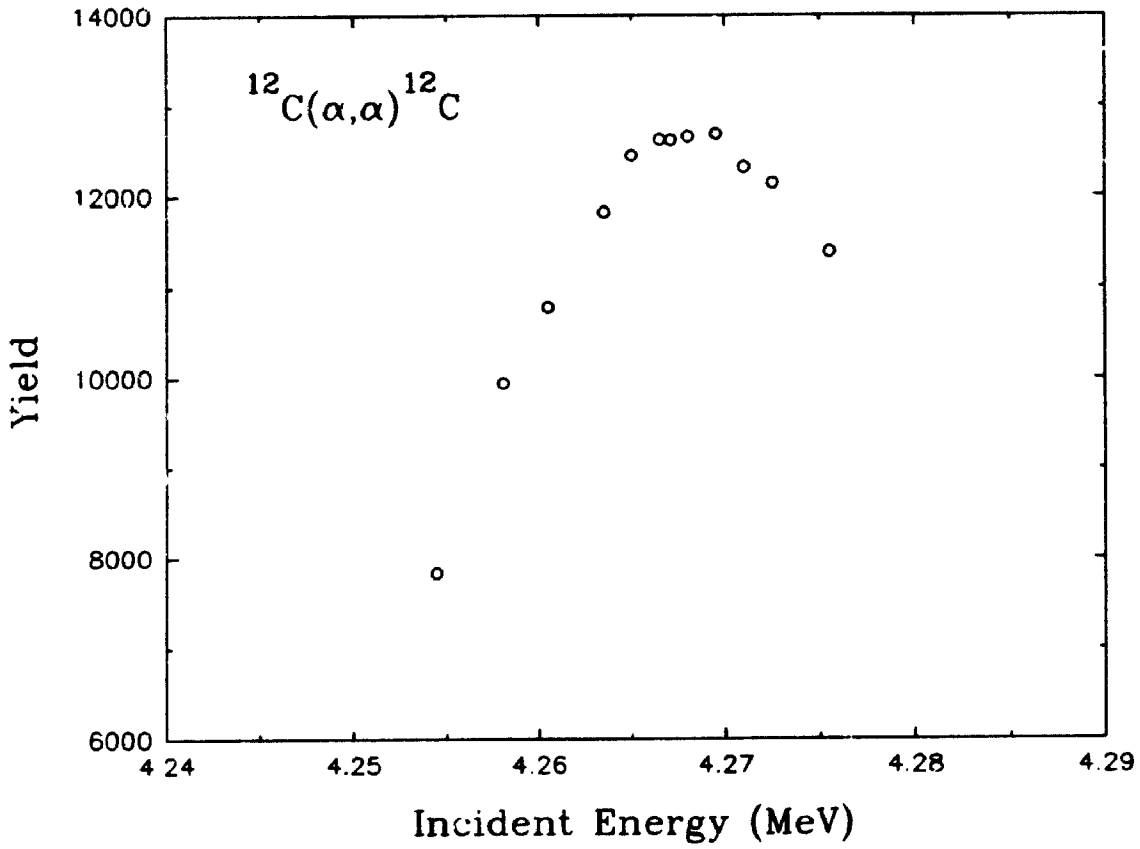

Figure 3.10 The backscattering yield of $^{12}C(\alpha,\alpha)^{12}C$ measured near the resonant energy of 4.265 MeV. The horizontal scale is converted from V_T data based on the two point energy calibration, in which the target thickness correction is included. The resonant energy is found to be 4.2675 ± 0.0024 MeV.

3.6 Experimental method

The purpose of this work is to study the response of the Ge detector to ionizing radiation by comparing pulse heights produced by light energetic particles (p, ^{3,4}He, ^{7}Li) with those produced by monoenergetic γ−rays. An earlier measurement for particle energies below 10 MeV was based on separate

measurements for γ-rays and particles, wherein the "window effect" and nuclear energy loss of the particles could introduce more uncertainty in the results and make the comparison more difficult. The novelty of the method used here is that a direct comparison of the detector's response to energetic particles and γ-rays was made via simultaneously measured particle-γ mixed spectra accompanied by a series of reference pulses, where the characteristic γ lines (peaks) in the spectra provided an instant calibration of the test pulses. Based on the γ calibration, the energy* peak of the incident monoenergetic particles in the test pulse height units could be converted to the standard energy units, *i.e.*

$$E_1(ion) = N_{e\text{-}h}\varepsilon_0 \tag{3.7}$$

where $N_{e\text{-}h}$ is the number of electron-hole pairs created by the incident particles in the active volume of the Ge detector. On other hand, the energy* of the incident particles was derived from knowing the energy loss of the incident particles in the window of the detector and the contribution of non-ionizing energy loss due to nuclear collisions, *i.e.*

$$E_2(ion) = E_0 - \Delta E_w - \Delta E_n = N_{e\text{-}h}\varepsilon_{ion} \tag{3.8}$$

where E_0 is the energy of the incident particles before entering the detector. By taking the ratio of Equation 3.8 and Equation 3.7, a value for $\varepsilon_{ion}/\varepsilon_0$ can be obtained, which will demonstrate the behaviour of the Ge detector to energetic particles (*i.e.* a few MeV) relative to its response to γ-rays.

---

*The energy refers to the energy dissipated by the incident particles in the active volume of the Ge detector.

To summarize, the energy loss of the incident particles in the front window of the Ge detector and part of the nuclear energy loss during the stopping process of the particles in the active volume of the Ge detector do not contribute to the production of electron-hole pairs, which are two crucial and dominant corrections for calculating the deposited energy of the incident particles in this study.

References

1. A. Nukermans and G. S. Kino, Phys. Rev. B7 (1973) 2693.
2. L. Reggiani, C. Canali, F. Nava and G. Ottaviani, Phys. Rev. B16 (1977) 2781.
3. A. Rytz, H. H. Staub, H, Winkler and F. Zamboni, Nucl. Phys. 43 (1963) 229.
4. F. S. Goulding and D. A. Landis, "Semiconductor Detectors", Section IIIA in Nuclear Spectroscopy and Reactions, J. Cerny, ed. Academic Press (1974).
5. H. R. Bilger, Phys. Rev. 163 (1967) 238.
6. F. S. Goulding and D. A. Landis, IEEE Trans. Nucl. Sci. NS-35 (1988) 119.
7. R. D. Ryan, IEEE Trans. Nucl. Sci. NS-20 (1973) 473.
8. W. K. Chu, J. W. Mayer and M. A. Nicolet, "Backscattering Spectroscopy", Academic Press, New York, 1978.
9. J. L'Ecuyer, J. A. Davies and N. Matsunami, Nucl. Instr. and Meth. 160 (1979) 337.
10. S. Y. Tong, W. N. Lennard, P. F. A. Alkemade and I. V. Mitchell, Nucl. Instr. and Meth. B45 (1990) 30.
11. J. B. Marion, Reviews of Modern Physics 38 (1966) 323.
12. J. A. Leavitt, L. C. McIntyre, Jr., P. Stoss, J. G. Oder, M. D. Ashbaugh, B. Dezfouly-Arjomandy, Z. M. Yang and Z. Lin, Nucl. Instr. and Meth. B40/41 (1989) 776.

Chapter 4

NUCLEAR ENERGY LOSS

The response of semiconductor detectors to energetic particles depends on the interaction of the particles with the detector material. Except for the ionization effect, which is responsible for the production of the charge carriers, there are also other non-ionizing competing processes, in which some of the energy of the particles is expended in displacing the lattice atoms or generating defects, or transferred to lattice vibrations.

4.1 Stopping power of charged particles in solid media

The interaction of energetic particles with a solid medium (target) arises from the Coulomb interaction via inelastic collisions with the electrons and elastic collisions with the nucleus in the medium. The charge state of the projectile is known to be important in such Coulomb interactions. At high velocity, the electrons of the incident particle will be fully stripped, and partially stripped at low velocity. The stopping power is used to describe the rate of energy loss of the projectile in the target. The total stopping power can be conveniently divided into two separate parts: (1) the electronic stopping power (S_e) due to the energy transferred to the target electrons; and (2) the nuclear stopping power (S_n) due to the energy transferred to the target nuclei. Possible correlations between the two processes are usually ignored [1].

The electronic and nuclear stopping cannot be measured separately.

Generally, the electronic stopping power for heavy ions is scaled to that of protons and helium, where the latter have been derived from measurements. The electronic stopping can be described by the Bethe formula [2] at high energy

$$S_e = \frac{4\pi e^4 (Z_1^*)^2 Z_2}{m_0 v^2}\left(\ln\left(\frac{2m_0 v^2}{\langle I\rangle}\right) - \beta^2 - \ln(1-\beta^2) - \frac{C}{Z_2}\right) \qquad (4.1)$$

where e and m_0 are the charge and mass of an electron, Z_1^* and v are the effective charge and relativistic velocity of the incident ion, Z_2 is the target atomic number, C is from the **shell effects**, <I> is the mean target ionization potential and β=v/c. At low velocity, the electronic stopping is proportional to v^n, where n ~ 1. Nuclear collisions are simply treated as the elastic scattering of two heavy nuclei, which can be described classically by screened Coulomb scattering. The nuclear stopping can be calculated by using appropriate interatomic potentials. From the conservation of energy and momentum, the energy of the projectile transferred to the target atom for each collision is

$$T(E,p) = \frac{4M_1M_2}{(M_1+M_2)^2} E\sin^2\frac{\Theta(p)}{2} = T_m \sin^2\frac{\Theta(p)}{2} \qquad (4.2)$$

where M_1 and M_2 are the masses of the projectile (Z_1) and the target atom (Z_2), respectively, and p is the impact parameter; $T_m = 4M_1M_2E/(M_1+M_2)^2$ and Θ is the projectile scattering angle in the centre-of-mass coordinate system. The nuclear stopping power, $S_n(E)$, is the average nuclear energy loss rate obtained by integration

over all impact parameters

$$S_n(E) = \int_0^{T_m} T d\sigma(T,E) = \int_0^{p_{max}} T(E,p)\, 2\pi p dp \tag{4.3}$$

By using the universal interatomic potential [1], the nuclear stopping power (eV·cm²/atom) can be expressed

$$S_n(E) = \frac{8.462\times10^{-15} Z_1 Z_2 M_1 S_n(\epsilon)}{(M_1+M_2)\,(Z_1^{.23}+Z_2^{.23})} \tag{4.4}$$

where $S_n(\epsilon)$ is the reduced nuclear stopping

$$S_n(\epsilon) = \frac{\ln(1+1.1383\epsilon)}{2(\epsilon+0.01321\epsilon^{.21226}+0.195993\epsilon^{.5})} \qquad for\ \epsilon\le 30 \tag{4.5}$$

$$S_n(\epsilon) = \frac{\ln(\epsilon)}{2\epsilon} \qquad for\ \epsilon>30 \tag{4.6}$$

and ϵ is the (dimensionless) reduced energy defined as

$$\epsilon = \frac{a_u M_2}{Z_1 Z_2 e^2 (M_1+M_2)} = \frac{32.53 M_2 E}{Z_1 Z_2 (M_1+M_2)\,(Z_1^{.23}+Z_2^{.23})} \tag{4.7}$$

where E is in keV, M_1 and M_2 are in amu, and a_u is the universal screening length. The probability of a nuclear collision occurring can also be roughly estimated using the Rutherford scattering cross section, *i.e.* proportional to $(Z_1Z_2/E)^2$. The probability increases rapidly with decreasing energy. Nuclear stopping dominates at low projectile energies, reaching a maximum close to $\epsilon=1$ and then decreasing as $E \to 0$.

4.2 Nuclear (non-ionizing) energy loss

Considering the process of ionization by incident energetic particles in the

depleted volume of semiconductor detectors, the electronic collisions (responsible for projectile stopping) mainly lead to electron−hole pair production. When a particle approaches the end of its range, nuclear collisions play a major role in the energy loss process, wherein the energy of the projectiles is transferred to target atoms by atomic scattering, given by Eq. 4.2. The scattered target atoms (*i.e.* recoils) will undergo a similar process as they slow down. The probability for those recoiling target atoms to create further ionization is quite small for the case of light incident ions. A large portion of the transferred energy does not lead to the production of electron−hole pairs in detectors. Therefore, the energy of an incident particle inferred only from the number of electron−hole pairs in the detector has to be corrected by the non-ionizing part of the nuclear energy loss, which is one of the factors responsible for the pulse height defect.

As an approximation, the non-ionizing part of the nuclear energy loss for light ions in the Ge detector can be estimated by

$$\Delta E_n = \int_0^{E_0} dE_n = \int_0^R S_n dx = N \int_0^{E_0} \frac{S_n}{S_n + S_e} dE \qquad (4.8)$$

where R is the range of the incident particles in the detector material having an atom density, N. The total stopping values are derived from the empirical stopping formula in refs. [3] and [4]. The neglect of the ionizing effect caused by the scattered target atoms causes an overestimate of the correction for the non-ionizing nuclear energy loss.

A second order correction can be made by considering the energy loss of a primary recoil target atom through secondary recoils, *i.e.* the nuclear energy loss of

Ge atoms in Ge crystal. Assume that the energy of the primary Ge recoil is T, the portion of T transferred by further nuclear collisions can be calculated [5] by

$$Q(T) = \frac{1}{T}\int_0^T \frac{S_n(E)}{S_e(E) + S_n(E)}\, dE \tag{4.9}$$

Then Equation 4.8 can be modified to

$$E_n = \int_0^{E_0} \frac{1}{S(E)} \int_0^{T_m(E)} Q(T)\, T d\sigma(T, E)\ dE \tag{4.10}$$

For the case of Rutherford scattering

$$\tan^2 \frac{\Theta}{2} = \frac{Z_1 Z_2 e^2 (M_1 + M_2)}{2EPM_1} \tag{4.11}$$

by using Equation 4.2 the cross section can be simplified as

$$d\sigma = 2\pi p dp = (\pi a_u^2/4)\ (dt/t^2) \tag{4.12}$$

where $$t = \epsilon^2 T / T_m(E) \tag{4.13}$$

According to Lindhard's previous contribution [6], the scattering cross section can be expressed in a simple form [1]

$$d\sigma = (\pi a_u^2/2)\, f(t^{1/2})\, dt/t^{3/2} \tag{4.14}$$

where the function $f(t^{1/2})$ was determined numerically using the Thomas–Fermi potential, *i.e.* Equation 4.3. By introducing a dimensionless range $\rho = Rk_R = RN\pi a_u^2 \gamma$, Equation 4.10 becomes

$$E_n = \frac{1}{2} N\pi a_u^2 \gamma k_E k_R \int_0^{\epsilon_0} \left(\epsilon \cdot \frac{d\epsilon}{d\rho}\right)^{-1} \int_0^{\epsilon^2} Q(t)\, f(t^{1/2})\, t^{-1/2} dt\, d\epsilon \tag{4.15}$$

with $k_E = E/\epsilon$ and $\gamma = 4M_1M_2/(M_1+M_2)^2$. The numerical value of $f(t^{1/2})$ is taken

from ref. 1 for this integration. The results should give a good estimate of the non-ionizing nuclear energy loss, since the second order correction represents $\leq 10\%$ of the nuclear energy loss calculated by Equation 4.8. As a cross check, the non-ionizing nuclear energy losses were calculated by the TRIM Monte Carlo program [1]. All the data for ^{1}H and ^{4}He in Ge are shown in Figures 4.1. The other nuclear energy loss data used are 25.2 keV for 3.76 MeV ^{7}Li and 7.2 keV for 2.48 MeV ^{3}He in Ge. The values obtained by TRIM agree well with those from Equation 4.15. Unfortunately, there are no accurate experimental data available for comparison with the calculations. The experimental results of nuclear energy loss for heavy ions in silicon were usually obtained from the energy difference between nonchanneled and channeled ions in silicon detectors [7]. But they are more or less subjected to the improper correction of the detector window energy loss for channeled and nonchanneled ions. The nuclear energy loss mentioned in later chapters refers to the non-ionizing nuclear energy loss calculated by Equation 4.15 or from the TRIM program.

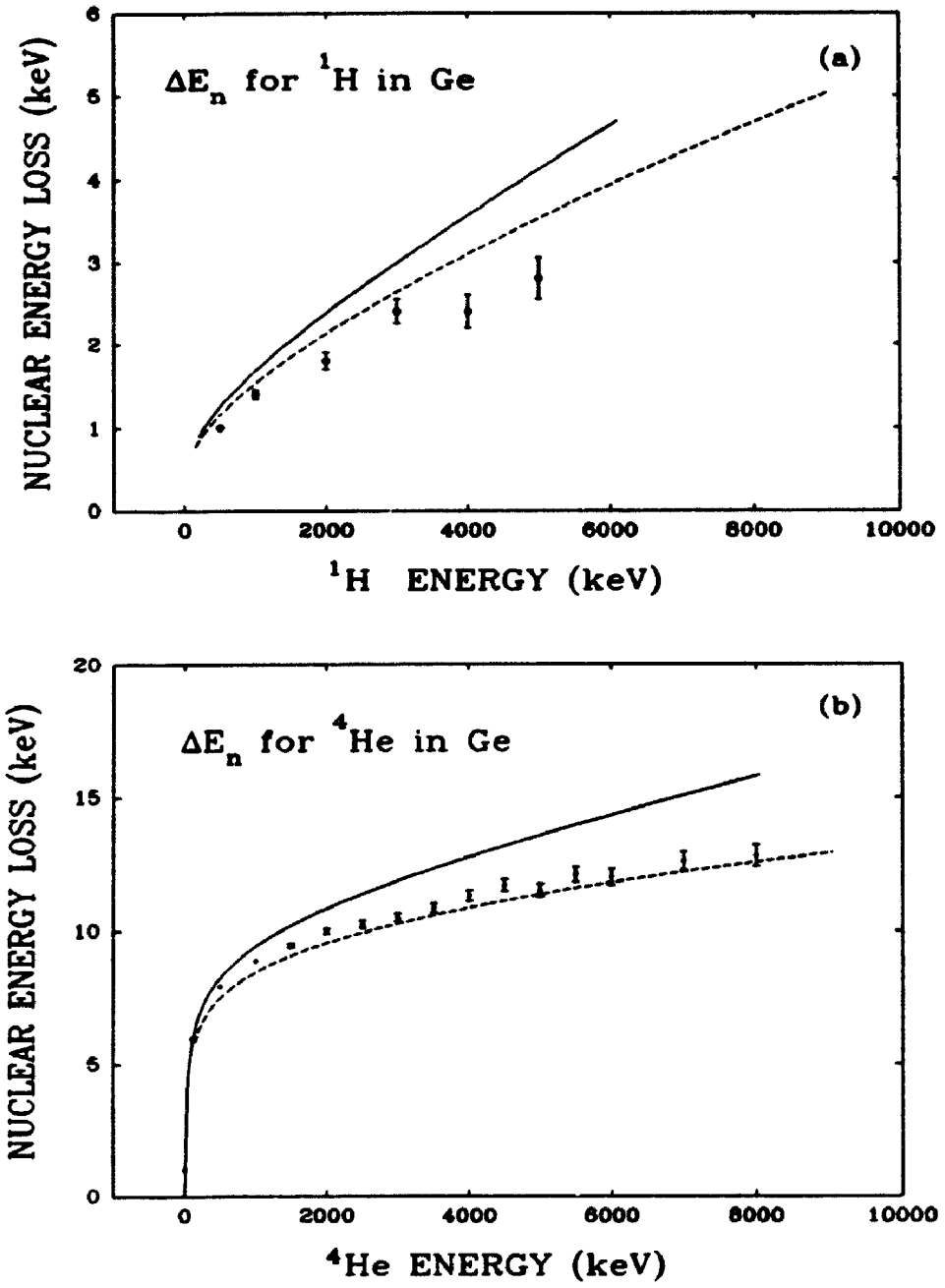

Figure 4.1 The nuclear energy loss, ΔE_n, is calculated using: (1) Equation 4.8 (solid line); (2) Equation 4.15, which includes the recoil ionization effect (dashed line); (3) TRIM calculation with 5000 incident ions (circles).

References

1. J. F. Ziegler, J. P. Biersack and U. Littmark, "The Stopping and Range of Ions in Solids", Vol.1, Pergamon Press, 1985.
2. H. A. Bethe and W. Heitler, Proc. Roy. Soc. A146 (1934) 83.
3. J. F. Ziegler, "Hydrogen: Stopping Power and Ranges in All Elements", Vol. 3, Pergamon Press, 1977.
4. J. F. Ziegler, "Helium: Stopping Powers and Ranges in All Elements", Vol. 4, Pergamon Press, 1977.
5. E. L. Haines and A. B. Whitehead, Rev. Sci. Instr. 37 (1966) 2.
6. J. Lindhard, V. Nielsen and M. Scharff, Mat. Fys. Medd. Dan. Vid. Selsk. 33, No. 10 (1968).
7. A. Grob, J. J. Grob and P. Siffert, Nucl. Instr. Meth. 132 (1976) 273

Chapter 5

MEASUREMENTS OF THE EFFECTIVE WINDOW THICKNESS OF THE Ge DETECTOR

The window of a planar semiconductor detector usually refers to its front and/or back conducting layer. It is the layer through which the incident particles must penetrate to reach the active (*i.e.* depletion) volume of the detector. Although the ionization effect in such layers is also caused by the penetrating particle, the lifetime of the created electron-hole pairs is too short to enable such charge carriers to be collected. Therefore, the energy loss of the incident particles in the window layer will not contribute to the total production of electron-hole pairs created by the incident particles in the detector, *i.e.* the effective incident energy of the particles is less than the original energy by the amount of the window energy loss. If one assumes that the window comprises simply a thin layer of material, the energy loss of the energetic particles in the window should approximately follow the stopping power curve, *i.e.* the energy loss increases with increasing energy of the incident particles and decreases after reaching the energy corresponding to the maximum in the stopping power, *e.g.* see ref. 1. Although a thin window is desired for *particle* detection, there always exists a certain limitation due to either technical difficulties or the nature of the materials. For surface barrier semiconductor detectors, a strong electric field in the detector can penetrate into the window region to make the apparent window thickness smaller [2] - an effect which depends on the type of the interface layer between the window and the underlying bulk detector crystal. The

equivalent thickness of the window layer can be estimated by measuring the window energy loss for an incident charged particle and dividing by the appropriate stopping power.

5.1 Window structure of the Ge detector

According to the manufacturer's (EG&G Ortec) description, the window of the Ge detector was formed by implanting 40 keV boron ions into the surface of the Ge detector crystal at a total fluence of 10^{14} ions/cm^2, which can produce a ~0.1-0.15 μm thick boron implanted layer at the surface of the Ge crystal (see ref. 4). As an approximation, the implantation damage can be estimated from the density of displaced lattice atoms [3]:

$$N_d = Q\frac{E_n}{2E_dR_p} = QS_n\frac{1}{2E_d} \qquad (5.1)$$

where E_n is the energy deposited in nuclear collisions by the incident ions and secondary recoils, E_d is the displacement energy of the lattice atoms, R_p is the range of the incident ions, and Q is the areal density of implanted ions. Choosing the values E_d=15 eV and S_n= 5.65 × 10^8 eV/cm [4] for ^{11}B in Ge, the damage is calculated to be $N_d \approx 1.9 \times 10^{21}$/cm^3, which implies that only ~4.3% of the lattice Ge atoms would be displaced for an implantation dose of 10^{14} /cm^2 (the atom density for Ge is 4.43 × 10^{22} atoms/cm^3). It is believed that this calculation is only valid for room temperature implantation where a significant annealing occurs, since more damage will occur at a lower temperature. For example, the normalized disorder due to implantation increases to 100% as the temperature of the Ge substrate drops to

LN_2 temperature for such an implantation dose [5]. Studies have shown that room temperature is the preferred temperature for implantation to create a good conducting layer in Ge [6,7], without any necessity of higher temperature annealing. Assume that the implantation for the Ge detector was done at room temperature. Therefore, the implantation dose was below that value necessary to render the surface layer amorphous, *i.e.* the window layer retains some semblance of crystalline structure [6]. However, the implantation could certainly provide a boron (or charge carrier) peak concentration of $10^{18}/cm^3$ in the window layer, which is enough to make the surface of the Ge crystal into a conducting layer [7,8]. Unlike the surface barrier semiconductor detector, the window thickness of the Ge detector depends on the boron distribution in the surface layer. Figure 5.1 shows a Monte Carlo [4] simulation of the boron distribution in amorphous Ge based on LSS theory [9]. Although the projected range of the boron ions is ~0.10 μm, the conducting layer extends at least to a depth of 0.175 μm and certainly differs from the ideal uniform distribution (see dashed rectangle distribution in Figure 5.1a). Figure 5.1b shows the distribution of vacancies due to the implantation, where the peak occurs near 650 Å and the average damage is quite close to the above estimate. The actual distribution of boron in the Ge detector used here is difficult to estimate without knowing the details of the Ge crystal direction and the implantation parameters (*e.g.* temperature). But unlike other elements, the unique characteristic for boron implantation is that it can create a quite uniform boron distribution in Ge [7,10]. As the depletion region extends to the interface between the window and the bulk of the Ge detector at 400V, corresponding to total depletion, the window layer is expected to remain

constant with a further increase in the bias [11].

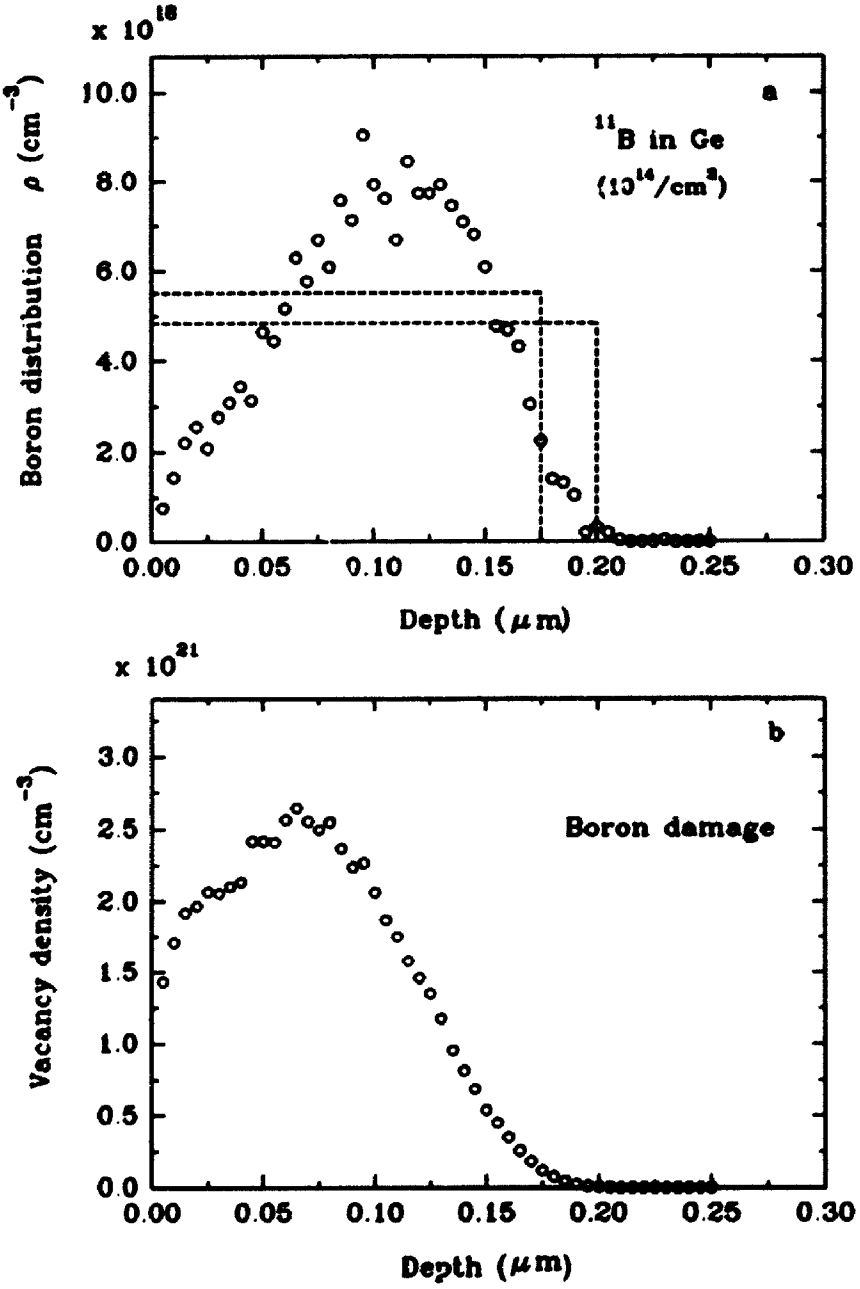

Figure 5.1 TRIM calculation of (a) the boron distribution and (b) the vacancy distribution in the 40 keV boron implanted amorphous Ge material.

5.2 Measurements of the energy loss in the window of the Ge detector

There are basically three ways to estimate the window thickness of semiconductor detectors, *i.e.* Bohr straggling method, absorption edge technique, and the detector tilting method.

As mentioned in Chapter 2, Bohr straggling [12] in the window layer will contribute to the total FWHM of the energy peak for monoenergetic incident ions,

$$(2.35\Omega)^2 = (FWHM)^2_{total} - (FWHM)^2_e \qquad (5.2)$$

where $(FWHM)_e$ is the contribution from the electronic noise, which can be measured using the FWHM of the test pulses. Using the Bohr straggling equation, *i.e.* Equation 2.10, the window thickness can be derived. It has been found that the measured straggling is less than Bohr straggling [12]. But even after such a difference has been considered, the calculated window thickness seems to be always larger than the actual values and sometimes the change of the Bohr straggling in the detector window does not reflect the changes of the window thickness (see the later discussion in this chapter).

The absorption edge technique is a complicated method, which relies on the variation of the detector efficiency for X−rays with an energy near the absorption edge of the detector window material [13]. As the energy of the incident X−ray increases further above the absorption edge (*e.g.* K or L edge), the energy of the corresponding photoelectrons in the window layer also increases. Therefore, the detected yield will change as soon as some of the photoelectrons start penetrating through the window layer into the active volume of the detector. By measuring such small changes in the X−ray yield, the window thickness of the detector can be

estimated. The uncertainties of the published data are usually ~15−20%.

The detector tilting method is the most effective and accurate way to obtain the effective window thickness of the detector, which is suitable for this experiment. It relies on measuring the variation of the pulse height of the incident monoenergetic ions with the tilt angle of the detector with respect to the incident beam direction, see Figure 5.2. Since the implanted boron atomic density is only ~0.01% of the Ge atomic density in the window layer, the window energy loss is dominated by the stopping power of the incident particles in Ge. If there is no directional dependence

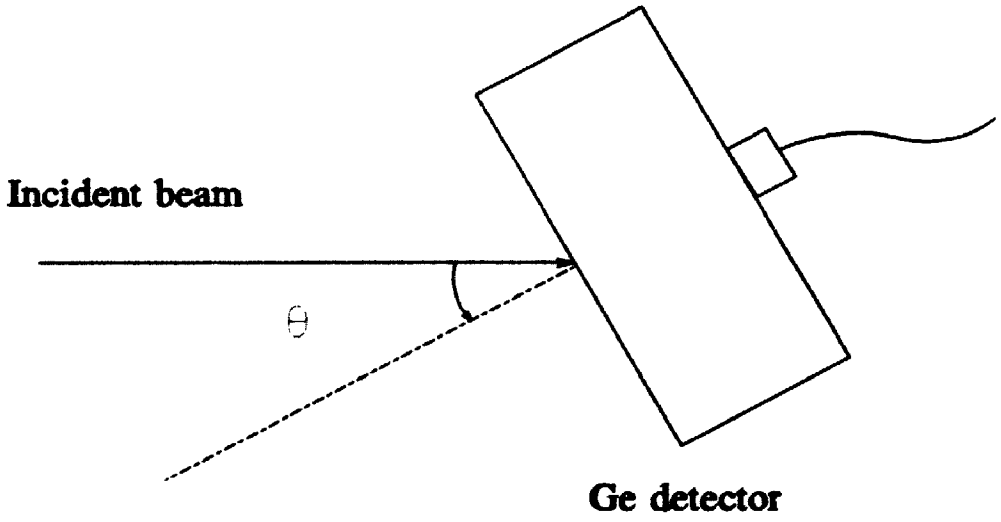

Figure 5.2 Relative position of the Ge detector with respect to the incident beam direction in the detector tilting method. The rotation axis of the detector is perpendicular to the paper through the front surface of the detector.

of the energy loss rate of the window layer of the Ge detector (*e.g.* crystalline effects), the output pulse height of the Ge detector for monoenergetic incident particles should depend on the tilt angle, θ_{det}, in the following manner:

$$P = P_0 - P_1 \sec(\theta_{det}) \tag{5.3}$$

where the pulse heights P, P_0, P_1 are measured values in test pulse height units (P.H.U.). By fitting Equation 5.3 to the output pulse height data for different θ_{det}-values of the Ge detector, the parameters P_0 and P_1 can be determined. The value of P_1 corresponds to the window energy loss, the value of P_0-P_1 is equal to the pulse height of the incident particles for $\theta_{det}=0°$, and P_0 corresponds to the pulse height of the incident particles for zero window thickness of the Ge detector. Thus, the window energy loss of the incident particles can be calculated by substituting P_1 for P_h in Equation 3.2 or by

$$\Delta E_w = \frac{P_1}{P_0}(E_0 - \Delta E) \tag{5.4}$$

where E_0 is the incident energy of the particles, and ΔE is any non-ionizing energy loss of the incident particles, such as the nuclear energy loss (ΔE_n) and/or the energy loss of emitted α's due to a finite source thickness (ΔE_s), excluding the window energy loss. The ΔE_w values from the two methods above agree very well, within $\lesssim$ 1%.

5.2.1 Preliminary measurement of the window

The first attempt was to use a triple α emitting source ($E_\alpha(^{239}Pu)$= 5156.6 keV, $E_\alpha(^{241}Am)$= 5485.6 keV, and $E_\alpha(^{244}Cm)$= 5804.82 keV [14]) for determining the

window energy loss of the Ge detector. The bias of the Ge detector was 1000V. Figure 5.3 shows a typical $\alpha-\gamma$ mixed spectrum containing three $\alpha-$peaks in the high energy part (see Figure 5.3a) and ^{152}Eu $\gamma-$ray peaks in the low energy part (see Figure 5.3b). The positions of the ^{241}Am and ^{244}Cm α_0 peaks in the spectra were determined by fitting a Gaussian function with a low energy exponential tail. The peak position for the ^{239}Pu α_0 was obtained by fitting two such functions (corresponding to α_0 and α_1 having a separation of 12.8 keV and a relative intensity ratio α_1/α_0 = 0.206), since the resolution (14.7 keV) of the Ge detector could not totally resolve the two ^{239}Pu α peaks (5156.6 and 5143.8 keV) [14]. The results for the measured pulse height data as a function of θ_{det} are shown in Figure 5.4, where the smooth fitted curve is located within the uncertainties of the data. The window energy losses determined by Equation 3.2 and Equation 5.3 were 108.1±2.2 keV for ^{239}Pu, 102.1 ± 1.5 keV for ^{241}Am and 98.9 ± 2.0 keV for ^{244}Cm at 80K. Surprisingly, the window thicknesses (derived from stopping power values [9]) are 0.502 ± 0.010 μm for ^{239}Pu, 0.495 ± 0.010 μm for ^{241}Am and 0.491 ± 0.010 μm for ^{244}Cm, (equivalent Ge thickness at 80K), which are much larger than the thickness claimed by Ortec and predicted by the TRIM calculation. For the α source, similarly, the equivalent source thickness was measured by tilting the source with respect to a fixed silicon detector for each α group, yielding ΔE_s = 3.8 keV ± 1.9 keV.

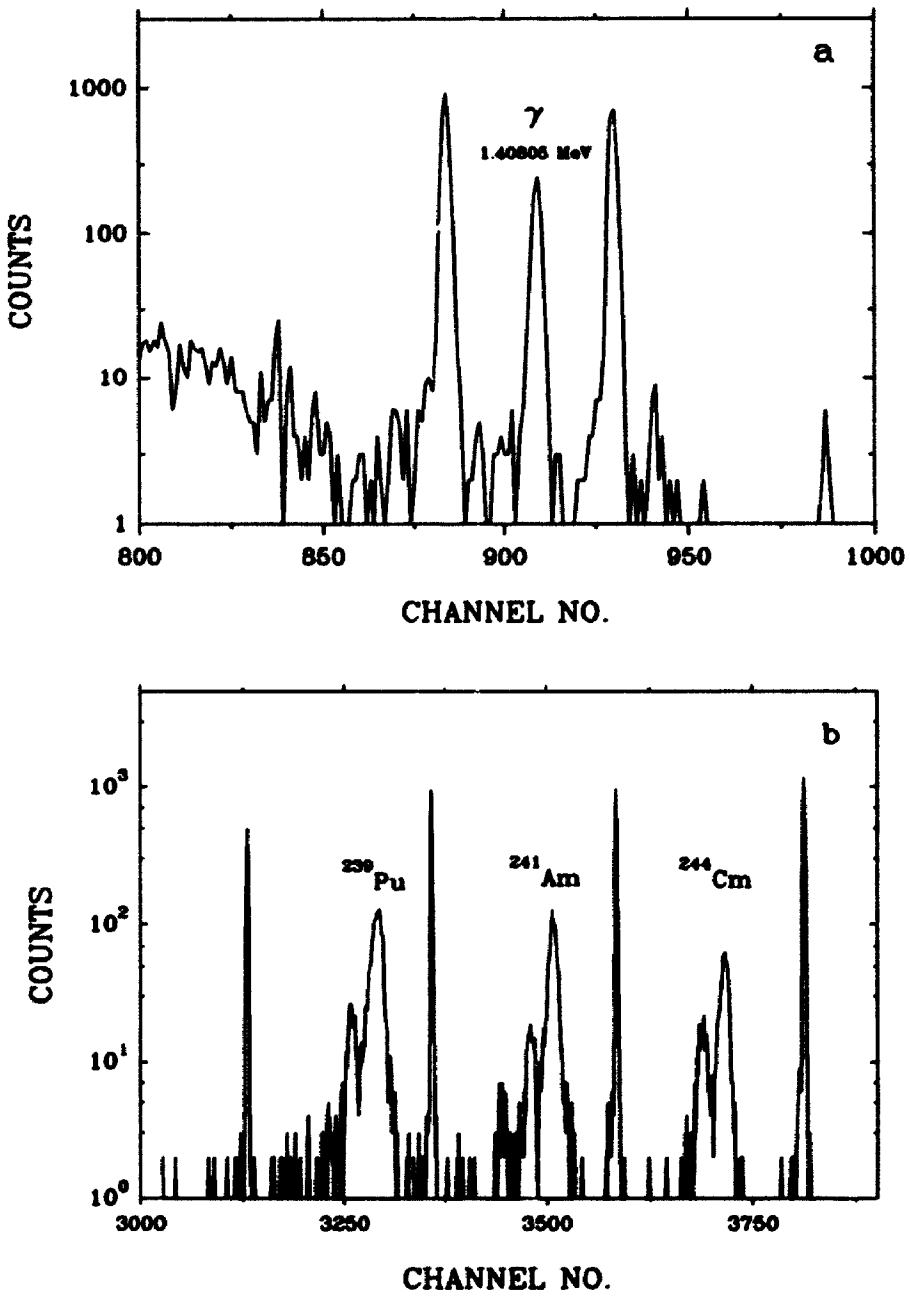

Figure 5.3 Typical spectrum observed for the triple α−source with a ^{152}Eu γ−emitting source. (a) γ peak, together with two reference test pulse peaks in the low energy portion of the spectrum; (b) α peaks with the reference peaks in the high energy portion of the spectrum.

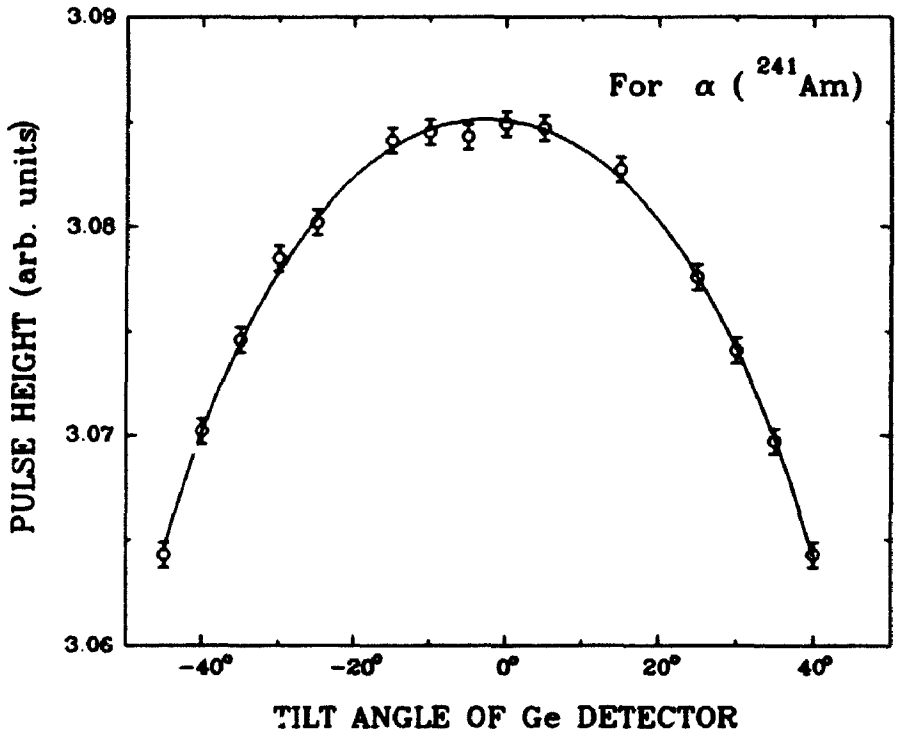

Figure 5.4 Pulse height data (α ^{241}Am, 5485.6 keV) as a function of the detector tilting angle to find the effective window thickness of the Ge detector and the surface normal. The smooth curve is a fit: $P = P_0 - P_1 \sec(\theta - \theta_0)$.

In a continuing effort to measure the window thickness of the Ge detector for different charged particles at different energies, accelerated proton ($^1H^+$) and α ($^4He^+$) beams were used. Since the C/Au self-supporting foil ($\rho t_C = 11.2$ $\mu g/cm^2$ and $\rho t_{Au} = 9.6$ $\mu g/cm^2$) was used for α particles, the incident ions can be scattered from both C atoms and Au atoms. The energy of the scattered ions is determined by the (energy independent) kinematic factor:

$$k = \frac{E_1}{E_0} = \left(\frac{(M_2^2 - M_1^2 \sin^2\theta)^2 + M_1 \cos\theta}{M_1 + M_2} \right)^2 \qquad (5.5)$$

where M_1 is the mass of the incident ion, M_2 is the mass of the scattering (target) atom, θ is the scattering angle of the incident ion with respect to the direction of the incident beam, and E_0 (E_1) is the energy of the incident (scattered) ions. Specifically, $k_{\alpha\rightarrow C}=0.96044$ and $k_{\alpha\rightarrow Au}=0.99755$ at $\theta=20^\circ$. The energy of the α particles scattered to 20° from the Au atoms and arriving at the Ge detector can be calculated by

$$E=k\left(E_0-S(C)N_C-\frac{1}{2}S(Au)N_{Au}\right)-\frac{1}{2}S'(Au)N_{Au}sec20^\circ \qquad (5.6)$$

where S(C) is the mean stopping power of α's in the (upstream) C layer of the scattering foil, S(Au) and S´(Au) are the mean stopping powers in the (downstream) Au layer of the scattering foil before and after scattering, respectively. The energy of the α particles scattered from the C atoms can be calculated in a similar fashion. The intensity of the α particles scattered from Au relative to that from C atoms is equal to the ratio of the two scattering cross sections weighted by the relevant atomic areal densities, *i.e.* approximately $(Z_{Au}N_{Au}/Z_CN_C)^2=(79\times9.6/67.2)^2\approx173.4$ based on the corresponding Rutherford scattering cross sections. However, as for $^{12}C(\alpha,\alpha)^{12}C$ backscattering (see chapter 3), non-Rutherford behaviour may occur for the $\alpha-^{12}C$ forward scattering cross section, especially in the energy region near 4.265 MeV where the measured cross section for the $^{12}C(\alpha,\alpha)^{12}C$ backscattering exceeds the Rutherford value by a factor ~130. At the incident energies chosen, the scattering yield from Au atoms always dominated the spectrum and those peaks were selected for the measurements. For protons, only the self-supporting Au foil was used, since the Au and C scattering peaks cannot be separated using the thin Au/C foil and the energy loss of protons is still quite small even in a slightly thicker Au foil. The energy

of the protons scattered from the Au foil was calculated by substituting $\rho t_C=0$ in Equation 5.6.

Typical spectra for incident protons and α's can be found in Figure 5.5a−b. Using again the detector tilt method as was used for measurements with α sources, the window thickness was measured for ^{1}H and ^{4}He at energies varying between 500 keV and a few MeV. The pulse height data show a large discrepancy from the behaviour predicted by Equation 5.2 at several θ_{det}-values, particularly for tilting angles in the range $-10° < \theta_{det} < 10°$, even though the results were reproducible. Therefore it was found that based on the pulse height measurements at a few selected angles, the window thickness of the detector (in keV) could not be determined with an accuracy <10% for H and <5% for ^{4}He and also varied with the choice of measuring angles. These variations will greatly affect the comparison of the ionization energy for γ−rays and particles. Furthermore, for several particular tilting angles of the detector, the measured α peaks showed a large high energy shoulder which did not appear for the proton peaks at the same angles, see Figure 5.6.

In order to investigate the details, two further measurements were made for 1.5 MeV ^{4}He and 1.2 MeV protons as follows:

(1) The pulse heights of the scattered protons and α particles were measured for detector tilt angles from −47° to 45° in 1° increments (normal incidence corresponds to an incident angle θ_{det} ~−2.5°); the positions of the α peaks with a high−energy shoulder were determined by fitting a Gaussian function with a low energy exponential tail to the main part of the α peaks, excluding the high energy shoulder; the results surprisingly revealed structure on the

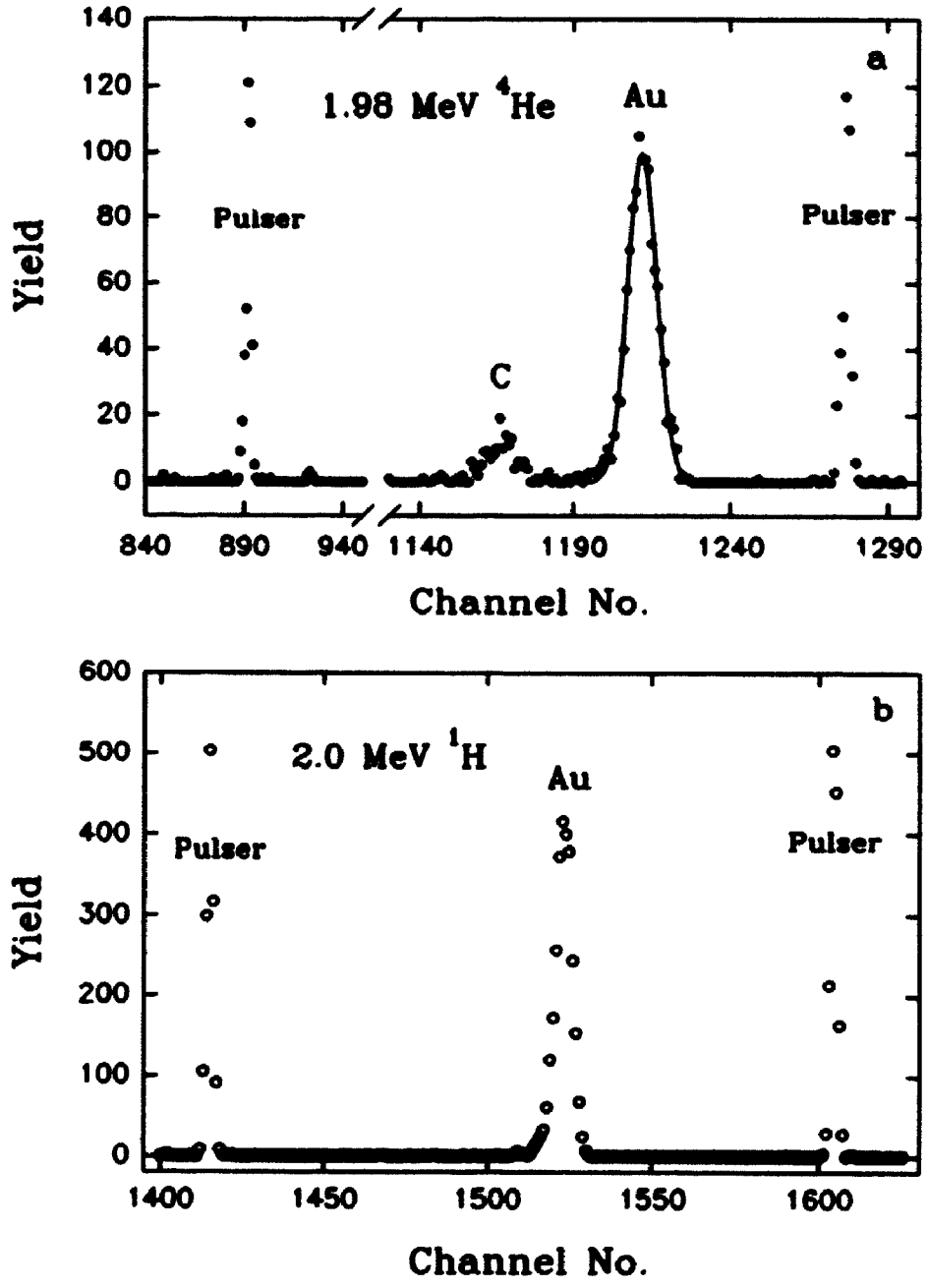

Figure 5.5 Typical spectra observed using ion beams. (a) 1.981 MeV ^{4}He peaks scattered from the self–supporting Au/C foil, together with two reference test pulse peaks, and the smooth curve is a fit using a Gaussian function with a low energy exponential tail; (b) 2.0 MeV ^{1}H peaks scattered from the self–supporting Au foil, with reference test pulses.

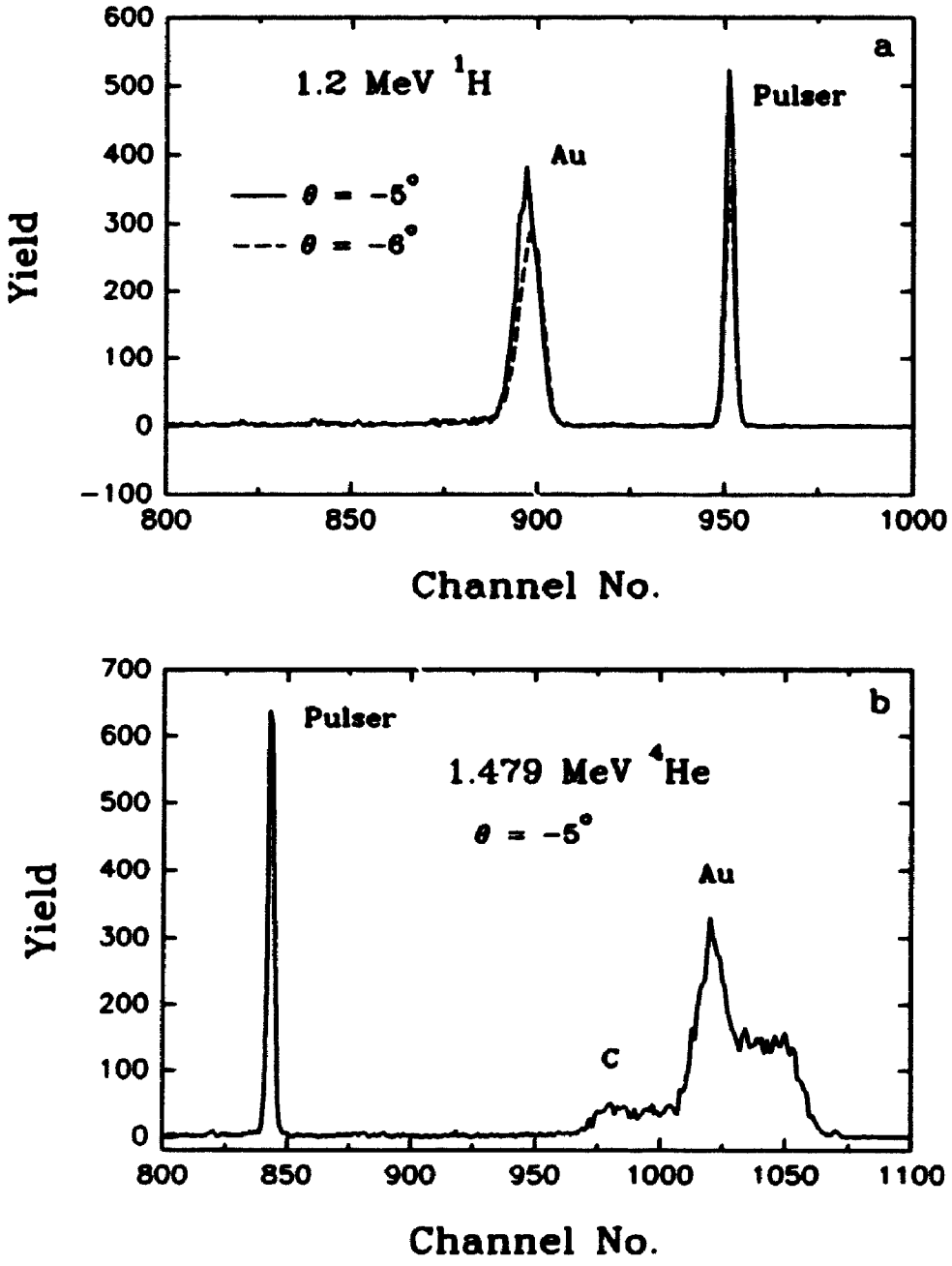

Figure 5.6 Examples of spectra for ^{1}H and ^{4}He beam near the anomalous tilting angles. (a) ^{1}H peak only shows a small shift at $\theta = -6°$ relative to that at $\theta = -5°$; (b) ^{4}He peaks show high energy shoulders, see Figure 5.17 as a reference.

tilting pulse height data wherein the measured pulse heights at some angles were higher or lower than the expected values, see Figure 5.7. Unfortunately this behaviour also occurred at the detector angles which had been chosen earlier, which explained why the window thickness could not be determined accurately if measurements were made only at a few selected angles, such as 0°, ±5°, ±10°, ...

(2) The pulse heights were measured in detail using small angular steps around those detector angles where anomalous structure had been observed; the angular dependence of these data suggested the existence of channeling effects in the Ge detector; a detailed study of such a channeling effect will be discussed in the next section.

In Figure 5.7, most of the pulse height data follow the curve shape defined by Equation 5.3. For convenience, the data showing peaks with higher energy shoulders for α particles and bigger or smaller pulse height values with relatively poor resolution for protons were called anomalous data here. These data were excluded in the process of determining the fitting parameters for the window thickness. There is no prescription that defines how to reasonably determine the positions of those anomalous pulse height peaks with high energy shoulders or to identify them as random pulse height peaks. The stopping power of the ions in those directions is different from the random value so that changes in the pulse height do not truly represent the random energy loss in the window layer. However, even with the inclusion of these anomalous data, the window thickness could still be determined with ±1% agreement with that from the data excluding the anomalous data. In Figure 5.7, the solid and dashed lines represent the fitted curves including and

excluding the anomalous data, respectively. The window energy loss was finally determined within ±2% for α's and ±3-6% for protons.

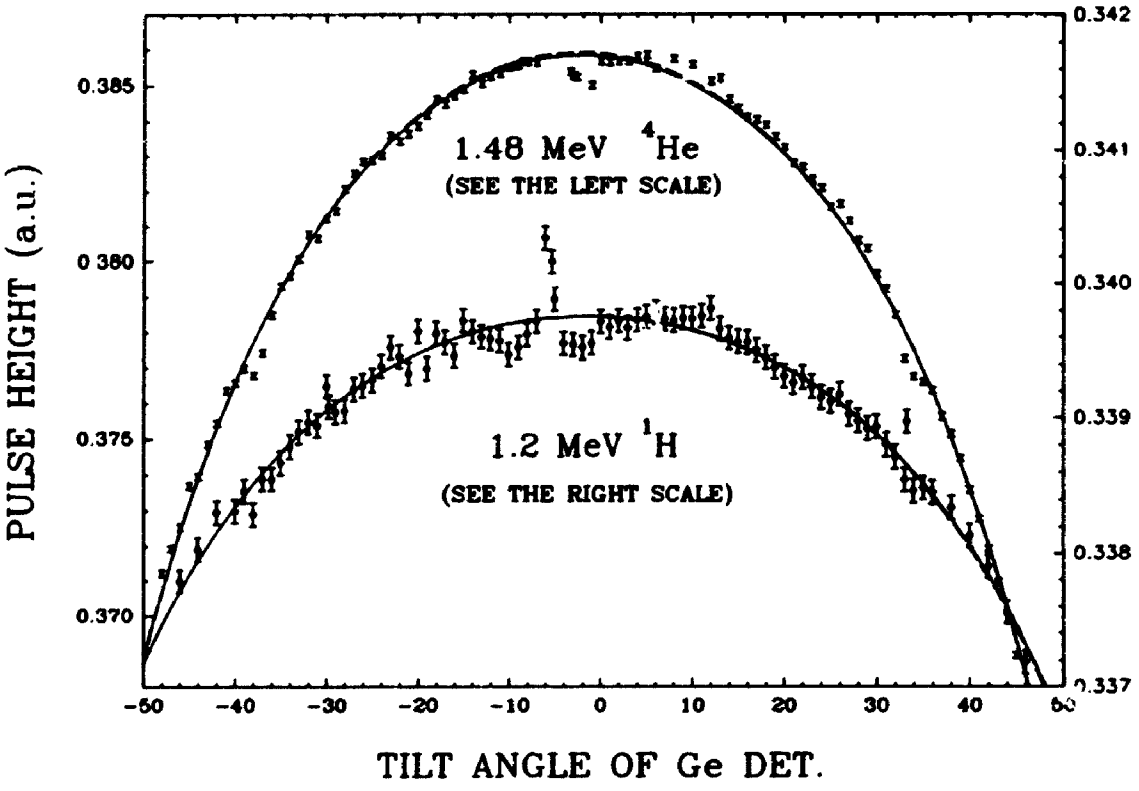

Figure 5.7 Pulse height data as a function of the detector tilting angles for 1.197 MeV ^{1}H and 1.479 MeV ^{4}He beams. The dashed curves (overlapped with the solid curves) is the fit of $P = P_0 - P_1 \sec(\theta - \theta_0)$ to all the data for each group data. The solid curves are the fits only to the data excluding those data at the anomalous angles.

5.2.2 Energy and temperature dependence

The dependence of the apparent Ge detector window thickness on incident energy was measured at 80K for protons with energies in the range 0.5−3 MeV and

for ^{4}He with energies in the range 1−4.5 MeV, Figures 5.9 and 5.8, respectively. The window thicknesses obtained using a ^{4}He beam and α sources were quite consistent, showing a maximum value at 2.2 MeV but not following the widely accepted energy dependent stopping (^{4}He in Ge) power curve for α particles. This observation suggests that the energy loss of α particles in the thin window layer is not simply proportional to the mean stopping power of α particles in the window layer, which is difficult to understand based on the results from ref. 1, where the energy loss of light ions in the Au window of Si surface barrier detectors followed the corresponding stopping power curve.

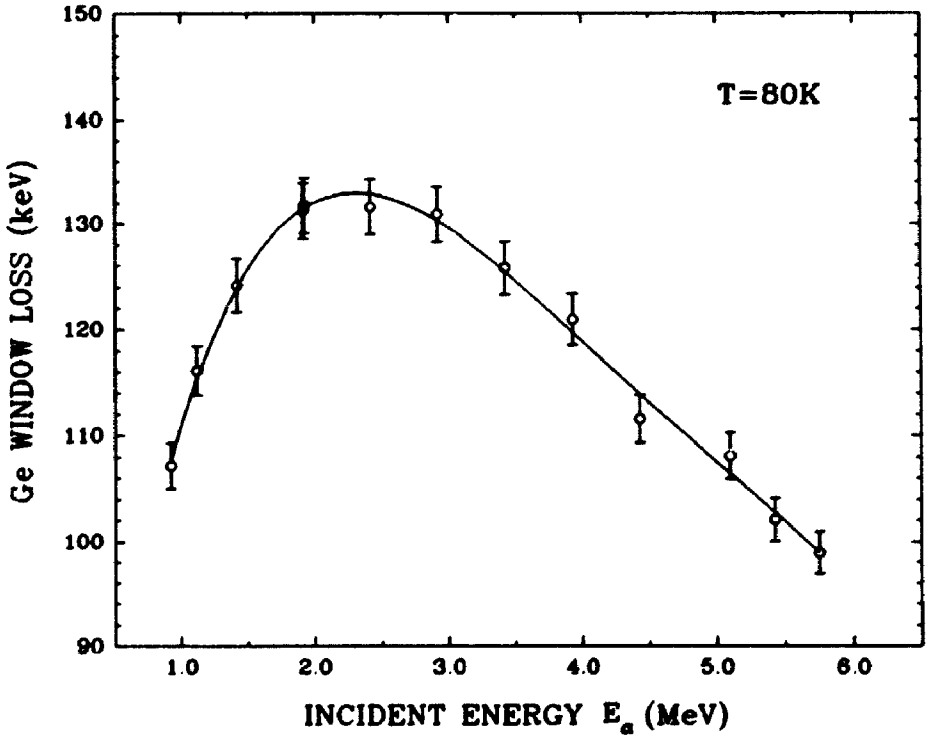

Figure 5.8 Energy loss measured for α particles in the window of the Ge detector as a function of the mean incident energy, $E_\alpha = E_0 - \Delta E_w/2$. The curve of a polynomial fit is only a guide.

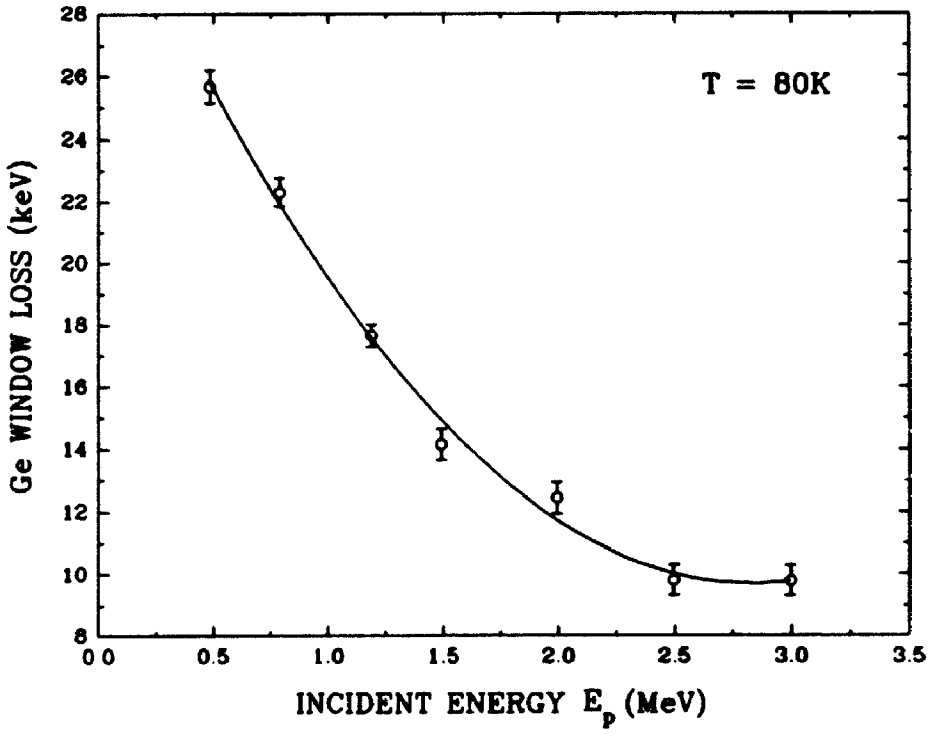

Figure 5.9 Energy loss measured for protons in the window of the Ge detector as a function of the mean incident energy, $E_p = E_0 - \Delta E_w/2$. The curve of a polynomial fit is only a guide.

Dividing the measured energy loss values by the corresponding stopping power at the mean proton or α particle energy, the window loss can be converted into an equivalent Ge thickness in microns, see Figure 5.10. The window thickness for α's increases with α energy and saturates in the region 4–5 MeV, while the window thickness for protons shows a value of 0.30 μm with ~10% fluctuations over the entire energy range. Since the stopping power maximum of protons in Ge occurs near 100 keV, the window thickness for a ^{1}H beam with the energies above 500 keV may have already reached a saturated value. For ^{7}Li and ^{3}He, the equivalent window

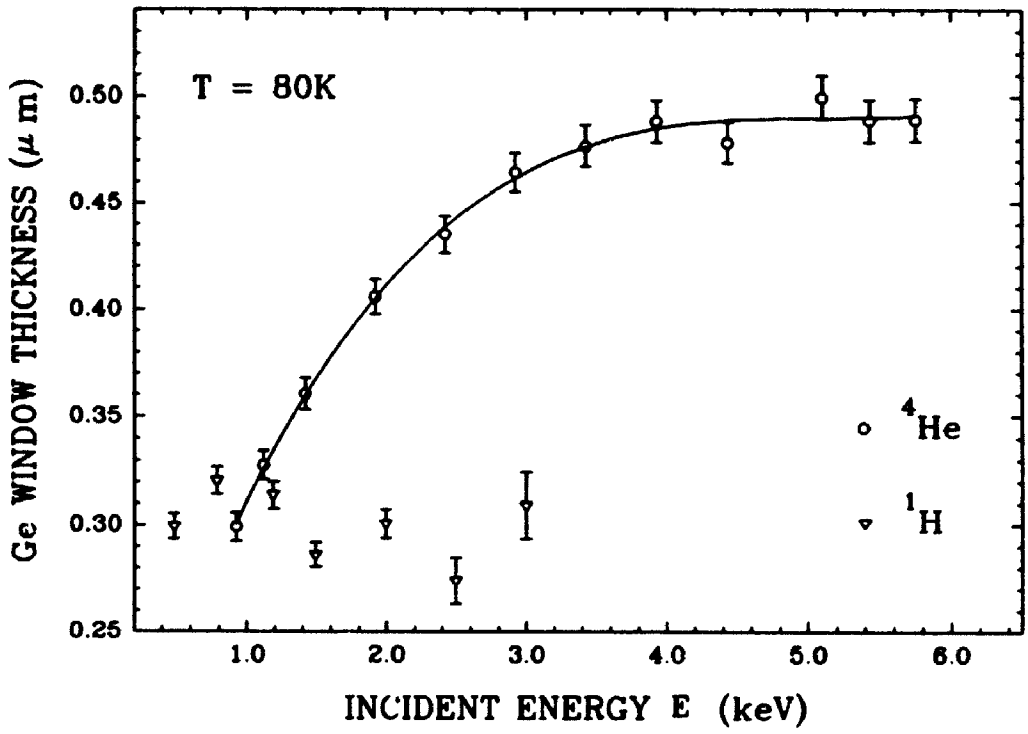

Figure 5.13 Equivalent Ge thickness of the Ge detector window obtained by using ^{1}H and ^{4}He beams and Ziegler's stopping powers [9]. It shows that a strong energy dependence of the window thickness for α particles and nearly constant effective window thickness (within 10%) for protons with different energies.

thicknesses are 0.500 μm (E_{Li} = 3.764 MeV, ΔE_w = 280.0 ± 2.0 keV, and S = 559.7 keV/μm) and 0.455 μm ($E(^3He)$ = 2.487 MeV, ΔE_w = 120.3 ± 1.8 keV and S = 270.3 keV/μm). All these data suggest that the window of the Ge detector may not be a simple conducting layer or there are other effects existing. The conclusion which

can be drawn here is: there may be another thin layer under the ion−implanted conducting layer which can cause a path dependence of the energy loss of the incident particles to compete with the process of electron−hole pair production; such extra energy loss is probably due to the existence of trapping centres, which also contribute to the so−called window energy loss, *i.e.* the fitting parameter P_1, if the tilting technique is used. Note that this observed variable window thickness represents the first evidence for such an effect.

In order to examine the response of the Ge detector at higher temperatures, the temperature dependence of the apparent window thickness of the Ge detector must be known accurately. Considering the larger window energy loss for α particles than for protons, α particles were selected for analysis. First the temperature dependence of the detector window was measured using 5.486 MeV ^{241}Am α particles. Since the temperature of the Ge detector could not be fixed arbitrarily at any temperature above 80K, the measurements of the window energy loss were performed in a dynamic fashion, *i.e.* while the detector temperature was rising. Specifically, the pulse heights of the α particles were measured at tilt angles of 0° and 30° alternatively as the temperature of the Ge detector increased. During the course of measuring each spectrum, the temperature of the detector had changed ≤ 2° (~10 min.; the temperature rising rate of the detector can be reduced by keeping the LN_2 trap and the wall of the Ge chamber cold); the counting time was dictated by the α source strength. From the data of pulse height versus the temperature of the detector, the pulse height at each angle for a given temperature (80K≤T≤170K) could be easily interpolated by polynomial fitting. Therefore, the window energy loss

at different temperatures was derived by applying Equation 5.2 and Equation 5.3:

$$P_1 = \frac{P(0°) - P(30°)}{sec30° - 1}$$
$$P_0 = P(0°) + P_1 \qquad (5.7)$$

For the accelerated α particles, the beam intensity was not a problem so that each spectrum was acquired in ~1 min., within which time the temperature of the Ge detector changed by less than 0.2°. The pulse height data were taken at the fourteen 'unanomalous' angles successively as the temperature increased, *e.g.* see Figure 5.11. Then, by fitting Equation 5.3 to the fourteen interpolated pulse height data (see Figure 5.12) at a given temperature, the temperature dependence of the detector window energy loss was obtained. For example, Figure 5.13 shows the temperature dependence of the window energy loss for α particles at three different energies. Of course, the latter method should provide a more precise measure of the window energy loss than the two angle determination mentioned above.

Figure 5.14 summarizes both the energy and temperature dependence of the window energy loss for α particles. Two unanticipated results are revealed, which makes the window problem even more complicated. First, the window energy loss changes dramatically with detector temperature, *i.e.* the window energy loss at T=173K (−100°C) was reduced to ~70% of its value at 80K. Secondly, the maximum value of the window energy loss seemed to gradually shift from ~2.2 MeV at 80K to ~1.5 MeV at ~173K, approaching the stopping power maximum. Once again, the measurements suggest that the window may be more complicated than a simple conducting layer. The window problem will discussed further in section 5.4.

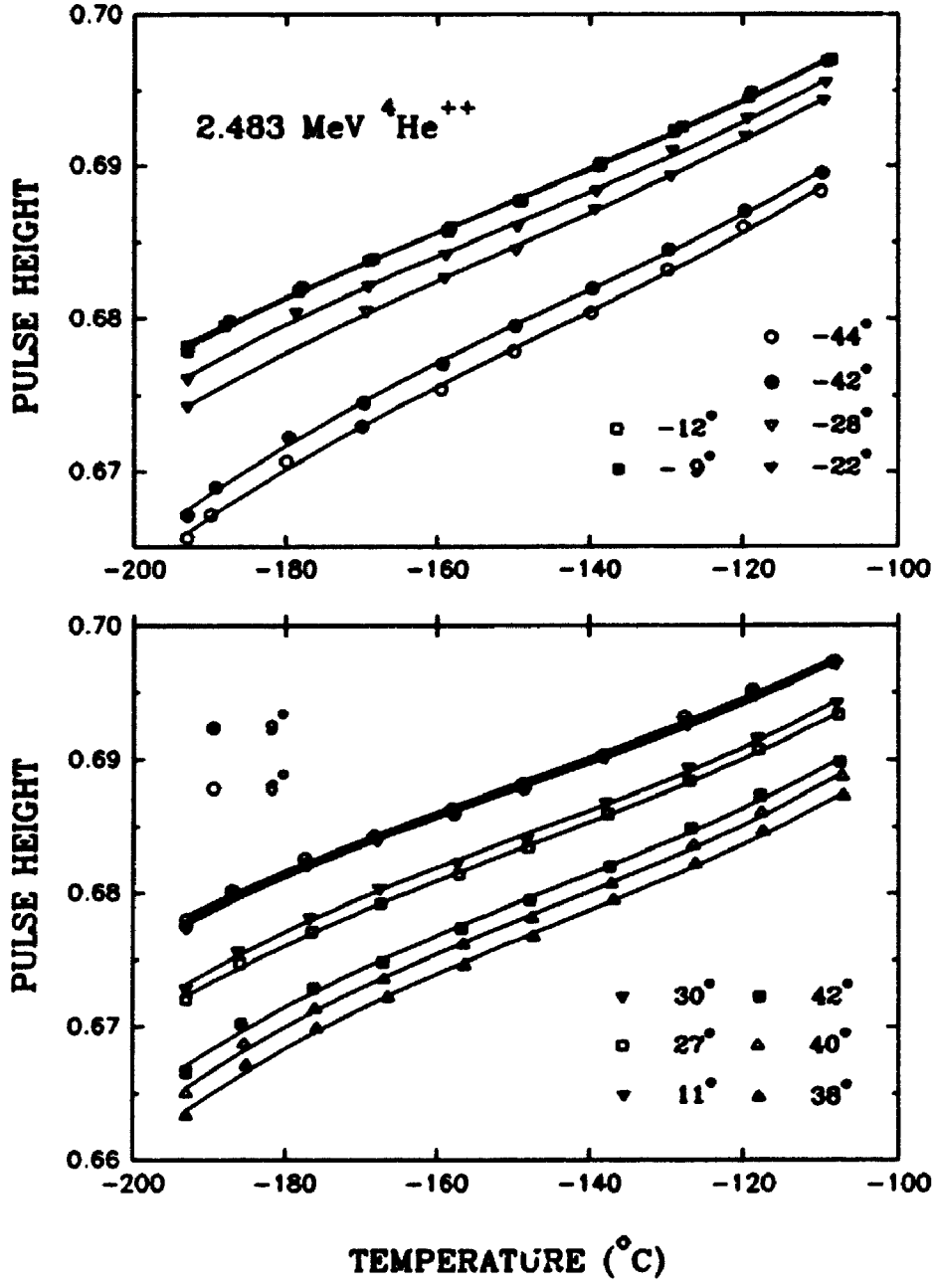

Figure 5.11 Pulse height data for ~2.483 MeV $^4He^{++}$ at the fourteen selected angles as a function of detector temperature. The solid curves are the results of polynomial fitting. Each datum is measured within a temperature change of ~0.5K.

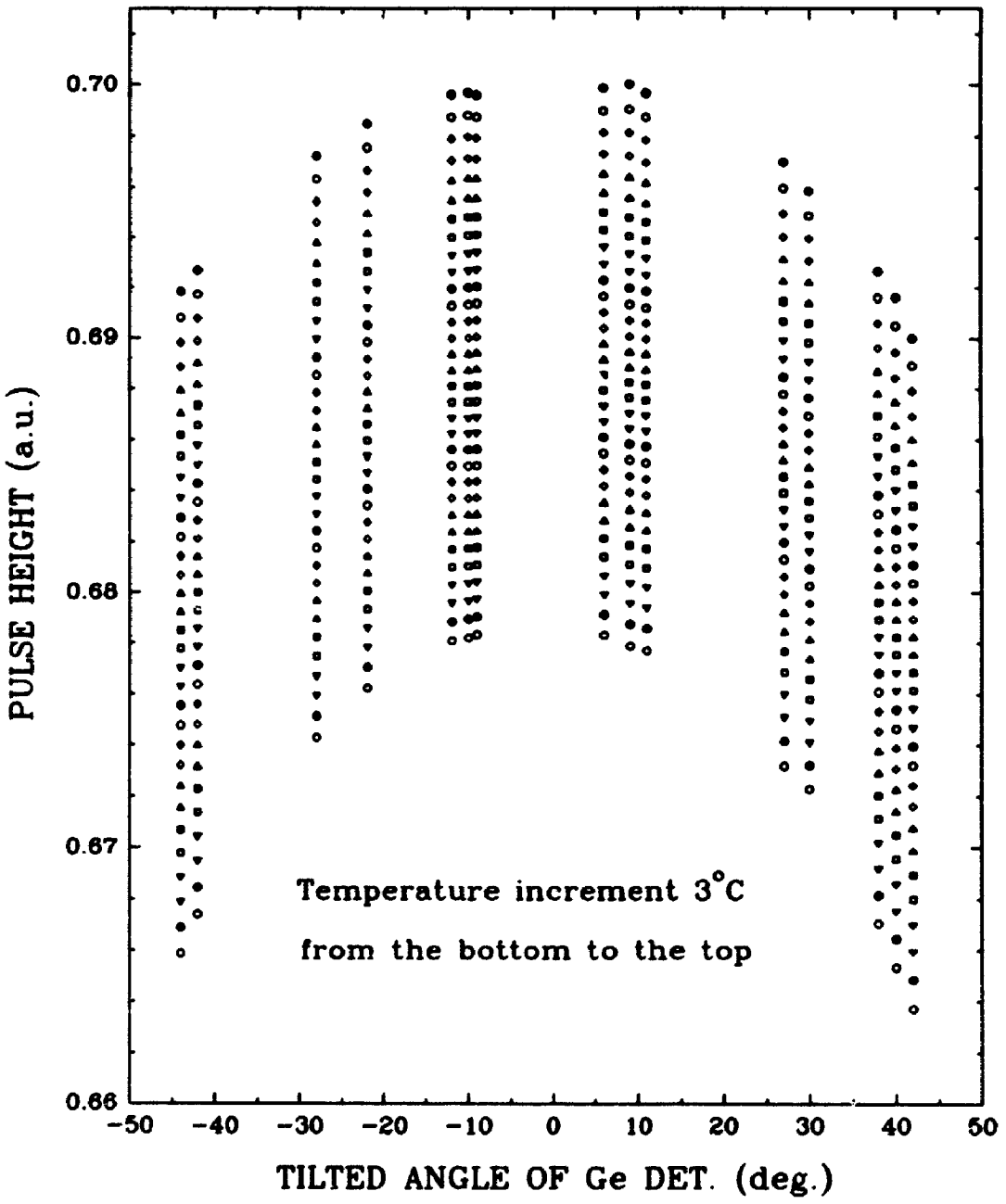

Figure 5.12 Tilting pulse height data at a given temperature for the selected fourteen angles are interpolated from the fits in Figure 5.11. The lowest and the highest data points in each column correspond to −193°C and −100°C. The temperature increment in each column is 3°C. From 14 data points measured at the same temperature, the window energy loss can be derived.

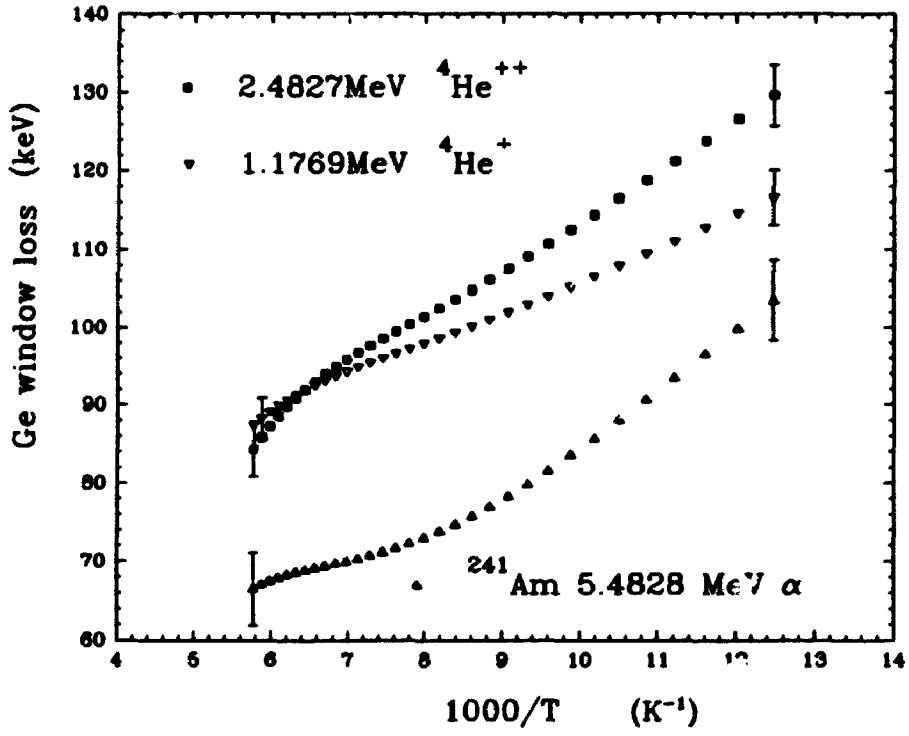

Figure 5.13 Temperature dependence of the window energy loss for three different energy α particles. More than 30% change of the window thickness is found from 80K to 170K.

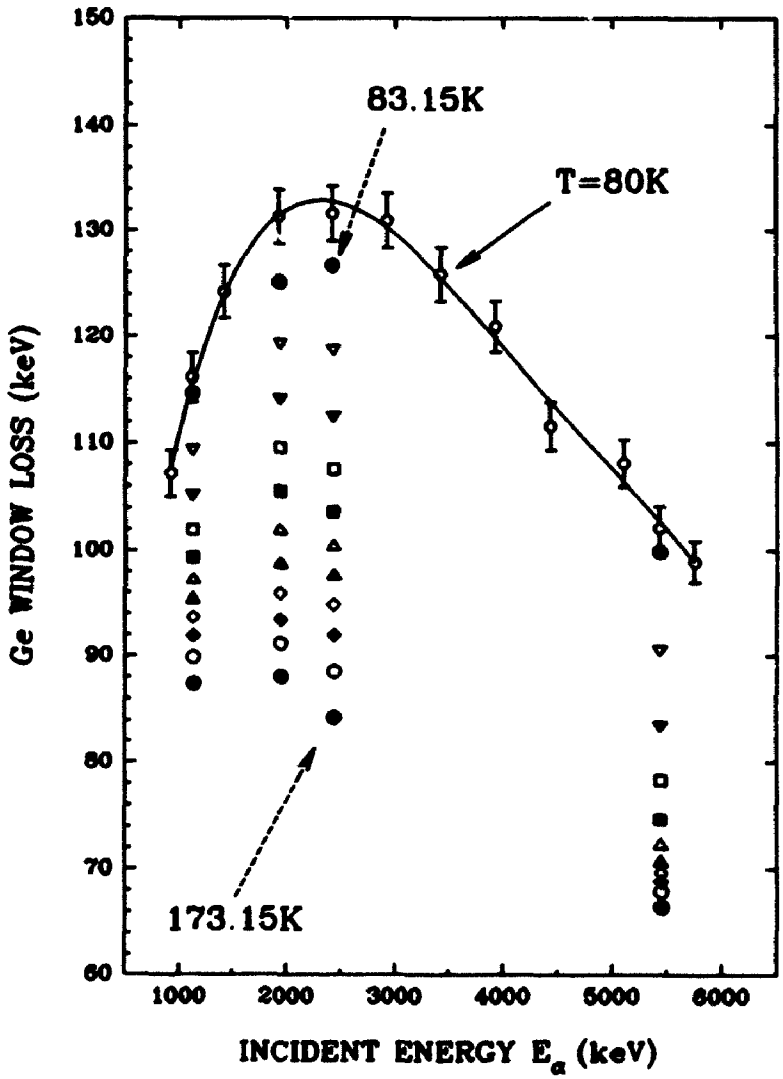

Figure 5.14 Summary of the temperature effect on the effective window thickness of the Ge detector for different energy α particles.

5.2.3 Bias dependence of the window thickness

As mentioned in chapter 2 and the beginning of this chapter, the electric field can penetrate into the window layer of semiconductor detectors [2]. It is believed that a stronger electric field can reduce recombination of electron–hole pairs created by the incoming radiation. On the other hand, a stronger electric field may cause further multiplication of electron–hole pairs. To inspect how the bias of the Ge detector affects the window thickness, the window energy loss was measured for several values of the bias voltage: 400V, 700V, 1000V and 1200V, using a 2.5 MeV α beam. No change of the window energy loss was found with the bias and the data agreed well with the previous measurement at a bias of 1000V, see Figure 5.15. This observation indicates that increasing the bias above the value required for total depletion does not cause the electric field to penetrate into the window layer any further. The α pulse height increased by ~0.3% when the bias rose from 400V to 1200V, while the 1.4 MeV γ–ray pulse height only increased by ~0.06%. Since the ionization of γ–rays is not localized, the plasma density is lower for γ's than for α particles. The increase of α pulse height with increasing bias is likely due to carrier recombination, see section 6.3.

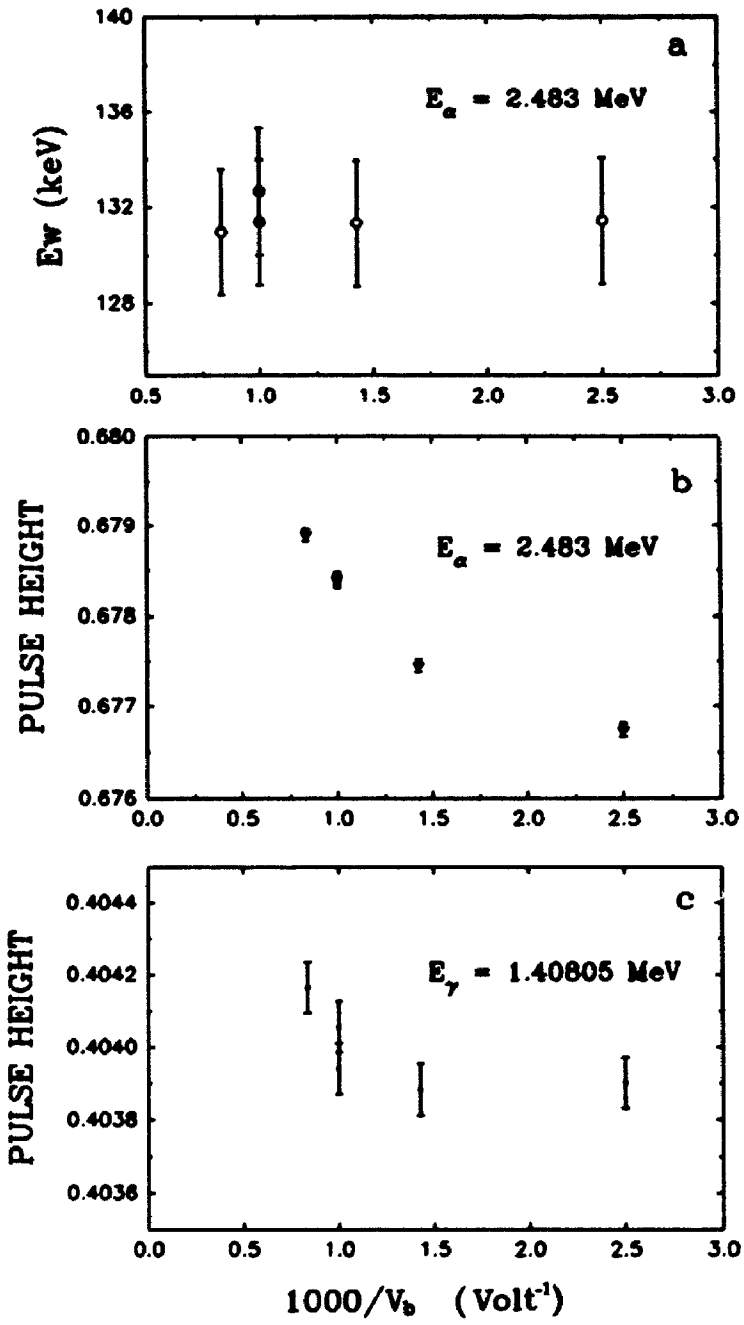

Figure 5.15 Bias dependence of the apparent pulse heights for α and $\gamma-$rays; (a) the window thickness is unchanged above the bias of 400 V; (b) the pulse height for 2.483 MeV α's changes by ~0.3%; (c) the pulse height for 1.40805 MeV γ rays changes by ~0.06%.

5.3 Channeling and Monte Carlo simulations

Channeling of energetic particles occurs when the particles are aligned with a major symmetry direction of a single crystal – either axial or planar; the channeled particles are gently steered by the atom rows or planes, without having close encounters with the lattice atoms and thereby reducing significantly any small impact parameter events such as elastic backscattering. A parameter called the critical angle is introduced to describe the channeling alignment such that channeling only occurs if the incident angle of the particles with respect to the direction of a major axis or atomic plane of the crystal is less than the critical angle. Theoretically, the critical half–angle can be estimated [12], which depends on the specific axial or planar direction and has the form

$$\Psi_{1/2} \propto \left(\frac{Z_1 Z_2}{E}\right)^{1/2} \tag{5.7}$$

where Z_2 is the atomic number of the target atom, and Z_1 and E are the atomic number and energy of the incident particle, respectively. Because the region between the atomic rows or planes has a lower electron density, the stopping power for channeled particles may be significantly different from that for nonchanneled particles. According to the equipartition rule of energy loss [15] the energy loss of projectiles due to close collisions equals that due to distant collisions at high projectile velocity. This rule then suggests that the stopping power for channeling directions can be reduced by as much as a factor of two.

From the tilting measurements for the detector window thickness, the anomalous pulse heights were always found near θ_{det} –values of $-38°$, $-30°$, $-20°$,

-5°, 12°, 24°, 33° (see Figure 5.7), where α peaks with high energy shoulders and proton peaks with higher or lower pulse heights as well as larger FWHM can be seen in the spectra. The small step angular tilting measurements have shown a different result: for proton beams, the pulse height increases sharply at the anomalous detector angle within ~0.1°, see Figure 5.7; for ^{4}He beams, the high energy shoulders of the α peaks gradually develop to become high energy peaks near the detector angles of -5.5° and 33.25°, see Figure 5.16–18. At other "abnormal" angles, these features are not so prominent as those at -5.5° and 33.25°. Clearly, the results strongly suggest that channeling effects are present in these data. Later, the manufacturer (EG&G Ortec) acknowledged that the Ge crystal was cut from a (100) crystal in order to reduce the cost, rather than cut off–axis as suggested by the Ortec technical literature. It appears that the detector angle of ~-5.5° most likely corresponds to (or close to) the <100> axial direction and that planar channeling is occurring for the detector tilt angle of 33.25°. In order to confirm this suggestion, detailed data using a two–axis goniometer are needed. In the spectra, the high energy α(Au) peak must correspond to channeled α particles.

The energy separation between the double α(Au) peaks at the channeling angles is so large, *e.g.* 30–40 keV for 1.5 MeV α's, that only the channeling effect of α particles in the detector window layer could render such a large separation. Although the difference in the nuclear energy loss for channeled and nonchanneled particles can make a small contribution to the separation (the total nuclear loss for α particles incident in a random direction is ~9 keV), the major part of the energy difference of the channeled and nonchanneled ions must originate from channeling

of incident ions in the partially damaged window layer.

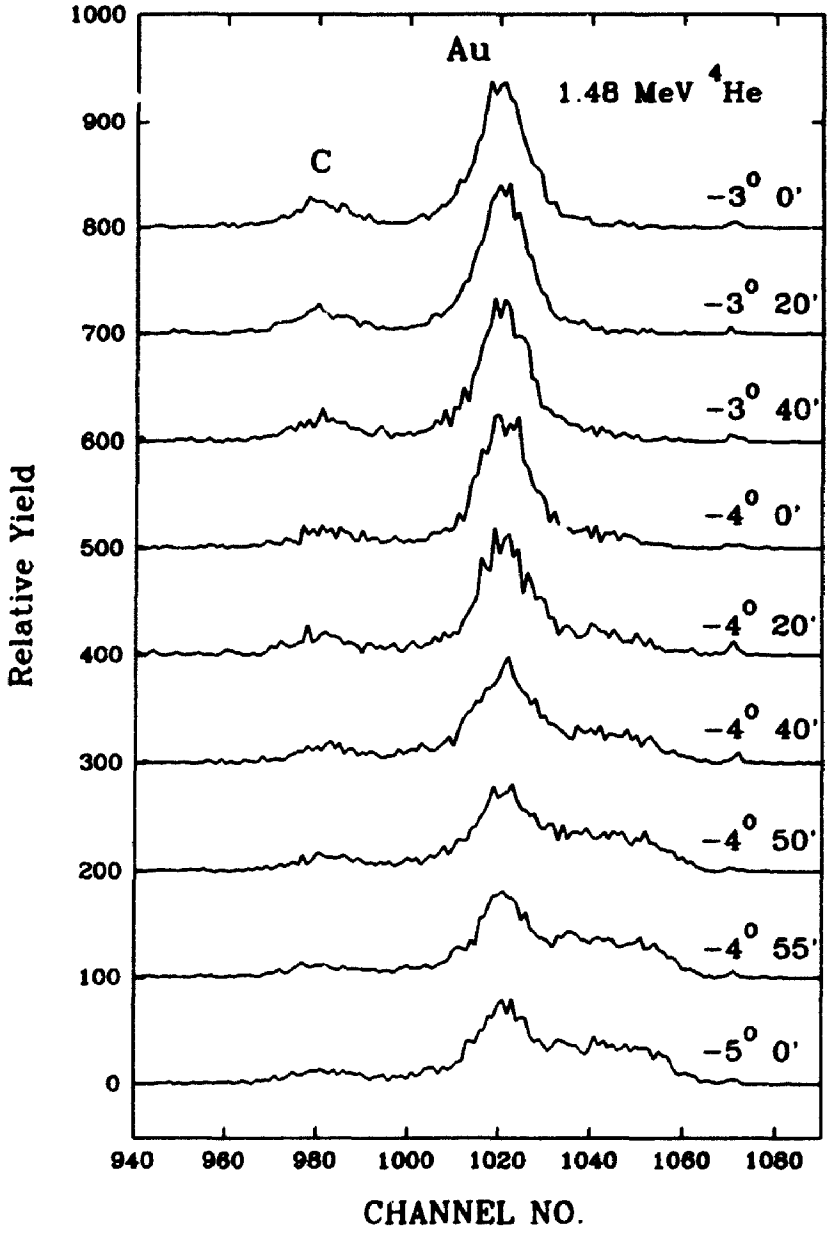

Figure 5.16 Channeling effect in the Ge detector for ~1.477 MeV α particles scattered from the Au/C foil near the normal incident angles to the detector. Successive traces are offset vertically by 100 units.

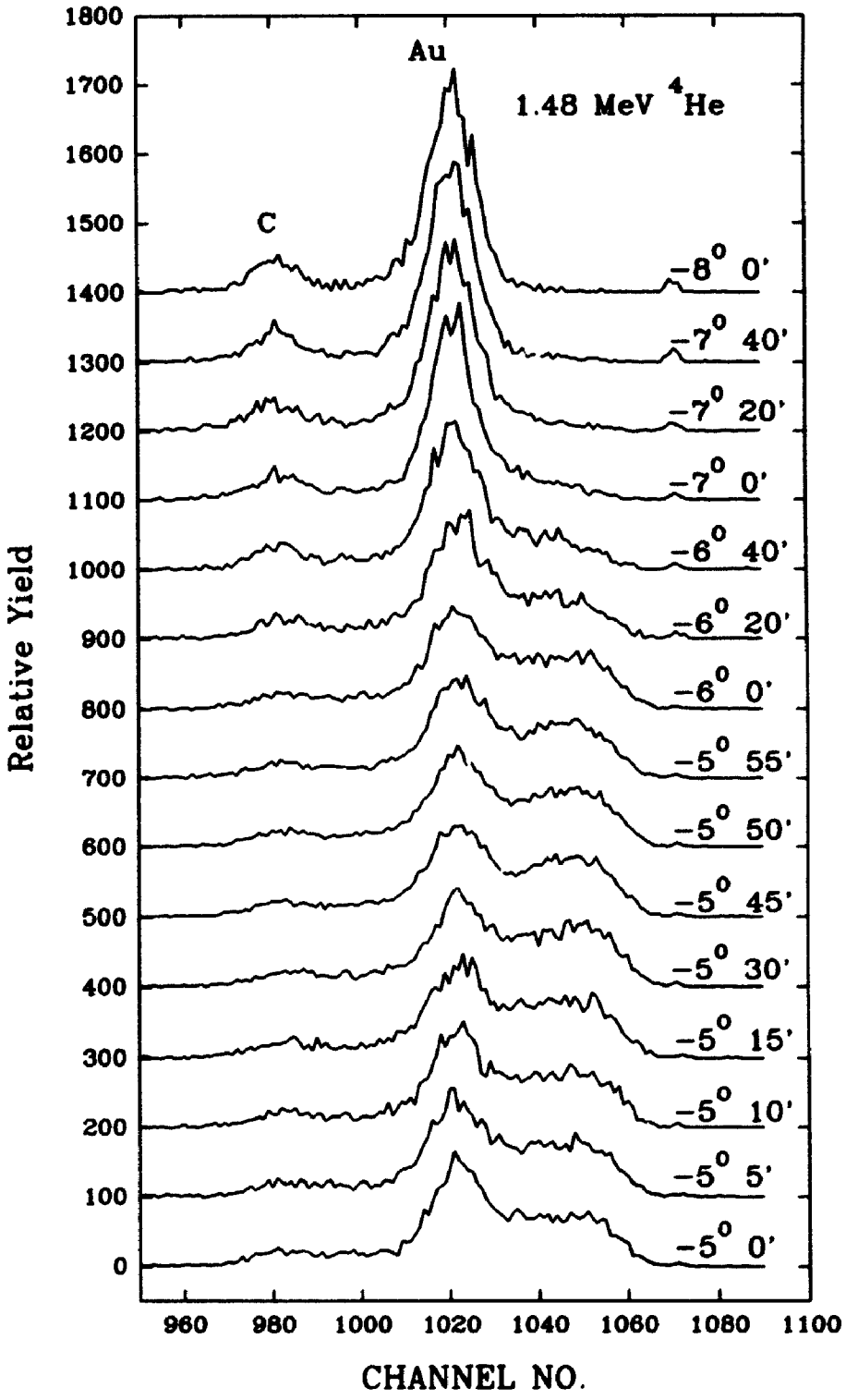

Figure 5.17 Channeling effect in the Ge detector for ~1.477 MeV α particles scattered from the Au/C foil in the Ge detector, as continued from Figure 5.16.

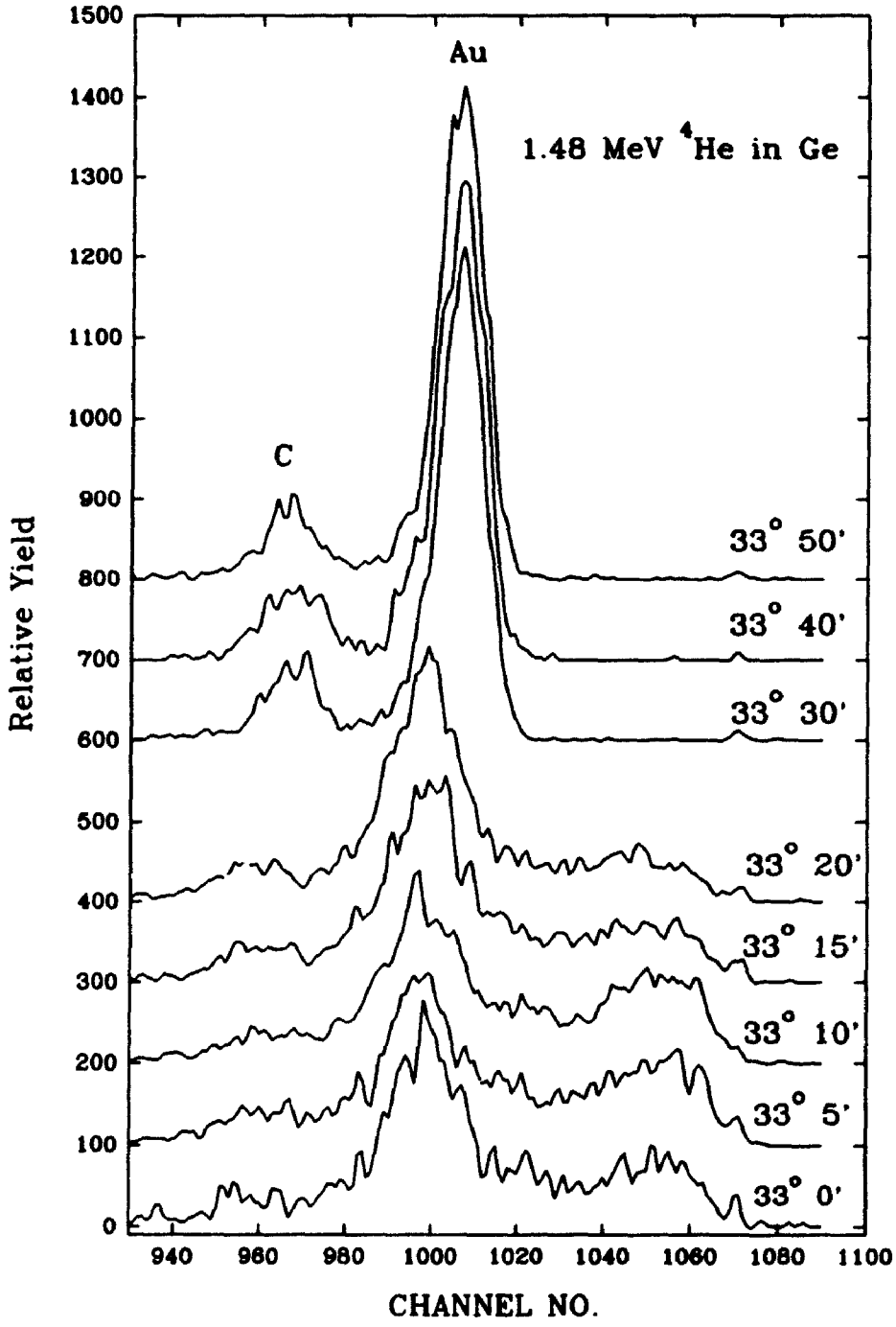

Figure 5.18 Channeling effect in the Ge detector for ~1.477 MeV α particles around the detector angles of 33°−34°. Clearly a shift of nonchanneled peaks in the channeling spectra (θ=30° − 33° 20') relative to random peaks in the normal spectra ($\theta \geq$ 33°30').

The critical half−angles for axial channeling in Ge <100> are 0.64° for 1.5 MeV ^{4}He and 0.51° for 1.2 MeV ^{1}H [12], and smaller critical angles are expected in planar directions. Channeling is not only restricted by the critical angle containing the parameters in Equation 5.7, but also depends on the beam spread (±0.1° used here) and crystal perfection. In channeling spectra for α particles, the higher energy α(Au) peak must correspond to channeled α particles due to a smaller electronic stopping power than that for nonchanneled particles, which comprise the lower energy α(Au) peak. For 1.2 MeV protons, the window energy loss is so small that the channeled and nonchanneled peaks cannot be totally separated with the existing resolution. At lower energy, the double peaks of the channeled and nonchanneled protons can be seen. It is also evident that pulse heights for nonchanneled peaks near or at the anomalous detector angles show smaller values than the expected random values, *e.g.* the dips on the pulse height curve in Figure 5.7. This phenomenon arises from those particles incident at angles near to the critical angle which may experience an increased stopping (compared to random) [16]. An increased probability of such close collisions for incident particles means that the particles penetrate through the high electron density region in Ge, leading to a larger energy loss than for random directions.

Figures 5.19−5.23 show several examples of channeling spectra for different ions with different energies. It seems that alignment of incident ions at θ_{det}≈33.2° is better than at θ_{det}≈5°−6°, so that the channeled and nonchanneled peaks can be separated well at θ_{det}≈33.2° with less continuum yield between them, and the higher−Z ions channel better than lower−Z ions due to their larger critical angle for

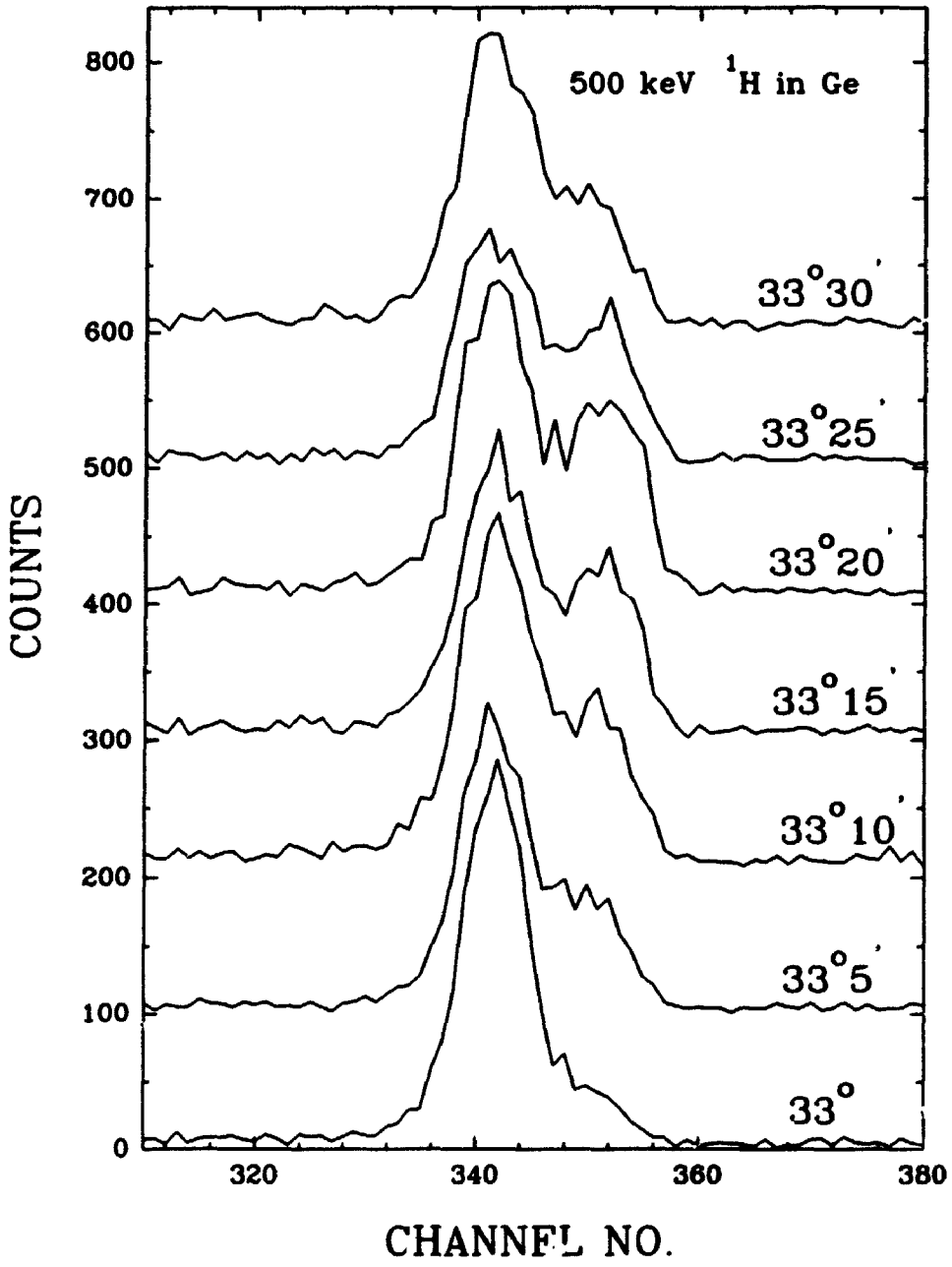

Figure 5.19 Channeling effect in the Ge detector for 495 keV protons scattered from the Au foil for the detector angles of 33°−33.5°.

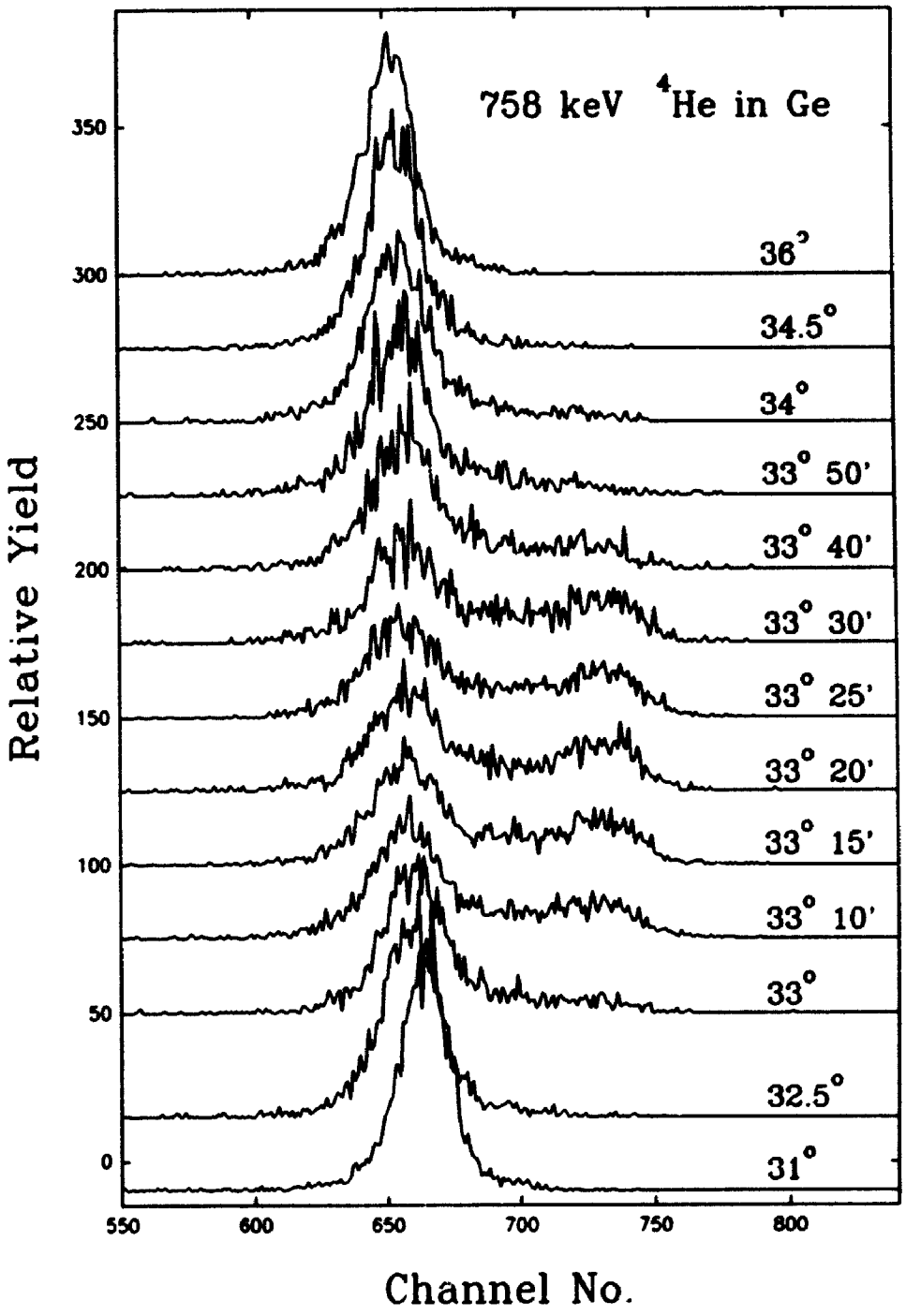

Figure 5.20 Channeling effect in the Ge detector for 759 keV α particles scattered from a self−supporting C foil (10 $\mu g/cm^2$) for detector angles of 31°−36°.

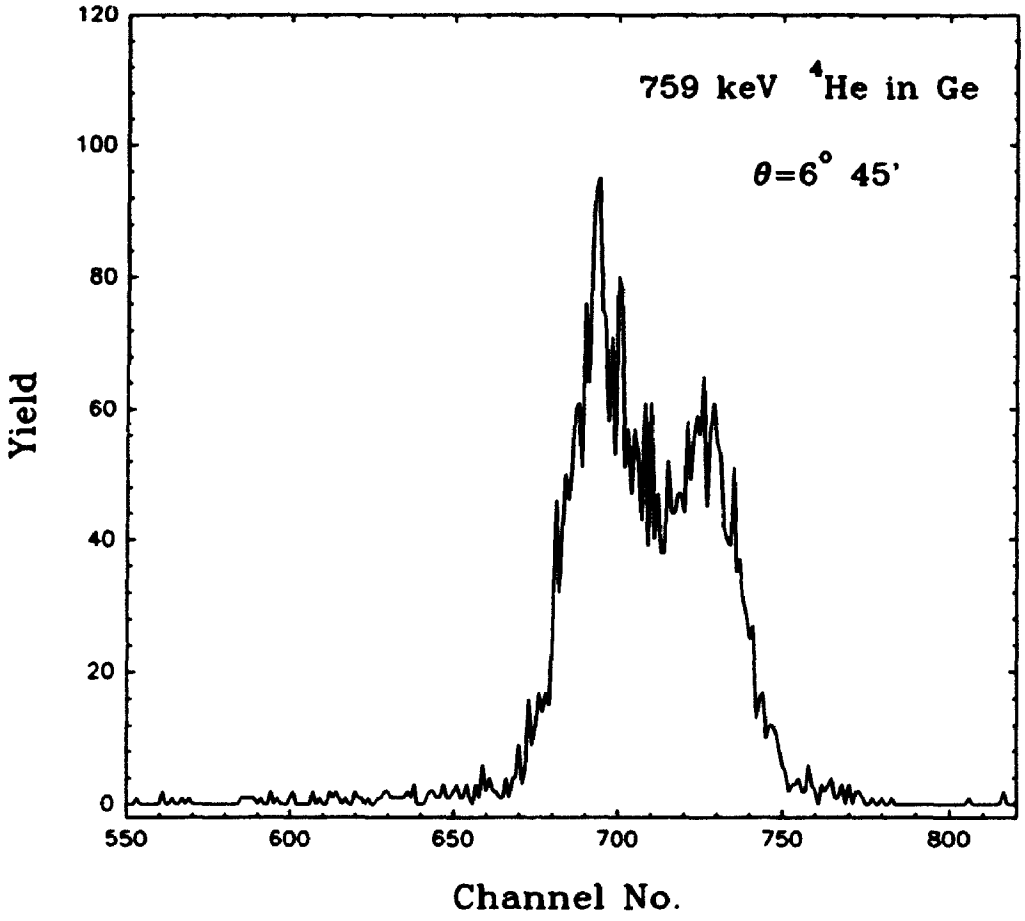

Figure 5.21 Channeling effect in the Ge detector for 759 keV α particles scattered from the C foil (10 $\mu g/cm^2$) at a detector angle of 6°45'.

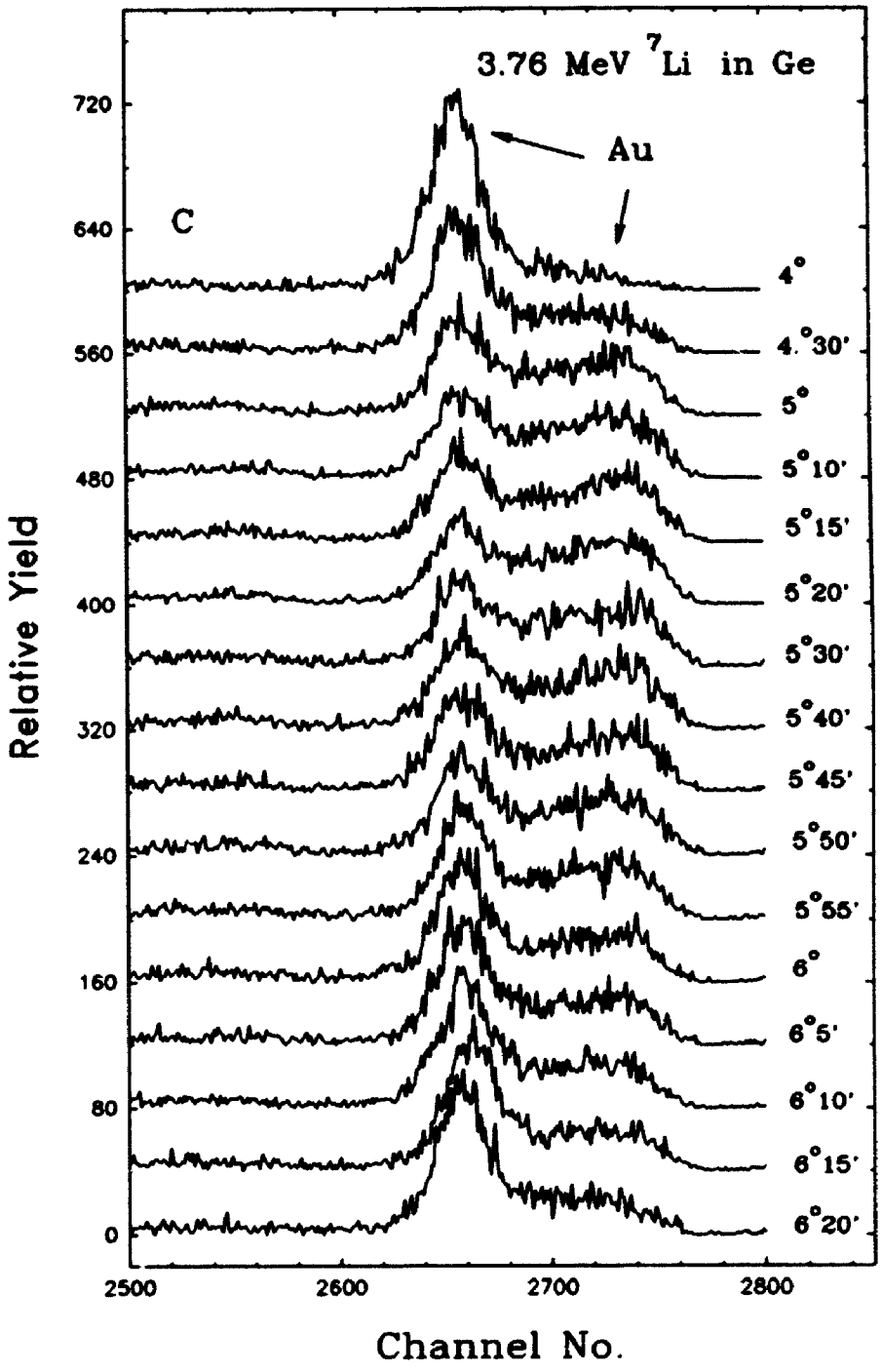

Figure 5.22 Channeling effect in the Ge detector for 3.764 keV $^{7}Li^{++}$ particles scattered from the Au/C foil for detector angles of 4°−6°20'.

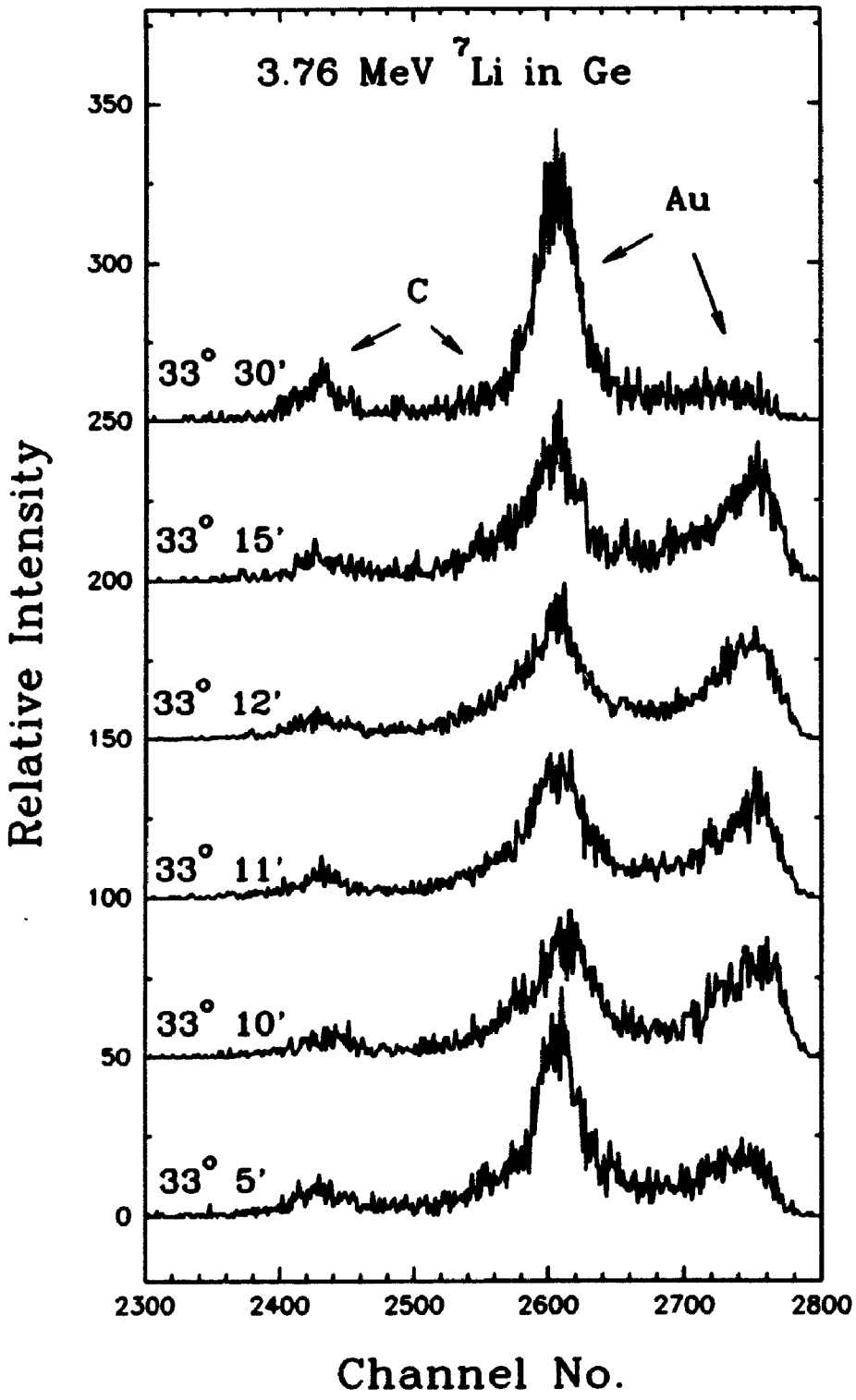

Figure 5.23 Channeling effect in the Ge detector for 3.764 MeV $^{7}Li^{++}$ particles scattered from the Au/C foil for detector angles of 33°5'–33°30'.

channeling. If we assume that the energy difference between the channeled and nonchanneled peaks is due only to the channeling of particles in the detector window layer, the stopping power ratio for channeled and nonchanneled particles can be estimated, see table 5.1. The window energy losses (ΔE_w) for the detector are the values for normal incidence, which corresponds to a dial reading of $\theta_{det} \sim -2.5°$. The energy is the projectile energy before entering the detector window. The peak positions were chosen according to the most probable values.

Table 5.1: Stopping ratio for channeled and nonchanneled particles

Ion beam	E_w det. window	θ_{det}	$E_{ch}-E_{nonch}$ (θ_{det})	S_{ch}/S_{nonch}
494.6keV ^{1}H	25.7 keV (N.I.)	33.33°	12(±2)keV	62% (66%)
758.7keV ^{4}He	97 keV (N.I.)	6.75°	20(±3)keV	79%
758.7keV ^{4}He	97 keV (N.I.)	33.42°	50(±3)keV	58% (65%)
1.477MeV ^{4}He	124 keV (N.I.)	5.83°	32(±3)keV	74%
1.477MeV ^{4}He	124 keV (N.I.)	33.17°	73(±4)keV	52% (58%)
3.764MeV ^{7}Li	280 keV (N.I.)	5.67°	101(±5)keV	64%
3.764MeV ^{7}Li	280 keV (N.I.)	33.17°	194(±5)keV	44% (51%)

The smallest energy loss ratio for channeled and nonchanneled particles in the detector window is ~44%; no correction has been made to allow for a reduced nuclear energy loss for channeled particles. The magnitude of this effect is not easy to estimate, as it depends on the beam energy, crystal quality, channeling direction in the crystal, and the temperature of the crystal. From previous studies [17] and an

approximate calculation based on the random and well−channeled backscattering spectra of 1.5 MeV ^{4}He in a GaAs crystal, the channeled particles will be gradually dechanneled linearly with penetration depth - up to 40−80% of the incident ions at the end of the ion tracks. This is close to the situation in the channeling spectra near −5°, where a flat continuum yield extends from nonchanneled peaks to the channeled peaks. In the channeling spectra near 33.3°, the channeled peaks are well separated from the nonchanneled peaks, suggesting that the particles can channel through to the end of their tracks with reduced nuclear energy losses. If no nuclear energy loss for the channeled particles is assumed, the stopping power ratio in Table 5.1 will be the values in parentheses. It was found that the stopping power of channeled protons in the axial directions of Ge crystals was about 30−48% of the random stopping power for proton energies from 1.5 MeV to 6.57 MeV [18], based on backscattering measurements.

In order to verify the assumption of channeling in the detector window, a Monte Carlo simulation was used to study the channeling of monoenergetic ions in thin Ge crystals [19]. Only the energy distribution of transmitted ions through a thin Ge crystal were recorded. In the Monte Carlo program, a modified binary collision model was used for collisions between incident ions and lattice atoms, taking into account the influence of the nearest lattice atoms. The maximum impact parameter between channeled ions and lattice atoms was 2 Å. The Ziegler−Biersack−Littmark (ZBL) "universal potential" [9] was used in the calculation of the deflection function. A three−component model was applied to the energy loss in each ion−atom collision [20,21]. This model assumes that the random stopping cross section is a sum of the

stopping cross section for the core and the valence electrons, where the stopping for valence electrons is further divided into the stopping due to single particle excitations of valence electrons and plasmon excitations [21]. The trajectory of each ion was followed and energy losses in each collision were summed. The residual energies for all transmitted ions were recorded regardless of their angular position. The energy spectrum of transmitted ions was finally convoluted with the intrinsic resolution of the Ge detector. The surface of the Ge crystal is set at (100) and the crystal orientation could be changed by $0^\circ \leq \theta \leq 6^\circ$ and $0^\circ \leq \phi \leq 360^\circ$. Figures 5.24–5.26 show some of the simulated results for 1.5 MeV α particles channeling in the (100), (110) and (310) planar directions of a 0.3 μm thick Ge crystal. The nonchanneled peaks (low energy peaks) show slightly higher or lower pulse height than the pulse height of the random energy loss of α's in the Ge crystal, and the energy loss ratio of channeled (higher energy peaks) and nonchanneled α's in the Ge crystal is ~67% for the (100) plane, ~52% for the (110) plane and 71% for the (310) plane, which qualitatively agrees with the experimental results.

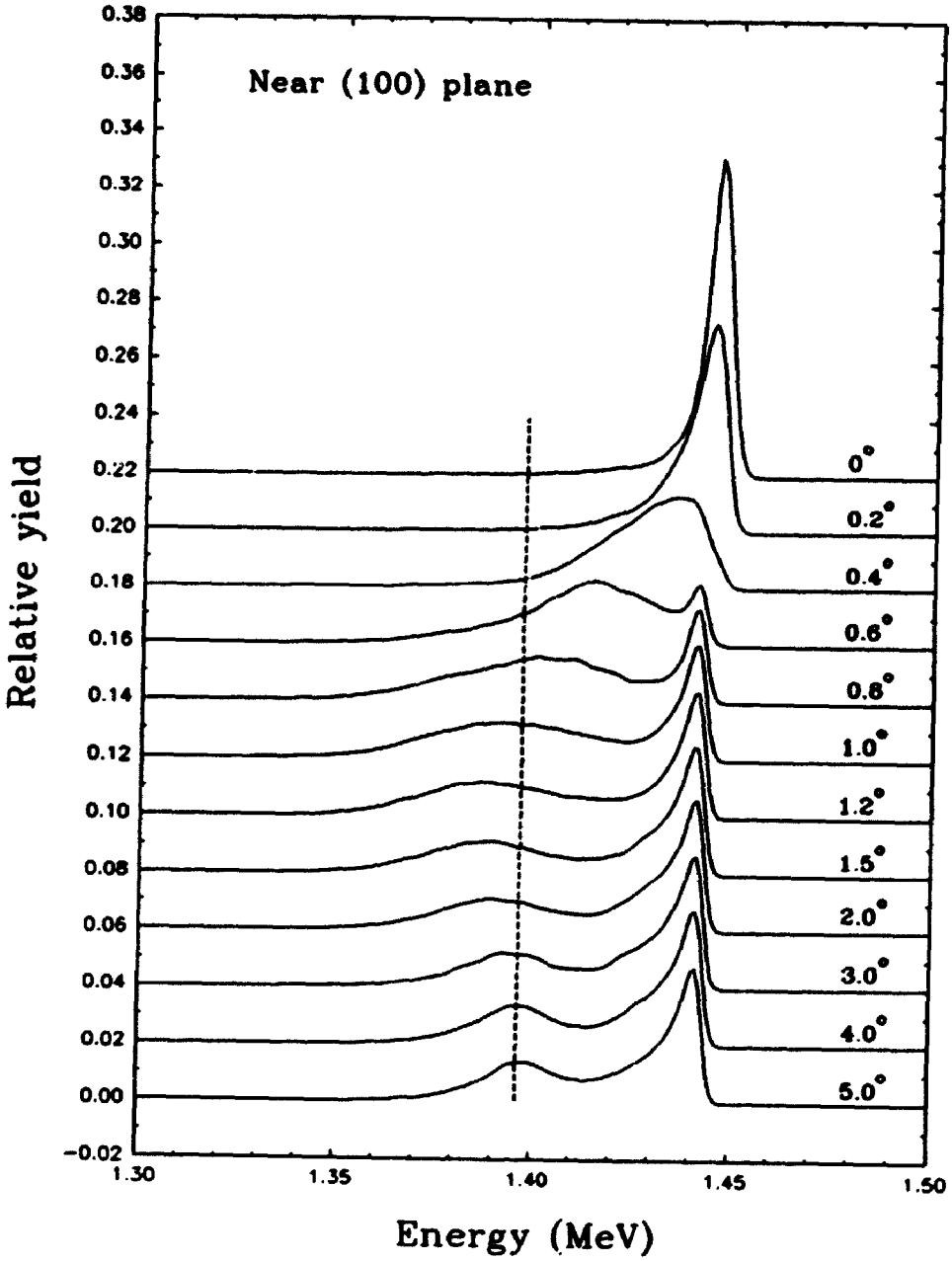

Figure 5.24 Monte Carlo simulation of 1.5 MeV α particles in (100) direction of a 0.3 μm thick Ge crystal as function of θ, which is shown for each curve. The dashed line is the energy predicted by Ziegler's theory after penetrating through the Ge crystal.

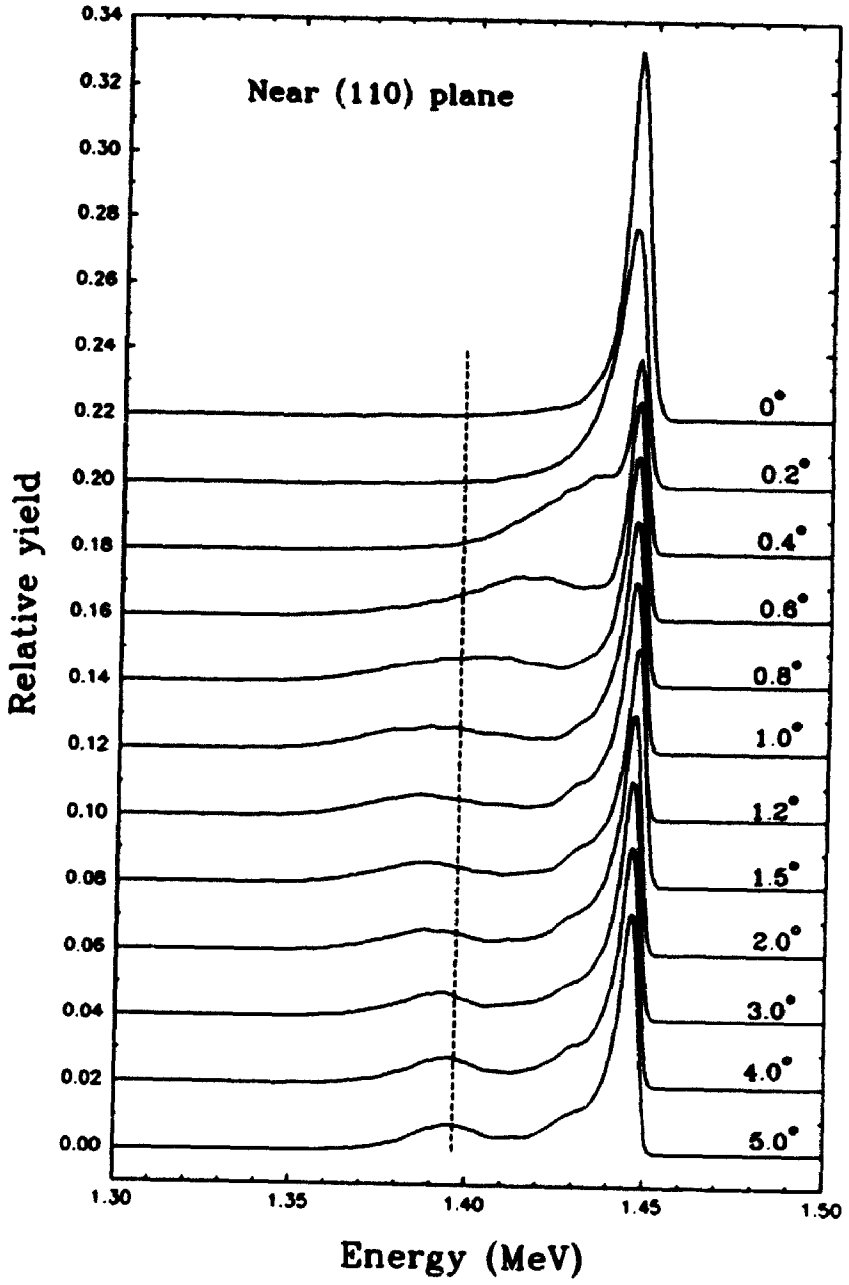

Figure 5.25 Monte Carlo simulation of 1.5 MeV α particles in (110) direction of a 0.3 μm thick Ge crystal as function of θ, which is shown for each curve. The dashed line is the energy predicted by Ziegler's theory after penetrating through the Ge crystal.

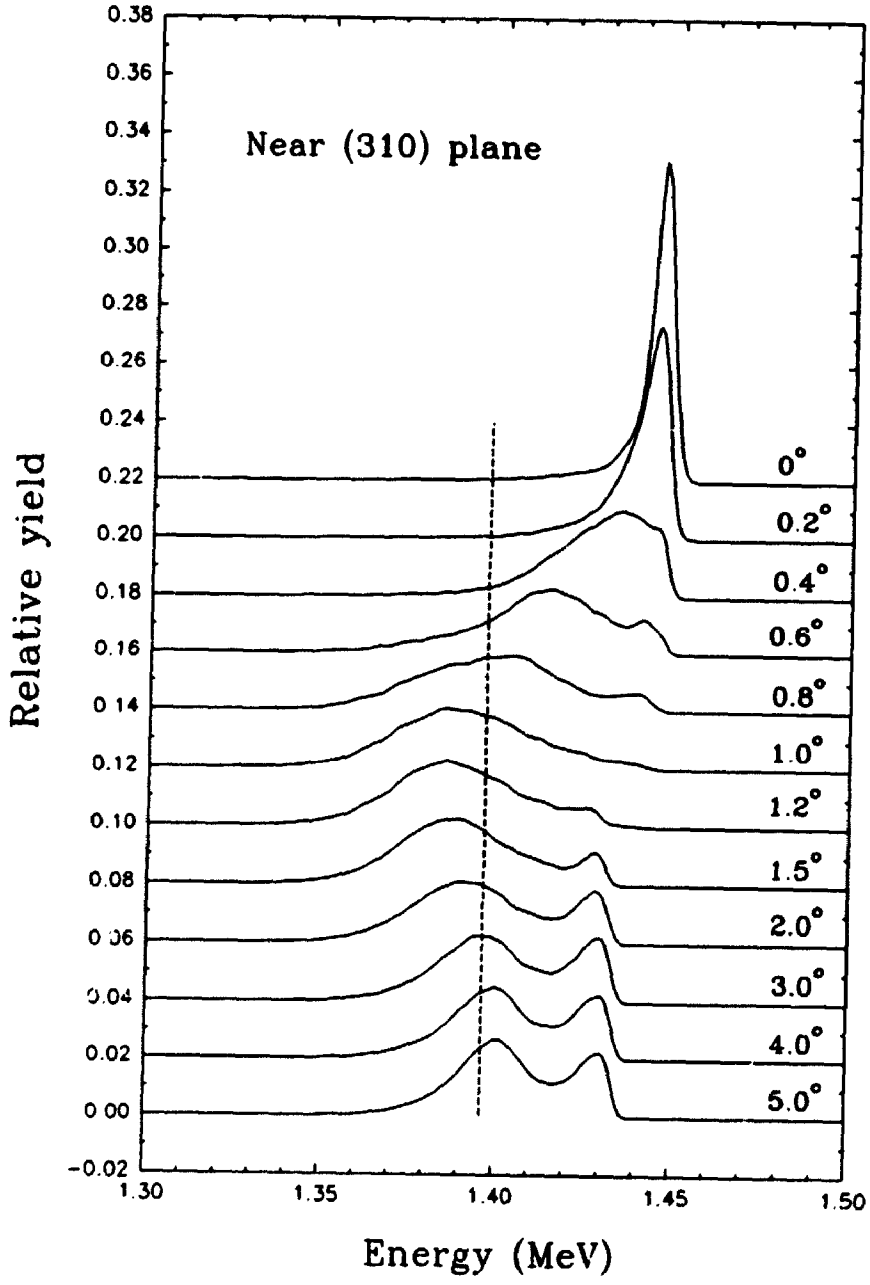

Figure 5.26 Monte Carlo simulation of 1.5 MeV α particles in (310) (ϕ = 18.34°) direction of a 0.3 μm thick Ge crystal as function of θ marked for each curve. The dashed line is the energy predicted by Ziegler's theory after penetrating through the Ge crystal.

5.4 The window of the Ge detector

The window of the detector has to be reconsidered after the channeling effect was observed due to the cutting of the Ge detector crystal near the (100) plane. First, since the critical half-angle of 40 keV boron ions channeling in the <100> axial direction of Ge crystal is about 7°, it is possible that channeling effects could occur during boron implantation if the incident angle of the boron ions with respect to the <100> direction is less than 7°. Therefore, the range of implanted boron ions could exceed its value for amorphous Ge. According to the carrier concentration measurements [7,10], 20 keV boron implantation ($10^{14}/cm^2$) in the <111> and <110> directions of the Ge crystal gave a flat and high charge carrier concentration, ~$10^{18}/cm^2$, up to depths ~0.35μm and ~0.6μm, respectively.

The results reported here for the equivalent window thickness of the Ge detector (see Figure 5.10) have shown the boron distribution depth must be larger than the value of 0.1 μm predicted by the TRIM calculation – the "random" range. This observation indicates that channeling did occur during implantation of boron ions into the Ge detector crystal. It is very difficult to estimate the boron penetration. Regarding the large change of the window energy loss with the temperature of the detector, the temperature dependence of channeling for ^{7}Li ions near the detector tilting angle of 33.2° was examined to check whether the thickness of the window layer changed with the temperature of the Ge detector. The energy difference between the channeled and nonchanneled peaks decreases about 34% as the temperature of the Ge detector went from 80K to 150K, close to the change of the window energy loss with the temperature, see Figures 5.27–5.28, which suggests

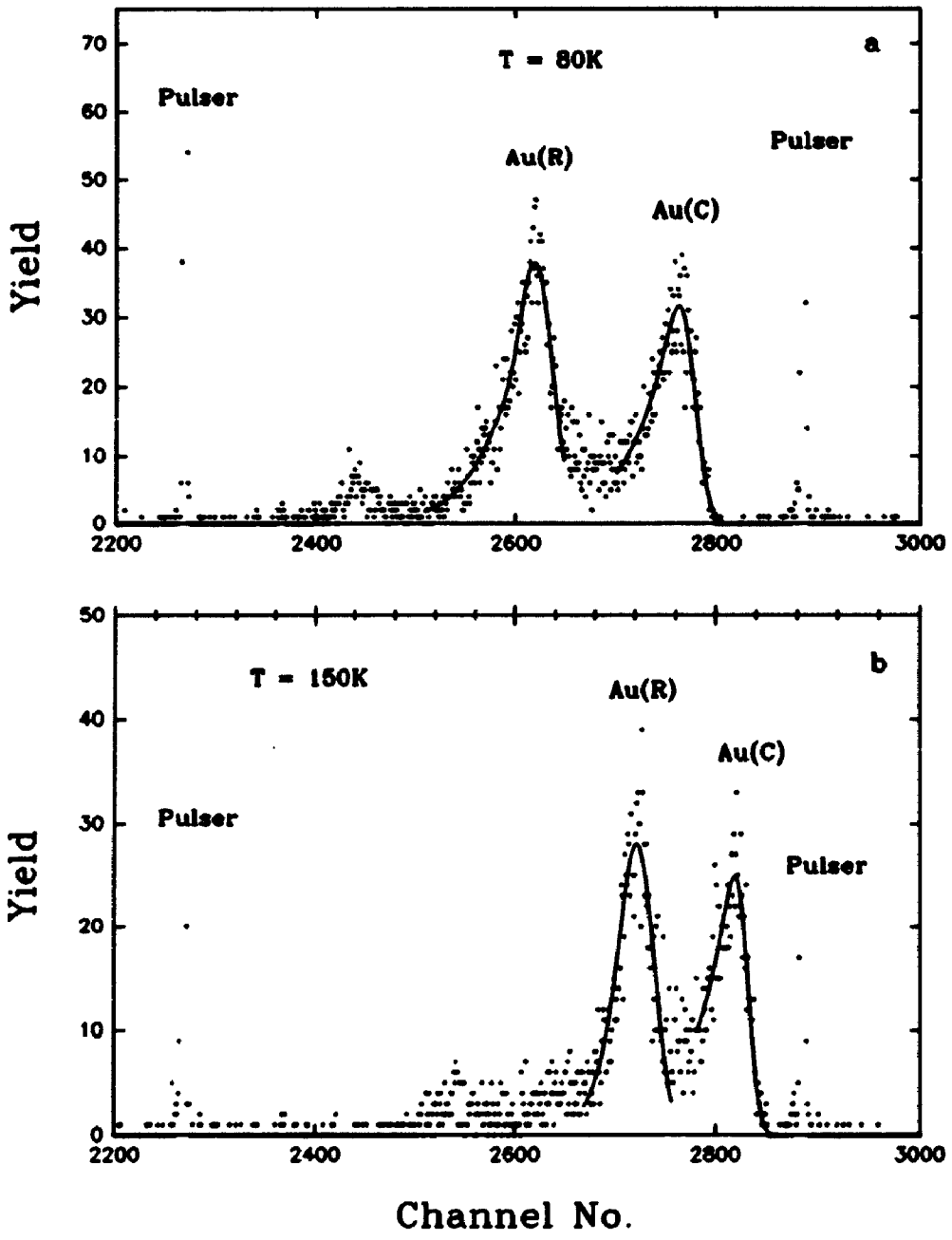

Figure 5.27 Channeling spectra for 3.764 MeV $^{7}Li^{++}$ (after scattering from the Au/C foil) in the window layer of the Ge detector, (a) at T = 80K and (b) at T = 150K. The solid curves are the fits for the nonchanneled Au peaks, Au(R), and channeled Au peaks, Au(C), respectively. The test pulse peaks exceed the vertical scales.

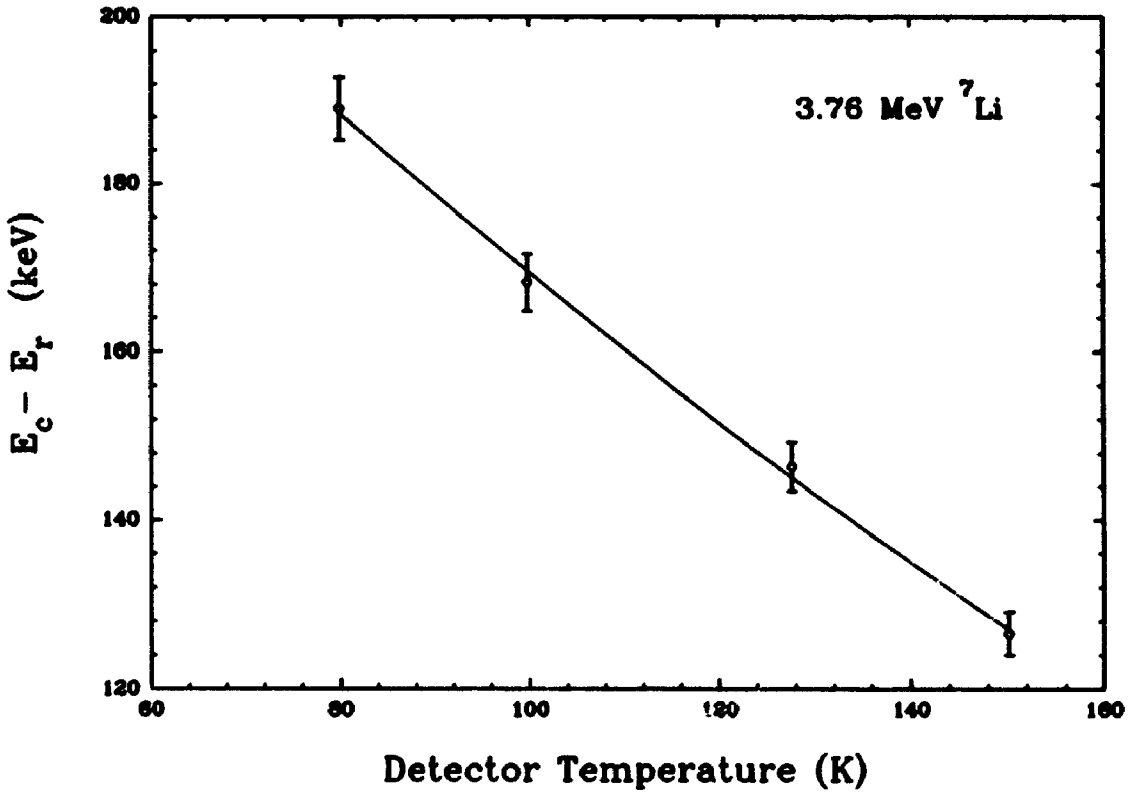

Figure 5.28 Temperature dependence of the energy difference between the non−channeled and channeled (Au) peaks. 34% change is shown from 80K to 150K. See Figure 5.27 as a reference.

that the thickness of the window layer does decrease with increasing temperature of the detector. The energy loss straggling effect in the detector window should then make a smaller contribution to the FWHM of a monoenergetic α peak as the window layer decreases. But the measurements of the temperature dependence of peak FWHM−values for α particles and for test pulses show that a smaller change of the measured straggling, $(\text{FWHM})^2_\alpha - (\text{FWHM})^2_{\text{test pulse}} - (\text{FWHM})^2_{\text{beam}}$, than that predicted

by Bohr straggling in the window, see Figure 5.29.

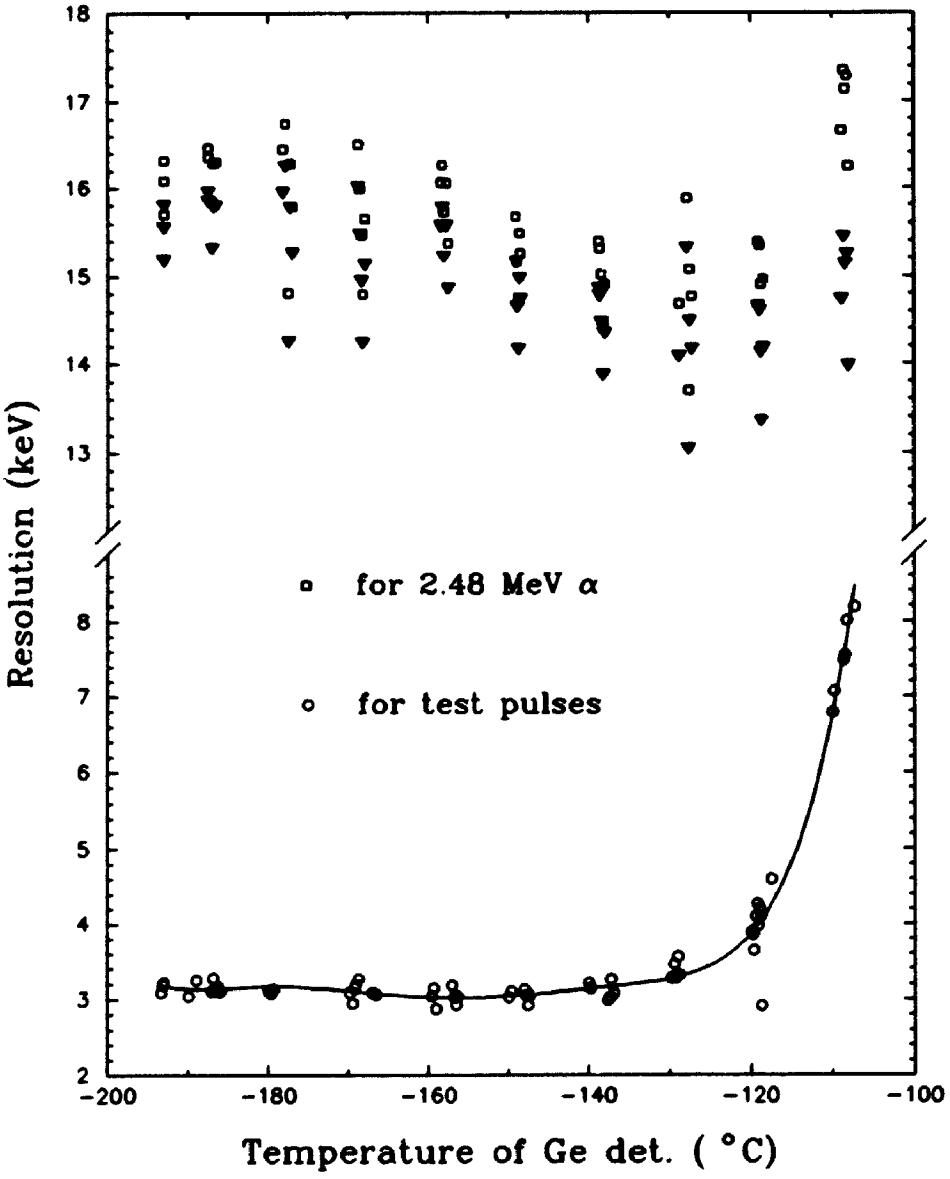

Figure 5.29 Temperature dependence of the FWHM for 2.483 MeV α particles (□) and the test pulses (○). (▼) are the FWHM after subtracting the contributions from the test pulses and the scattering foil, *i.e.* the FWHM due to energy loss straggling in the detector window.

The energy loss straggling for α particles in the C/Au scattering foil is only about 2 keV. Thus, the change of the apparent window thickness with the crystal temperature is not simply due to a variation of its thickness with the temperature. It may be possible that there are many defects at the interface of the boron implantation layer and the Ge bulk crystal, which can cause defect−related recombination of the electron−hole pairs along the path of the incident particles in the interface layer. The total amount of the carrier loss due to such recombination should depend on the length of the projectile track in the interface layer. Therefore, this effect will be included in the measured window energy loss (*i.e.* in the parameter P_1), without distorting the curve shape of the detector window PH-θ_{det} data. On the other hand, since all the data from the tilting measurements follow the curve defined by Equation 5.3 very well, it suggests that this tilting method must be reliable. Such defect−induced recombination seem to be enhanced at a lower temperature so that extra electrons or holes created by α particles are exhausted and the apparent detector window layer becomes thicker. This is similar to the temperature dependence of trapping effects discussed by Ryan in his early study [22]. Additionally, with regard to channeling effects, a fit to all the tilting data should be appropriate since the parameter desired is the **average** energy loss in the window, which means averaging over all directions including those exhibiting channeling effects. The origin of the projectile energy dependence of the window energy loss remains an open question.

References

1. W.N. Lennard, H. Geissel, K.B. Winterbon, D. Phillips, T.K. Alexander and J.S. Forster, Nucl. Instr. and Meth. A248 (1986) 454.
2. J.M. Caywood, C.A. Mead and J.W.Mayer, Nucl. Instr. and Meth. 79 (1970) 329.
3. J.W. Mayer and S.S. Lau, "Electronic Materials Science: For Integrated Circuits in Si and GaAs", MacMillan Publishing Company, 1990.
4. TRIM Version 92, written by J. F. Ziegler, see reference 9.
5. K. S. Jones and E. E. Haller, J. Appl. Phys. 61 (1987) 2469.
6. J. P. Ponpon, J. J. Grob, R. Stuck, P. Burger and P. Siffert, 2nd Int. Conf. on Ion Implantation in Semiconductors, Garmisch−Partenkirchen, eds. I. Ruge and J. Graul (Springer, 1971) p.420.
7. H. Herzer, S. Kalbitzer, J.P. Ponpon, R. Stuck, and P. Siffert, Nucl. Instr. and Meth. 101 (1972) 31.
8. K.S. Jones and E.E. Haller, Appl. Phys. 61 (1987) 2469.
9. J. F. Ziegler, J. P. Biersack and U. Littmark, "The Stopping and Range of Ions in Solids", Vol. 1, Pergamon Press, 1985.
10. H. Herzer and S. Kalbitzer, 2nd Int. Conf. on Ion Implantation in Semiconductors, Garmisch−Partenkirchen, eds. I Ruge and J. Graul (Springer, 1971) 307.
11. A. Grob, J. J. Grob and P. Siffert, Nucl. Instr. and Meth. 132 (1976) 273.
12. J.W. Mayer and E. Rimini, "Ion Beam Handbook for Material Analysis", Academic Press, Inc., 1977.

13. M. Bundar, D. Glavic, A. Kodre and Z. Smit, Nucl. Instr. and Meth. B31 (1988) 456.

14. A. Rytz, At. Data Nucl. Data Tables 23 (1979) 507.

15. E. Bonderup, Lecture notes: "Penetration of Charged Particles Through Matter", p.57.

16. D. V. Morgan, "Channeling: Theory, Observation and Applications", Wiley, 1973.

17. M. A. Kumakhov and G. Shirmer, "Atomic Collisions in Crystals", (1980), English Translation in 1989.

18. K. Morita and N. Itoh, J. Phys. Soc. Jap. 30 (1971) 1430.

19. A. Dygo and A. Turos, Phys. Rev. B40 (1989) 7704.

20. B. R. Appleton, C. Erginsoy and W.M. Gibson, Phys. Rev. 161 (1967) 1330.

21. A. Dygo and A. Turos, Phys. Lett. A127 (1988) 281.

22. R. D. Ryan, IEEE Trans. Nucl. Sci. NS−20 (1973) 473.

Chapter 6

IONIZATION ENERGY FOR CHARGED PARTICLES IN Ge

Since the ionization energy, ε_0, is known and independent of γ−ray energy, it is easier to obtain the ionization energy for ions, ε_{ion}, by comparison with ε_0 rather than to measure ε_{ion} directly. In order to perform the comparison experimentally, many parameters must be known precisely, such as the detector window energy loss, nuclear energy loss and the energy of the incident ions. In previous chapters, the γ−ray calibration of the test pulses, the detector window energy loss, and the calculation of the nuclear energy loss, *etc.* have been carefully determined. In this chapter, the detailed method of how to derive the ratio $\varepsilon_{ion}/\varepsilon_0$ will be described based on experimental data. The response of the Ge detector to energetic ions is discussed in terms of ε_{ion}.

6.1 Pulse height measurements and determination of $\varepsilon_{ion}/\varepsilon_0$

The advantage of the method, measuring the response spectra of the detector simultaneously for γ and energetic ions, is that $\varepsilon_{ion}/\varepsilon_0$ can be determined very accurately. Therefore, it provides important information about the response of the Ge detector to energetic ions. In the following, a detailed description for deriving $\varepsilon_{ion}/\varepsilon_0$ from the pulse height measurements is given.

When using accelerated ion beams, the incident ions are scattered by a thin self-supporting film into the Ge detector at a scattering angle of 20° with respect to the incident beam direction. The energy, E_0', of the incident ions before entering the

Ge detector was determined from the calibration of the Tandetron accelerator and considering the energy loss in the scattering foil (C/Au or Au) and the kinematic factor. Assuming that E_0 is the energy of the energetic ions bombarding the scattering foil, then E_0' can be calculated by Equation 5.6 for a Au/C scattering foil. For the case of the self-supporting Au scattering foil, $N_C = 0$ in Equation 5.6. The kinematic factor, k, used for ^1H, ^3He, ^4He and ^7Li ions scattered from Au atoms to 20° in the forward direction are 0.99938, 0.99815, 0.99755 and 0.99571, respectively. After considering the window and non-ionizing energy losses, the effective energy of the incident ions dissipated in creating electron-hole pairs in the Ge detector can be calculated

$$E_{ion} = E_0' - \Delta E_w - \Delta E_n \tag{6.1}$$

When using radioactive α-sources, the source thickness (see Section 5.2) must also be considered and then Equation 6.1 becomes

$$E_{ion} = E_0 - \Delta E_s - \Delta E_w - \Delta E_n \tag{6.2}$$

The source energy loss, ΔE_s, is also measured by the tilting technique where now the source is tilted with respect to the detector rather than vice versa. The number of electron-hole pairs is proportional to the measured pulse height and is given by the following relations:

$$N_{eh} = \frac{E_{ion}}{\varepsilon_{ion}} \qquad for\ \alpha\ particles \tag{6.3}$$

$$N_{eh} = \frac{E_\gamma}{\varepsilon_0} \qquad for\ \gamma\text{-}rays \tag{6.4}$$

The ratio $\varepsilon_{ion}/\varepsilon_0$ can be obtained, directly based on the pulse height data, window,

nuclear and source energy losses. In this experiment, the ratio $\varepsilon_{ion}/\varepsilon_0$ is obtained from

$$\frac{\varepsilon_{ion}}{\varepsilon_0} = \frac{E_{ion}}{E_\gamma} \tag{6.5}$$

where ε_{ion} represents the average ionization energy for the energy E_{ion}, and E_γ is the energy corresponding to the ion pulse height based on the calibration of γ−ray energy versus the γ pulse height measured simultaneously in the same spectrum (see Equation 3.2).

Since channeling effects occur for a normal incident angle of the Ge detector, the pulse height values at normal incidence were derived from the fitting parameters of the detector window tilting data, *i.e.* P_0-P_1, see Equation 5.3. At the same time, the window thicknesses were obtained from the P_1/P_0 ratio, see Equation 5.4. Again, as for the window energy loss, the pulse height values at normal incidence derived in this manner were determined from ~40 measurements rather than from a single measurement.

6.2 Ionization energies for ^{1}H, ^{4}He, ^{3}He, ^{7}Li at 80K

The ratio of ionization energy for light ions and γ-rays were measured for the Ge detector at T = 80K, with a detector bias voltage of 1000 V. The results are shown in Figures 6.1 and 6.2, and listed in tables 6.1 and 6.2 where E_γ is the γ−ray energy corresponding to the same pulse height of the ions in the same row. For protons, the Au self-supporting foil (68 μg/cm^2) was used and the C/Au (11.2 μg/cm^2 / 9.6 μg/cm^2) self-supporting foil combination for the other ions.

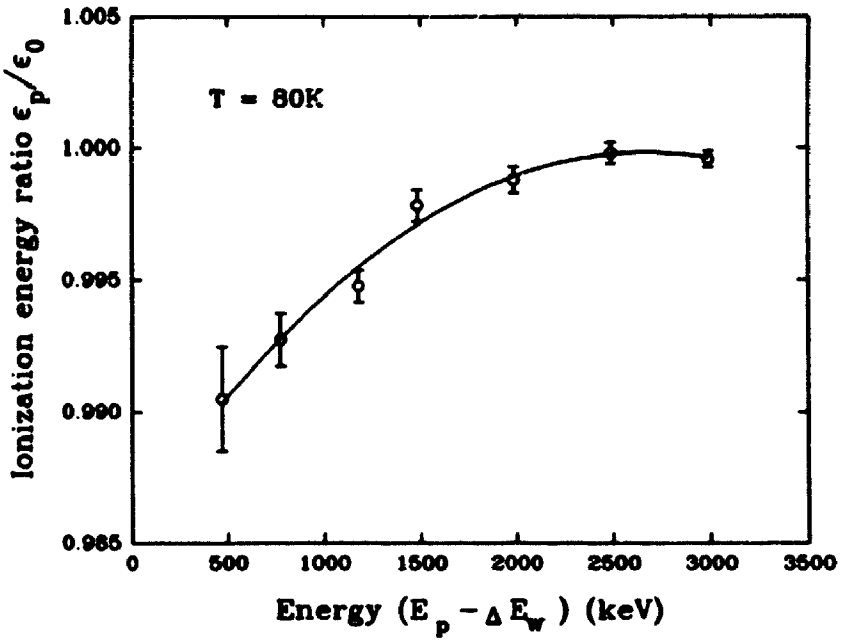

Figure 6.1 Energy dependence of the ionization energy ratio for protons versus γ−rays at 80K. The data are listed in Table 6.1.

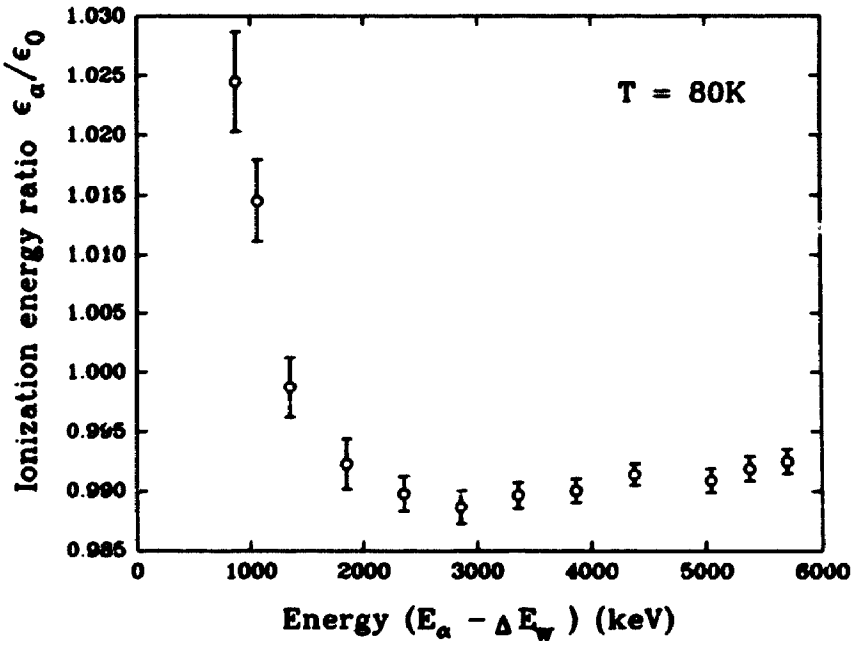

Figure 6.2 Energy dependence of the ionization energy ratio for α particles versus γ−rays at 80K. The data are listed in Table 6.2.

Table 6.1 Ionization energy for ^{1}H, ^{3}He, and ^{7}Li in the Ge detector at 80K

Ion	E_0' (keV)	ΔE_w (keV)	ΔE_n (keV)	E_{ion} (keV)	E_γ (keV)	$\varepsilon_{ion}/\varepsilon_0$
H:	494.61±0.62	25.68±0.51	1.0	467.93±0.83	472.42±0.51	0.9905±0.0020
H:	796.60±0.49	22.30±0.45	1.2	773.10±0.71	778.76±0.38	0.9927±0.0010
H:	1197.60±0.40	17.64±0.35	1.4	1178.56±0.60	1187.77±0.47	0.9948±0.0006
H:	1498.41±0.37	14.14±0.49	1.6	1482.67±0.69	1486.05±0.56	0.9978±0.0006
H:	1999.72±0.34	12.44±0.50	1.8	1985.48±0.70	1987.90±0.86	0.9988±0.0005
H:	2500.82±0.36	9.81±0.58	2.1	2488.91±0.80	2489.41±0.66	0.9998±0.0004
H:	3001.41±0.39	9.79±0.59	2.4	2989.22±0.85	2990.47±0.54	0.9996±0.0003
^{3}He:	2487.0±1.2	120.3±1.8	7.2	2359.8±2.9	2385.9±2.0	0.9890±0.0014
^{7}Li:	3764.6±3.0	280.0±2.5	25.2	3459.4±6.2	3473.2±4.9	0.9960±0.0023

Table 6.2 Energy dependence of ε_α in the Ge detector at 80K

E_0' (keV)	ΔE_w (keV)	ΔE_n (keV)	E_{ion} (keV)	E_γ (keV)	$\varepsilon_\alpha / \varepsilon_0$
976.1±2.3	107.2±1.6	8.6	860.3±3.2	839.8±1.6	1.0245±0.0042
1176.9±2.0	116.2±1.7	9.1	1051.6±3.2	1036.7±1.9	1.0145±0.0034
1478.5±1.8	124.2±1.9	9.4	1344.9±3.2	1346.6±1.7	0.9987±0.0025
1981.3±1.6	131.3±2.0	10.0	1840.0±3.2	1854.4±2.0	0.9923±0.0021
2482.7±1.2	131.6±2.0	10.2	2340.9±3.2	2365.1±1.9	0.9898±0.0015
2984.3±1.6	130.9±2.0	10.5	2842.9±3.1	2875.6±2.2	0.9886±0.0014
3485.0±1.5	125.8±1.9	10.8	3348.4±3.3	3383.5±1.8	0.9896±0.0011
3985.8±1.7	120.9±1.8	11.2	3853.7±3.2	3892.6±1.9	0.9900±0.0010
4486.5±2.0	111.6±1.7	11.5	4363.4±3.5	4401.2±1.7	0.9914±0.0009
*5156.6−ΔE_s	108.1±2.2	11.6	5033.1±3.7	5079.5±2.0	0.9908±0.0010
*5485.6−ΔE_s	102.1±1.5	11.9	5367.8±3.4	5412.0±2.1	0.9918±0.0010
*5804.8−ΔE_s	98.9±2.0	12.2	5689.9±3.7	5733.5±2.3	0.9924±0.0010

* ΔE_s = 3.8 keV ± 50%

The uncertainties in the incident energies in the first column of each table arise from two sources: (1) the uncertainty in the energy calibration of the Tandetron accelerator; and (2) an estimated 10% uncertainty in the measured thickness of the scattering foils. The former uncertainty reaches a minimum between the energies corresponding to the terminal voltage values found at the calibration energies and gets larger at both lower and higher energies, while the latter one decreases with increasing energy (*i.e.* as the stopping power decreases).

The derived uncertainties of window energy loss in P. H. units from fitting are about 1%, except for higher energy protons. The uncertainty in the nuclear energy loss for ions is difficult to estimate because values are based on calculations (see Chapter 4). For all cases, 20% uncertainty in the nuclear energy loss has been assumed in deriving the overall estimate of the uncertainty in $\varepsilon_{ion}/\varepsilon_0$, since the difference of the nuclear energy loss calculated by different approximations is $\lesssim 20\%$, see Figure 4.1.

In Figures 6.1 and 6.2, the ionization energy ratios for ^1H and ^4He approach unity as the energy of the ion increases. The largest difference of the ionization ratio observed is ~1.1% except for $E_\alpha < 1.5$ MeV. Note that $\Delta E_n/E_{ion}$ only amounts to less than half of the difference of the $\varepsilon_{ion}/\varepsilon_0$ ratio from unity. The variation of ε_p and ε_α with energy is quite similar to results obtained for Si detectors, see Figure 2.9. Obviously the rapid rise of $\varepsilon_\alpha/\varepsilon_0$ starts at an energy higher than that corresponding to the stopping power maximum and the ratio becomes larger than unity at $E_\alpha < 1.1$ MeV. This observation may suggest that there is trapping effect during the course of carrier transportation. In principle, the trapping effect will be reduced at higher

temperature because of a shorter detrapping time of the carriers [1]. There is no clear evidence of a trapping effect for protons and $\gamma-$rays, see section 6.4.

In order to examine more details about ε_{ion}, the differential change of $\varepsilon_{ion}/\varepsilon_0$ with the ion energy rather than the average ionization energy ratio tabulated in tables 6.1 and 6.2 must be investigated. Using the data in tables 6.1 and 6.2, the variation of $\varepsilon_{ion}/\varepsilon_0$ with the stopping power is derived by

$$\frac{\varepsilon_{ion}(E)}{\varepsilon_0} = \frac{\Delta E_{ion}(E)}{\Delta E_\gamma} \tag{6.6}$$

as shown in Figure 6.3. In this manner, corrections for the window energy loss and nuclear energy loss become less significant in affecting the ionization ratio, and the uncertainty in the differentials may not increase because some of the systematic errors can be cancelled in taking differences. The ionization ratio is almost constant for ^{1}H, while for ^{4}He the ratio increases as the stopping power decreases. It is believed that the ratio $\varepsilon_\alpha/\varepsilon_0$ will remain at unity below the stopping power of 0.20 keV/nm in the high energy region. If we assume that the ionization energy for protons and ^{4}He is the same as that for $\gamma-$rays above 5 MeV, then the predicted average value of $\varepsilon_\alpha/\varepsilon_p$ at 15 MeV is 0.9975($\pm$0.0010) at 80K. Martini's data [2] show very close agreement for 10-19 MeV proton, deuterium and α particles in a Ge detector at a temperature of 90K, *i.e.* their results yield $\varepsilon_\alpha/\varepsilon_p = 0.9989 \pm 0.0015$ and $\varepsilon_\alpha/\varepsilon_d = 0.9963 \pm 0.0035$.

6.3 Bias dependence of the measured ionization energy

As mentioned in chapter 3, the window energy loss of the Ge detector for

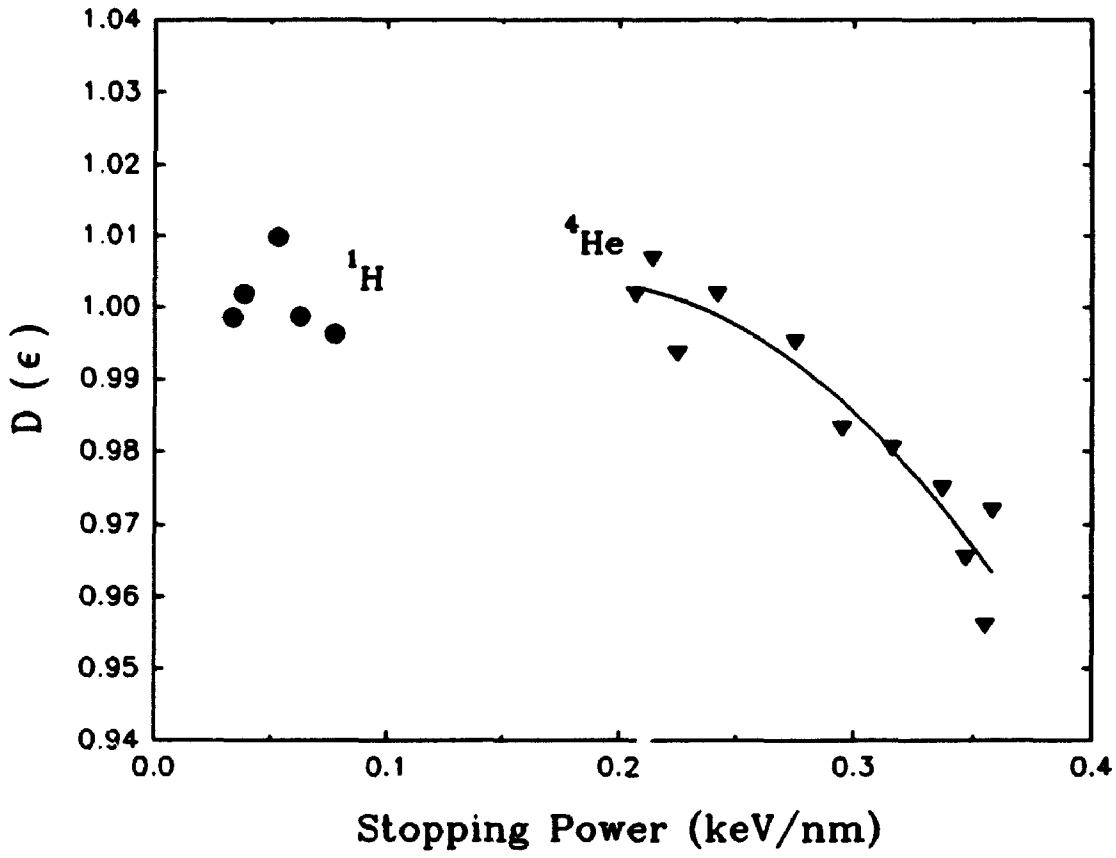

Figure 6.3 The differential ratio $D(\varepsilon)$ of $\varepsilon_{ion}/\varepsilon_0$ is based on the data in tables 6.1 and 6.2, and calculated by $[E_{ion}(i+1)-E_{ion}(i)]/[E_\gamma(i+1)-E_\gamma(i)]$. The corresponding stopping power is chosen at the mean energy, $[E_{ion}(i+1)+E_{ion}(i)]/2$.

~2.5 MeV α particles remains constant when the bias (V_b) of the Ge detector changes from 400 V (total depletion voltage) to 1200 V. Figure 6.4 shows how $\varepsilon_\alpha/\varepsilon_0$ varies with the bias of the detector for 2.5 MeV α's. Based on a linear fit of $\varepsilon_\alpha/\varepsilon_0$ vs V_b^{-1}, the minimum value of $\varepsilon_\alpha/\varepsilon_0$ for 2.5 MeV α particles is 0.988 for an infinitely large electric field value ($1/V_b \rightarrow 0$). However, the actual value of $\varepsilon_\alpha/\varepsilon_0$ for $V_b \rightarrow \infty$

may

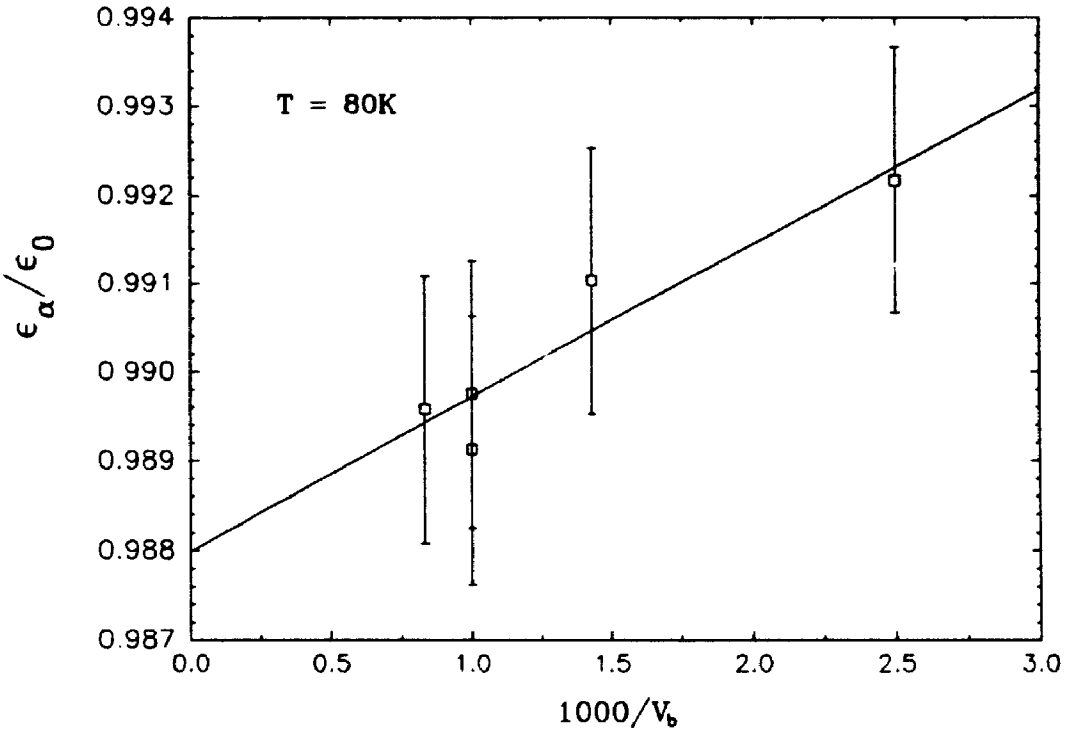

Figure 6.4 Bias dependence of $\varepsilon_\alpha/\varepsilon_0$ obtained for 2.483 MeV α particles at T = 80K. The solid line is a linear fit to the data.

be between 0.988 and 0.989. Such a small variation of ε_α with the bias may be explained by a recombination effect. (The plasma density of electron-hole pairs created along the ion track is much higher for ^{4}He ions than for γ−rays, which may increase the recombination of electron-hole pairs created by the passage of a charged particle.) In principle, a large electric field in the detector should reduce the recombination or trapping, especially for ions. For γ−rays, the density of e−h pairs associated with electron energy loss is sufficiently low that there should be no plasma effect (see ref.2 in chapter 2). That is why the α pulse height increases by a larger

fraction than that for γ's, see Figure 5.15. As a conclusion, any reduced recombination and/or trapping effect for the bias voltage exceeding 1000 V can contribute at most ~0.2% to the derived ionization energy ratio, $\varepsilon_{ion}/\varepsilon_0$. The infinitely large electric field (or bias) does not mean that the recombination can be eliminated completely because the penetration of the electric field (even when infinitely large) into the electron−hole pair plasma may be limited. So the recombination effect for ions may always exist and always acts to increase the measured value of $\varepsilon_{ion}/\varepsilon_0$. For light ions, the recombination is less than that for heavy ions due to the lower plasma density. Additionally, the changes observed for γ and α pulse heights with the detector bias are not likely caused by a charge carrier multiplication effect, because the charge multiplication requires a minimum electric field of 10^6 V/cm in semiconductor detectors [3], which is much larger than the bias (10^3 V/cm) used here. If charge multiplication were occurring in the detector, a high−energy tail in the peaks should be detected for monoenergetic radiation; such tails have not been observed. The capacitance of the Ge detector can also change with the bias (*e.g.* $C \propto V^{-0.2}$ for implanted Ge detectors at a bias less than the fully depleted voltage, see ref. 4), which may affect the output pulse amplitude of the preamplifier. However for charge−sensitive amplifiers, if the duration (τ_i) of the input pulse is shorter than the falling time constant ($\tau_f = R_{feedback}C_{feedback}$) of the preamplifier, the changes in the input capacitance (of detectors) no longer has an appreciable effect on the output voltage (of the amplifier) [5]. In this experiment, the τ_i/τ_f ratio is ~10^{-2}. Even so, the small changes (0.06%) in the γ pulse height and part of the change in the α pulse height with the detector bias from 400 V to 1200 V may be caused by a small

variation of the detector capacitance with bias.

6.4 The temperature dependence of ε_0 and ε_α

The temperature dependence of ionization energy is another important feature of the detector response, which is essentially related to the variation of the bandgap with temperature. To measure the change of ionization energy with temperature requires a precise measurement of the window energy loss. Since the window energy loss for protons is small, it is difficult to measure its change with the detector temperature. The temperature dependence of window energy loss was therefore measured only for α particles, which provides the basis for deriving ε_α at different temperatures.

First, the value of ε_0 was derived using ^{152}Eu, ^{60}Co, and ^{137}Cs γ sources in the temperature range 80 K − 170 K. By adopting the value ε_0 = 2.962 eV/e-h pair at 80 K [6], the results are shown in Figure 6.5, where the ε_0 data obtained here and Stuck's data [7] agree very well.

The ε_α and ε_0 data were also measured simultaneously at various temperatures. The results are presented in the form of the $\varepsilon_\alpha/\varepsilon_0$ ratio, which certainly will reflect the change of the ionization energy for α particles with detector temperature. As seen in Figure 6.6, the percentage difference of ε_α and ε_0 becomes smaller at higher temperatures of the Ge detector. The reason for this behaviour is complicated, as it may result from an interplay of the recombination in the bulk and the interface layer between the window and the bulk of the detector, the bandgap change and the trapping effect. The window energy losses for deriving ε_α were

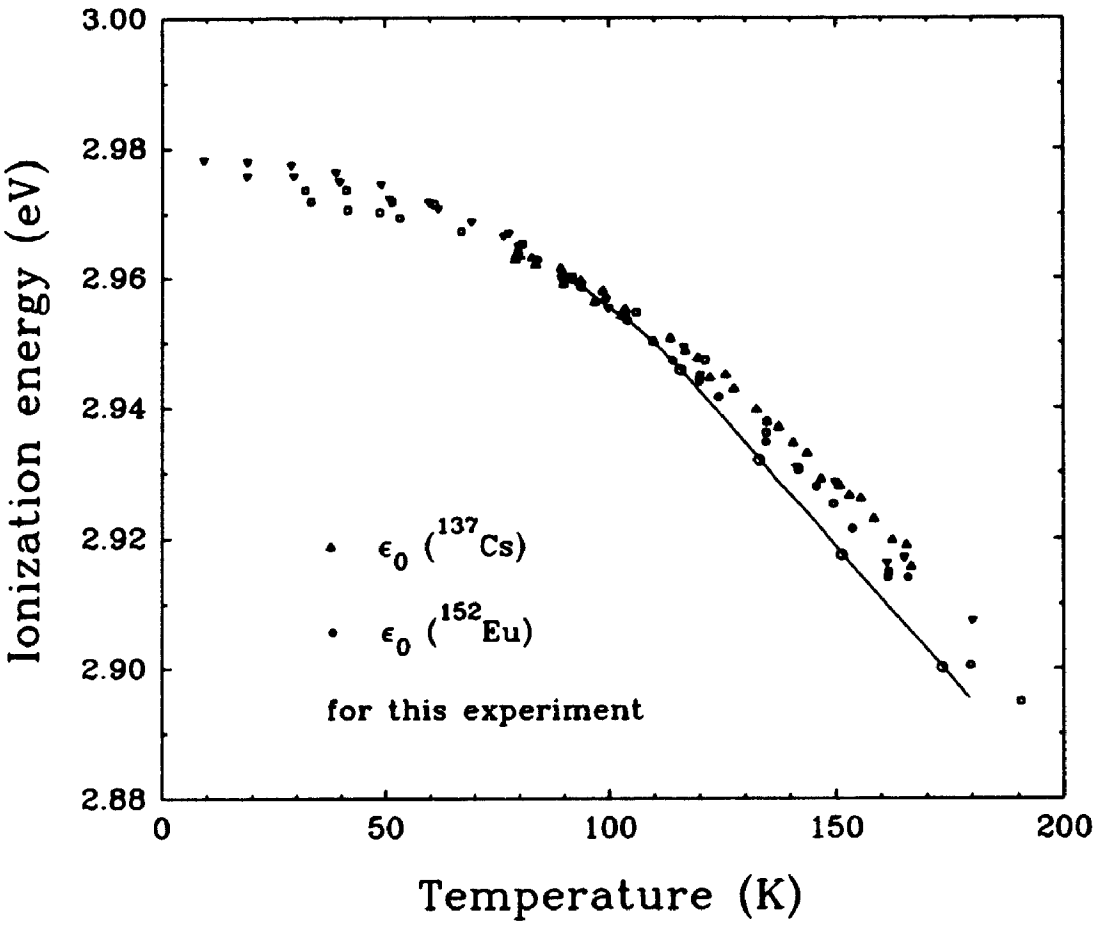

Figure 6.5 Temperature dependence of ε_0 measured in this experiment and in earlier works. Stuck's data: □ ε_0 and ▽ ε_α; Pehl's data: ○ $\varepsilon_{0 \text{ or } \alpha}$.

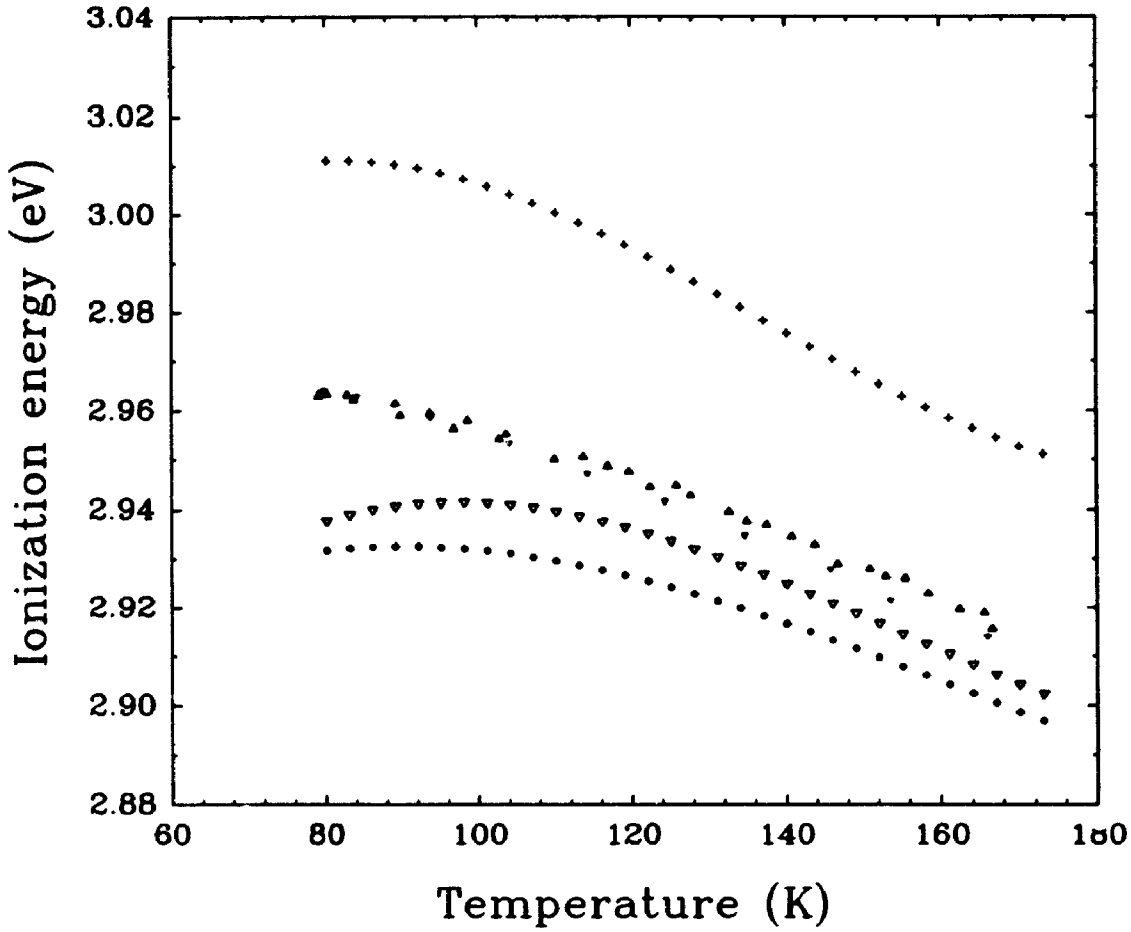

Figure 6.6 Temperature dependence of ε_α and ε_0 measured in this experiment. ε_α: ▿ (5.486 MeV), + (1.177 MeV) and • (2.483 MeV); ε_0: ▲ (^{137}Cs) , ▼ (^{152}Eu).

corrected carefully at each temperature for different α energies. The window energy loss corrections decrease with increasing temperatures. If the window energy loss were assumed to be independent of the temperature, the ε_α curves would behave differently. Figure 6.7 shows a comparison of the measured ε_α(T) with that derived assuming a constant correction for the window energy loss (the values were chosen

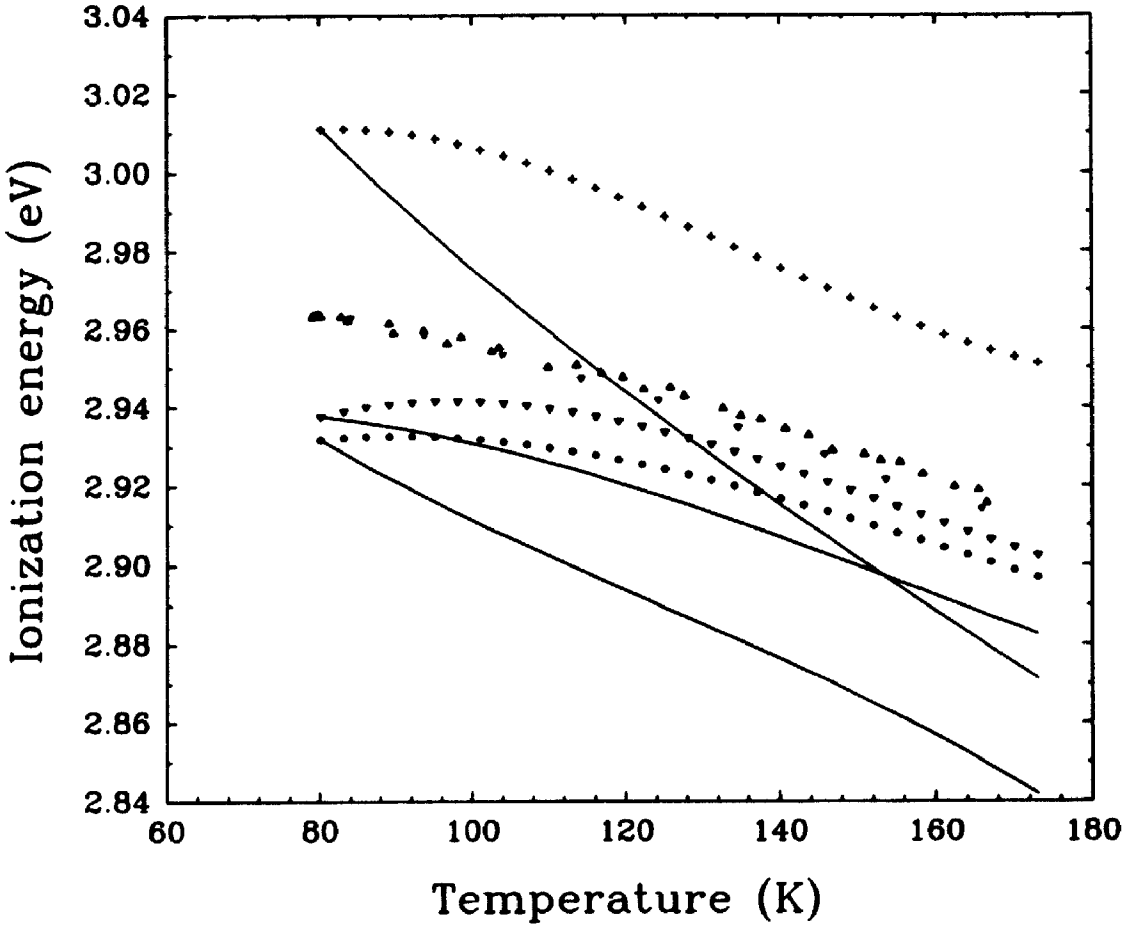

Figure 6.7 Temperature dependence of ε_α assuming a constant window energy loss. The window energy loss values for α particles at 80K are used for calculating the solid lines. For other symbols, see Figure 6.5.

at 80K). For instance, the $\varepsilon_\alpha(T)$ curve for 5.5 MeV α particles becomes parallel to the $\varepsilon_0(T)$ curve if $\Delta E_w(T)$ = const. is used for the detector window energy loss correction. In previous studies [6,7] of the ionization energy for α particles in Ge detectors, a constant window thickness was always assumed for boron–implanted Ge detectors and all α particle energies used exceeded 5 MeV, so that the temperature

dependence of ε_α always followed that of ε_0. Therefore, the previous results for ε_α(T) [7] can also be reproduced here by assuming a constant window thickness at all temperatures (for ~5 MeV α's). Again this observation demonstrates that the quality of the Ge detector used here is similar to those used in the previous studies [7].

Figure 6.8 shows the bandgap dependence of the ionization energy for α's and γ's in the Ge detector obtained in this work. The linear relation of ε_0 with the Ge

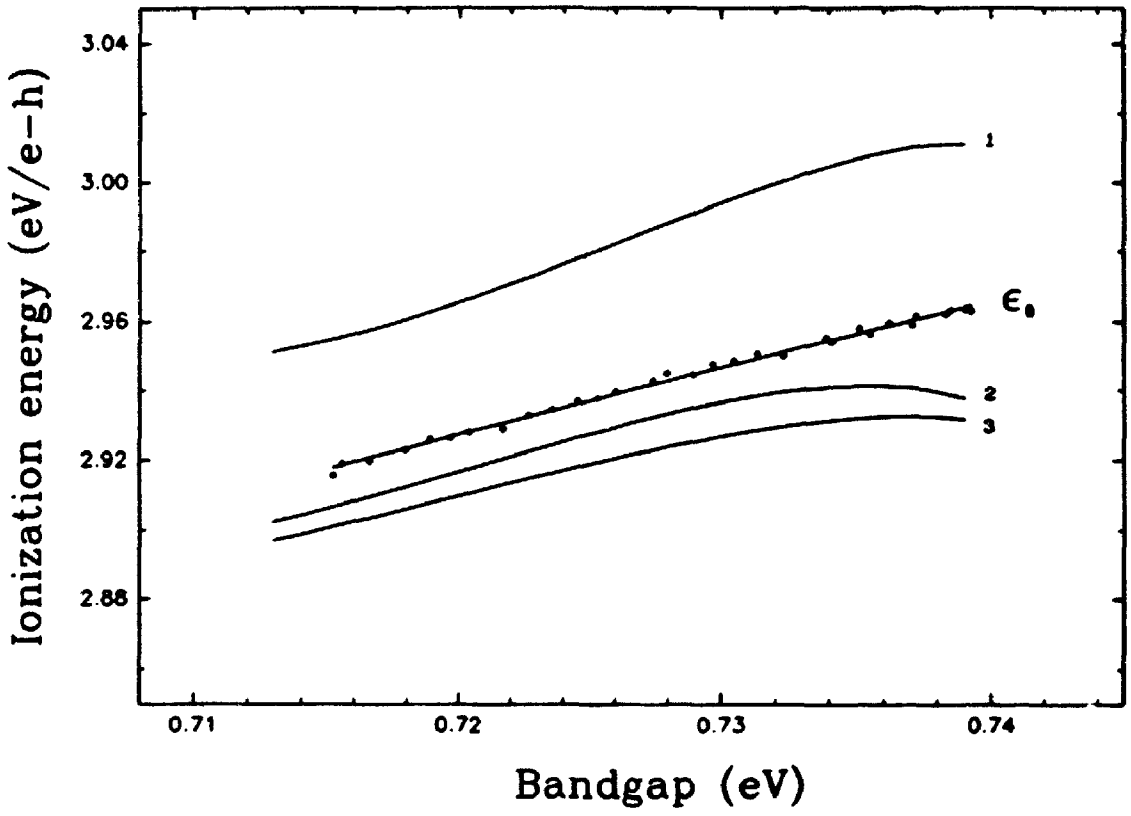

Figure 6.8 Ionization energy of γ rays and α particles as a function of the bandgap. The straight line is a fit of ε_0 data and curves marked by 1, 2, and 3 correspond to E_α = 1.177, 5.485 and 2.483 MeV.

indirect bandgap gives a slope of 1.934 and an intercept of 1.535 eV, which values agree with previous results [7] within 3%. But a non-linear change in ε_α with the indirect bandgap can be seen clearly, particularly at low temperature. This is the first time that such a non-linearity of ε_α has been observed. If a constant window energy loss were used for ε_α with ^{241}Am α particles, a linear relationship of ε_α with the bandgap would be obtained here (also see refs. 6 and 7).

6.5 Trapping and recombination effect in the Ge detector

It is necessary to specifically discuss the trapping effect together with the observations of the energy, bias and temperature dependence of ε_α and ε_0. The trapping effect refers to the phenomenon of charge (or carrier) loss in the charge collection process, in which those carriers that are trapped by defects in the detector are not subsequently detrapped during the charge collection time.

Since the rear surface (300 μm Li drifted layer) of the Ge detector is positively biased and connected to the input of the preamplifier, the output of the detector is based on the collection of electrons generated in the ionization process. For the ions used here, the ranges ($\leq$ 50μm) in the detector are only of the order of 10^{-3} of the detector depletion depth. Thus, the electrons created by energetic ions have to travel almost the entire depletion distance to be collected. Therefore, the electron trapping effect will be almost the same for all ions, which will not affect the window tilting measurements, *i.e.* the pulse height data with the detector tilting angle will still follow the curve shape defined by Equation 5.3. Possibly the pulse heights for ions at the normal incidence angle (*i.e.* P_0 - P_1) can be affected. Similar to the recombination

effect, trapping can be reduced via a strong electric field inside the detector, which may be the factor causing the increase of the bias dependence of the γ and α pulse heights. However, it is unlikely that the trapping is significant in the Ge detector used here. Since the carriers (electron) created by each γ ionization event will travel a distance corresponding to 1/2 depletion depth on average before being collected, the trapping effect will also be reduced by 50% or less (depending on the plasma density). If it is assumed that 0.06% increase of the γ pulse height with the bias changing from 400 V to 1200 V is caused by a reduction of the trapping effect, one would expect 0.12% or more increase of the pulse height for 2.5 MeV α's. But such pulse height increases may be due to a detector capacitance change with bias. In addition, the fact that the previous data [7] for ε_0 and ε_α (^{241} Am) can be reproduced here suggests again that trapping is negligible, although the n−type Ge detector with a net bulk impurity concentration of 8×10^{10} (30 keV FWHM for 5 MeV α) was used in ref. 7 and the p−type ultra−high purity Ge detector material with impurity concentration $< 10^{10}$ is used here. Note that Li, B, and P are shallow donors or acceptors and therefore do not act as traps.

6.6 Comparison of the ionization energy in Ge and Si detectors

As a conclusion of this study, it is necessary to compare the ionization energy of light ions in Ge and Si detectors in order to provide more information for understanding the basic ionization process and the response of semiconductors. The discussion will concentrate on the following three aspects and some further experiments will be suggested based on the present study.

(1) $\varepsilon_{ion}/\varepsilon_0$ ratio

Similar to Si detectors, the largest difference of the ionization energy for light ions and γ rays in a Ge detector are found to be ~1% at 80K and to approach zero as the energy of the ion increases. The energy dependence of $\varepsilon_{ion}/\varepsilon_0$ for protons and α's has a similar trend with that found for Si detectors. The $\varepsilon_{ion}-S(E)$ curve appears different from one obtained for Si detectors [9]. $\varepsilon_{ion}/\varepsilon_0$ is approximately unity in the low stopping power region (at high energy end). Above the stopping power of 0.20 keV/nm, the data show an average slope $\Delta\varepsilon_{ion}/\Delta S$ of $2.5\varepsilon_0 \times 10^{-4}$ nm/e-h pair, which is not close to the slope obtained for Si detectors [10,11]. From the data in table 6.1, it is possible that $\varepsilon_p/\varepsilon_0$ for larger stopping power values ($\geq$ 0.09 keV/nm) will behave similarly to $\varepsilon_\alpha/\varepsilon_0$, but no data are available in this region. Obviously more measurements of ε_p at higher stopping power are required, *i.e.* at lower incident energies.

(2) Apparent pulse height change with the temperature

Two possible factors that can affect the pulse height for ions in detectors as the temperature of the detector changes are contributions from the change of the window thickness and ionization energy with the temperature. In Figures 6.9 and 6.10, the change of the apparent pulse heights versus the detector temperature are presented for the Ge detector (in this study) and for the surface barrier Si detector [12]. From 173 K to 80 K the apparent pulse heights (number of electron−hole pairs) of α particles in the Ge detector decreases by 2−3% compared with $\leq$ 1% for a Si detector.

(3) Ionization energy versus E_g

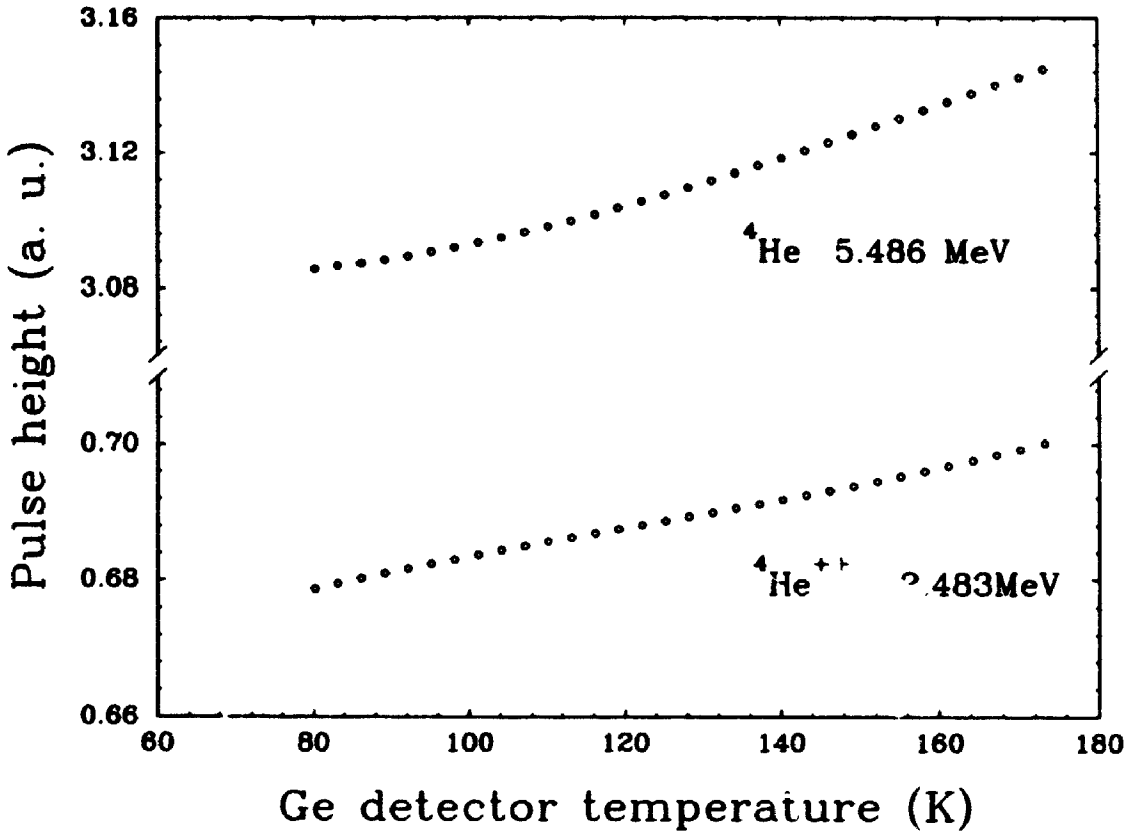

Figure 6.9 Temperature dependence of the pulse heights at normal incidence for α particles (5.846 and 2.483 MeV). Different attenuation for test pulses was used for upper and lower scales.

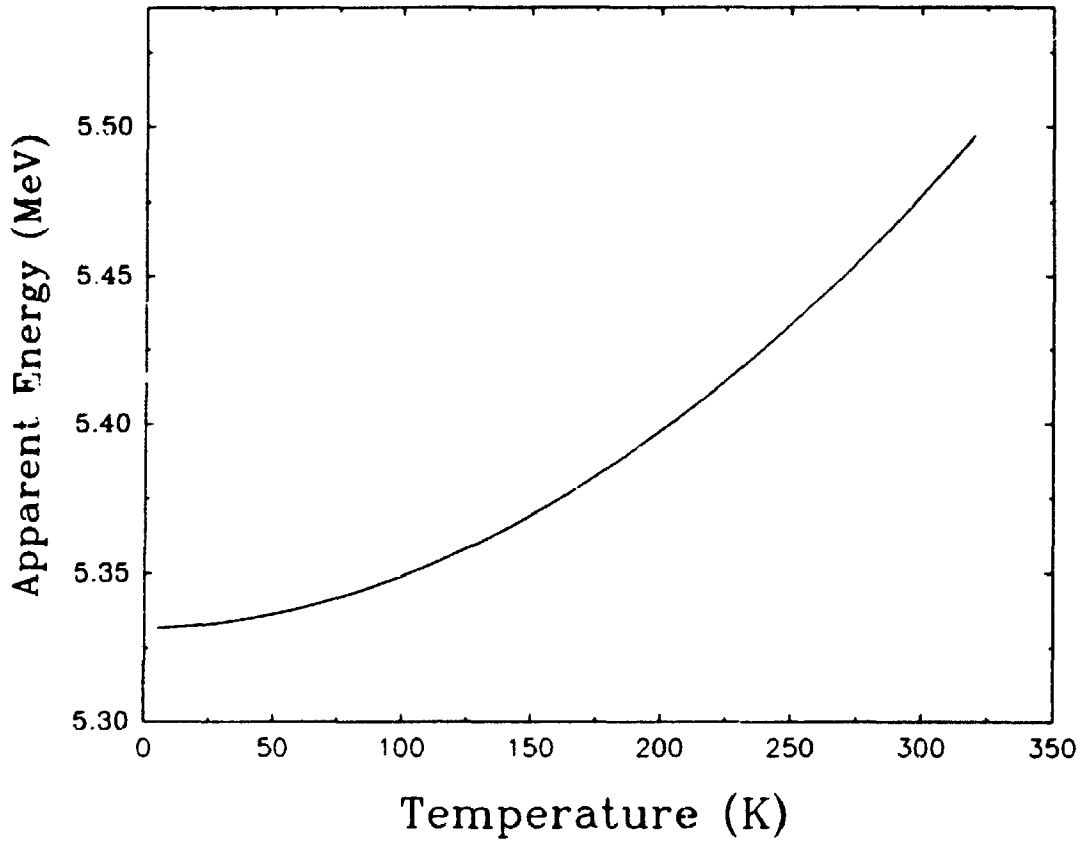

Figure 6.10 Temperature dependence of the apparent energy obtained for the 5.477 MeV ^{241}Am α particles [12].

Unlike earlier published data for Si and Ge detectors, the ε_{ion} data in the Ge detector show a nonlinear change with the bandgap (see Figure 6.8). The temperature dependence of the detector window energy loss is an important correction for such a nonlinear phenomenon to be seen. Measurements of the effective window thickness of the boron-implanted Ge detector, based on the tilting technique, have proved that the implanted window thickness cannot be accurately determined using the energy loss straggling method [7]. This observation raises a

question as to how to make the window correction for ionization energy measured in Si detectors. It is not clear how the window thickness of Si detectors was measured as a function of temperature, even though a linear change of the surface barrier window and no change of the ion–implanted window were claimed [7,13]. It is still possible that the temperature dependence of the window thickness can be so large that the linear relation between ε_{ion} and the bandgap for Si detectors will be affected by such a window correction, even though the window energy loss (at room temperature) for Si detectors in previous studies [2,7] were claimed to be very small (0.5% effect on ε_{α}).

6.7 Conclusions

Summarizing the results obtained from the experimental studies performed here, several points should be emphasized:

(1) Contrary to earlier conclusions, we can assert that there is a ~1% difference between ε_{ion} (light ions at lower energy) and ε_0, often exhibiting $\varepsilon_{ion} < \varepsilon_0$. This conclusion cannot be explained away by trapping or recombination effects during the stopping of the ion in the sensitive volume – both of which would act in the opposite direction to yield data whereby $\varepsilon_{ion} > \varepsilon_0$.

(2) For very energetic ions, $\varepsilon_{ion} = \varepsilon_0$, which is to be expected on an intuitive basis.

(3) The apparent window thickness measured for the detector under study varies with ion energy and temperature in a manner that suggests that this surface layer does not consist of a simple passive dead layer. The reasons for this behaviour are not understood.

(4) Where comparisons can be made with earlier works, the present results for the ratio $\varepsilon_{ion}/\varepsilon_0$ are in quantitative agreement when similar assumptions are included, *e.g.* when we assume that the apparent window thickness does not depend on ion energy.

(5) The behaviour observed for Ge is in qualitative, but not quantitative, agreement with data measured for Si detectors.

(6) Channeling effects on the incident ions are readily observed for the ion−implanted entrance window region; however, such effects are not responsible for the intrinsic deviations of the $\varepsilon_{ion}/\varepsilon_0$−ratio from unity.

Further measurements along the lines of those described herein would benefit from an intensive study of the ion−implanted window region, *i.e.* $\varepsilon_a/\varepsilon_0$ should be determined using different conditions (implant dose, energy and high−T annealing) for fabricating the front contact. As well, the detector crystal should be cut off−axis to minimize or eliminate channeling effects for both implantation and ion detection. This remark is motivated by the unexplained behaviour observed for the energy loss of ions, in particular α's, transmitted through the front contact as a function of ion energy and temperature. Such measurements for Si detectors at different temperatures may also shed light on the physical processes that are occurring in this complicated interface region. It would be interesting to extract defect profiles for such semiconductor detectors, as their role may dominate the observed window energy loss behaviour under charged particle detection.

References

1. R. D. Ryan, IEEE Trans. Nucl. Sci. NS−20 (1973) 473.
2. M. Martini, T. W. Raudorf, W. R. Stott and J. C. Waddington, IEEE Trans. Nucl. Sci. NS−22 (1975) 145.
3. F. J. Walter, IEEE Trans. Nucl. Sci. NS−11 (1964) 232.
4. J. P. Ponpon, J. J. Grob, R. Stuck, P. Burger and P. Siffert, 2nd Int. Conf. on Ion Implantation in Semiconductors, Garmisch−Partenkirchen, eds. I. Ruge and J. Graul (Springer, 1971) p.420.
5. G. F. Knoll, "Radiation Detection and Measurement", Wiley, 1989 (2nd edition) p.590.
6. R. H. Pehl, F. S. Goulding, D. A. Landis and M. Lenzlinger, Nucl. Instr. and Meth. 59 (1968) 44.
7. R. Stuck, J. P. Ponpon, R. Berger and P. Siffert, Rad. Eff. 20 (1973) 75.
8. G. G. Macfarlane, T. P. McLean, J. E. Quarrington and V. Roberts, Phys. Rev. 108 (1957) 1377.
9. D. Comedi and J. A. Davies, Nucl. Instr. and Meth. B67 (1992) 93.
10. W. N. Lennard, H. Geissel, K. B. Winterbon, D. Phillips, T. K. Alexander and J. S. Forster, Nucl. Instr. and Meth. A248 (1986) 454.
11. P. Bauer and G. Bortels, Nucl. Instr. and Meth. A299 (1990) 205.
12. C. Canali, M. Martini, G. Ottaviani and A. A. Quaranta, IEEE Trans. Nucl. Sci., NS−19 (1972) 9.
13. J. M. Caywood, C. A. Mead and J. W. Mayer, Nucl. Instr. and Meth. 79 (1970) 329.